2013-07-26

Lateral Current Density Distribution in a PEM Fuel Cell

Shan Jia
University of Miami, jason.jaa@hotmail.com

UNIVERSITY OF MIAMI

LATERAL CURRENT DENSITY DISTRIBUTION IN A PEM FUEL CELL

By

Shan Jia

A DISSERTATION

Submitted to the Faculty
of the University of Miami
in partial fulfillment of the requirements for
the degree of Doctor of Philosophy

Coral Gables, Florida

August 2013

UNIVERSITY OF MIAMI

A dissertation submitted in partial fulfillment of
the requirements for the degree of
Doctor of Philosophy

LATERAL CURRENT DENSITY DISTRIBUTION IN A PEM FUEL CELL

Shan Jia

Approved:

_____ Hongtan Liu, Ph.D. Professor of Mechanical and Aerospace Engineering	_____ M. Brian Blake, Ph.D. Dean of the Graduate School
_____ Xiangyang Zhou, Ph.D. Associate Professor of Mechanical and Aerospace Engineering	_____ Na Li, Ph.D. Assistant Professor of Mechanical and Aerospace Engineering
_____ Gang Wang, Ph.D. Assistant Professor of Civil, Architectural and Environmental Engineering	

JIA, SHAN (Ph.D., Mechanical and Aerospace Engineering)
Lateral Current Density Distribution in a PEM Fuel Cell (August 2013)

Abstract of a doctoral dissertation at the University of Miami.

Dissertation supervised by Professor Hongtan Liu.
No. of pages in text. (121)

In a polymer electrolyte membrane (PEM) fuel cell, local current density distributions are critical to the overall fuel cell performance. Local current density can vary drastically in the lateral direction across land and channel areas. Non-uniform distribution of current density can lead to serious problems at certain locations, which may accelerate membrane and catalyst degradations. It is essential to know the lateral current density distribution in order to optimize the flow field design and operation conditions. Thus the objectives of this study are (a) to directly measure the current density distribution in the lateral direction across land and channel areas in millimeter resolution, (b) to analyze the fundamental mechanisms of the current density variations in the lateral direction by electrochemical methods, (c) to develop a method to enhance fuel cell performance based on experimental results, and (d) to use a 3-dimensional numerical model to simulate the current density distribution.

Partially-catalyzed membrane electrode assemblies (MEAs) are used to measure the lateral current density distribution. Results show that in the high cell voltage region, the current density decreases drastically from the center of the land to the center of the channel; while in the low cell voltage region, the current density under the channel becomes higher than that under the land. Flow rates and oxygen concentrations at the

cathode side also affect the current density distribution between land and channel. Further studies are conducted to investigate the fundamental mechanisms of such significant lateral current density variations. Results from cyclic voltammetry (CV) show that electro-chemical area (ECA) is a major factor that leads to different local current densities in the lateral direction. Further study by electrochemical impedance spectroscopy (EIS) shows that charge transfer resistance under the land is lower than that under the channel, but mass transport resistance under the land is higher in the low cell voltage region. Inspired by the results that the current density under the land is higher than the channel, a novel method, namely the cold pre-compression treatment is developed to enhance the performance under channel areas. The results show that the overall performance of a PEM fuel cell indeed increases with the cold pre-compression treatment. However, over-compression may have a significantly detrimental effect on the fuel cell performance. In order to simulate the current density distribution in a PEM fuel cell, a 3-dimensional numerical model with a serpentine flow field is developed using FORTRAN. ECA variations in the lateral direction under land and channel are incorporated in the model. The model results agree well with experimental data.

ACKNOWLEDGEMENTS

I would like to express my great appreciation and respect to my advisor and Ph.D. committee chairperson Dr. Hongtan Liu. In the last four years, he not only advised my Ph.D. study, but also passed his wisdom and life experience to me. He encouraged me to pursue comprehensive understandings of fundamental mechanisms behind physical phenomena. The discussions on the research with him always inspired me and helped me generate new ideas.

I would like to give my acknowledgements to all my committee members, Dr. Xiangyang Zhou, Dr. Na Li and Dr. Gang Wang. My Ph.D. dissertation is greatly improved with their suggestions.

The fuel cell lab is a nice place where I devote and obtain a lot. Here I met a good group of intelligent people, to whom I also want to give my thanks. Mr. Song Luo and Mr. Xuyang Zhang are the best colleagues and friends; Dr. Andrew Higier, Dr. Saif Matar and Dr. Hidetaka Taira also gave me a lot of help during my study.

I would like to thank all the friends I met in the University of Miami during the past four years, for your help and company.

Last but not least, I feel grateful to my dear parents. They gave me the chance to explore this great world, to live this wonderful life. Without their support, my study could not be completed.

TABLE OF CONTENTS

Page

LIST OF FIGURES

LIST OF TABLES

LIST OF NOMENCLATURE

a	ECA at cathode ($m^2 \cdot m^{-3}$)
c	Mole concentration ($mol \cdot m^{-3}$)
D	Gas channel depth (m)
D_{eff}	Effective diffusivity ($m^2 \cdot s^{-1}$)
D_k	Air diffusivity ($m^2 \cdot s^{-1}$)
E_0	Open circuit potential (V)
F	Faraday constant (96,487 $C \cdot mol^{-1}$)
i_0^{ref}	Reference exchange current density ($A \cdot m^{-2}$)
j	Transfer current density ($A \cdot m^{-3}$)
k_p	Permeability (m^2)
L	Gas channel length (m)
p	Pressure (Pa)
$r^{(2)}$	Coefficient in the momentum equation for porous materials
R	Universal gas constant (8,314 J)
S_k	Source term in species equation (s^{-1})
t	Thickness for different layers (m)
T	Temperature (K)
$\boldsymbol{V}$	Velocity vector ($m \cdot s^{-1}$)
W	Gas channel width (m)
X_{O_2}	Oxygen mole fraction
x	x direction coordinate (m)

y	y direction coordinate (m)
z	z direction coordinate (m)

Greek symbols

α	Transfer coefficient
ε	Porosity
η	Overpotential (V)
μ	Viscosity (Pa·s)
ρ	Density (kg·m^{-3})
σ	Conductivity (S·m^{-1})
ϕ	Potential (V)

Subscripts and Superscripts

a	Anode
c	Cathode
cl	Catalyst layer
eff	Effective
g	Gas diffusion layer
in	Inlet
m	Membrane phase
ref	Reference
s	Solid phase

CHAPTER 1

INTRODUCTION

1.1 An outlook of energy development

In recent years, the demand for natural energy resources by human beings has been growing very fast. Fig. 1.1 shows the estimates of total primary energy consumption in United States in the past 60 years [1]. The amount in the year of 2010 is almost three times of that in 1950. Clearly traditional fossil fuel resources such as coal and petroleum may not meet the requirement of the energy consumption in the future.

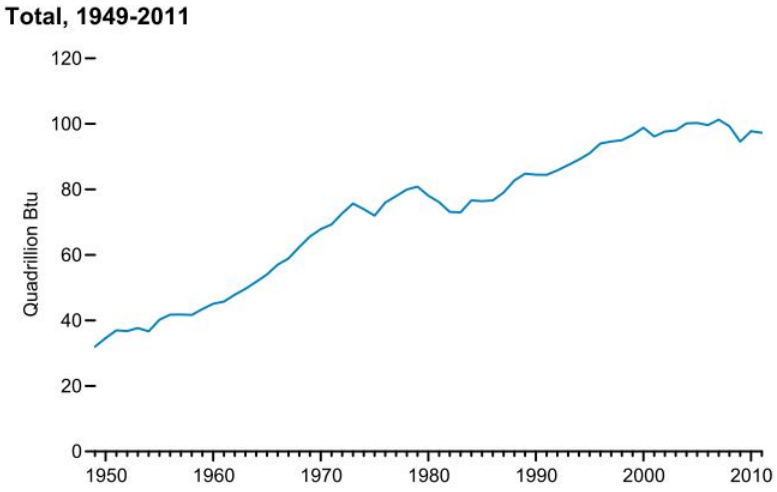

Fig. 1.1 Total primary energy consumption estimates in U.S. from 1949 to 2011 [1]

Due to the population explosion and uncontrolled resource exploitation, the world is facing a severe energy environment more than ever. The report from U.S. Energy Information Administration shows that the world energy consumption will increase by 47 percent from 2010 to 2035 as shown in Fig. 1.2 [1]. The most robust growth is from non-OECD Asia as the quick development of Asian economy has consumed a large amount of

energy recently. In addition, some of those countries and areas only focus on the GDP growth but do not pay enough attentions to waste of energy and consequent pollution to environment. Essentially all of the countries in the world should take the responsibility to the continuous development of energy economics.

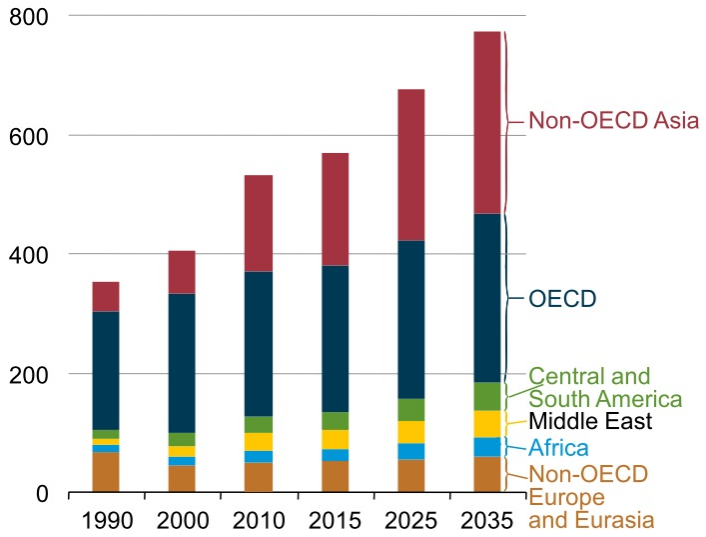

Fig. 1.2 World energy consumption by region, 1990-2035 [1]

Based on the fact that fossil energy resources stored on the earth are limited, how could human survive after the depletion of coals, petroleum and natural gas in centuries? Fortunately, a lot of alternative resources are discovered and developed to maintain the fast growth of energy consumption from human's activity. Fig. 1.3 shows that the renewable energy grows very fast in the recent decade, while the consumption of traditional fossil energy resources such as coal and petroleum decreases [1]. Clearly, renewable energy will become a great supplementary to the traditional fossil energy world in the near future. As the renewable energy does not just provide an alternative

way to solve the future energy problem, it is also a very efficient and environmental friendly resource for sustainable development of our human society.

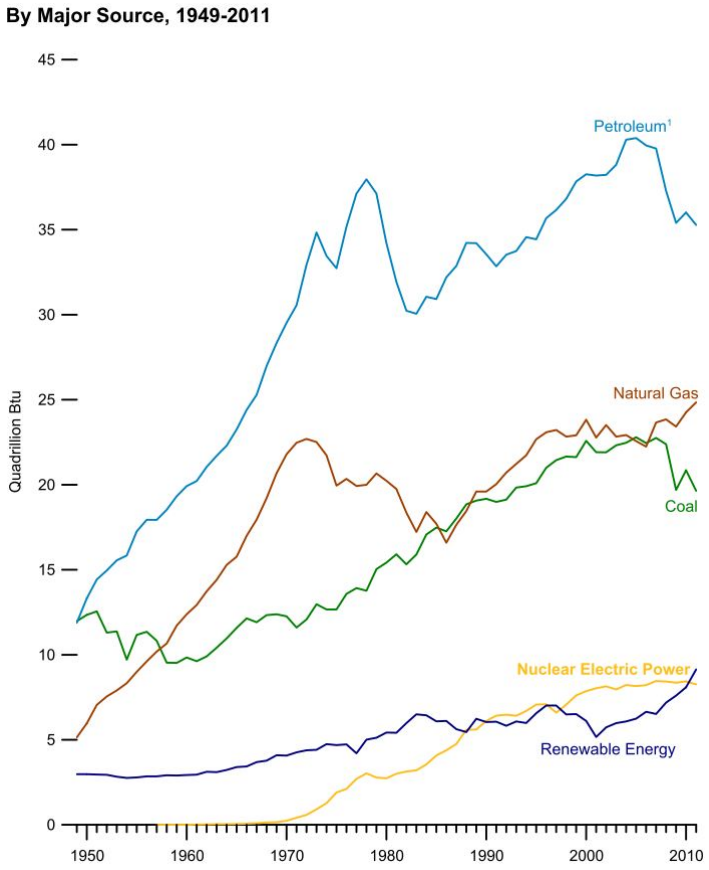

Fig. 1.3 Primary energy consumption estimates in U.S. by major source from 1949 to 2011 [1]

1.2 Fuel cell introduction

1.2.1 Why fuel cells?

Hydrogen energy is developed as one of the most important renewable energy resources. A fuel cell is a device that can convert hydrogen energy into electrical energy directly and stably. Compared with other renewable energy sources, fuel cells are quiet and reliable due to its structure without any moving parts. If fuel is available, a fuel cell

can continuously provide power supply. The advantages make the fuel cell become a very suitable application for power stations and automobiles in industry and real life society.

As power supply devices, fuel cells gain merits over its competitors, i.e. internal combustion engines and batteries. Combustion engines have higher energy density compared to fuel cells. However, due to the mechanism in a combustion engine that chemical energy of fuel must first be transformed into thermal energy, which pushes pistons inside the engine that produces mechanical energy. During this energy transformation procedure, huge amount of energy is wasted in a combustion engine. During these steps, less than 30% energy is utilized and most of the energy is lost to the environment as heat. If a further step from mechanical energy to electrical energy is desired for producing electrical power, the thermal efficiency would be even lower. In contrast, fuel cells obtain a more straightforward procedure as the chemical energy of reactants is directly converted into electrical energy by electrochemical reactions. Thus the efficiency of a fuel cell could be much higher than an internal combustion engine.

Unlike batteries, power and capacity of a fuel cell are independent on fuel cell size and its reservoir size respectively. Thus it is much more flexible to design the fuel cell application than batteries. Besides, fuel cells can approach potentially higher energy densities than batteries. Refueling hydrogen is also much faster than recharging batteries. Another advantage of a fuel cell is environmentally friendly. From the electrochemical reaction it is known that water is the only product. As global warming is a critical problem for today's world, a lot of countries are working on reducing emission of greenhouse gases such as carbon dioxide.

1.2.2 Development of fuel cells

A fuel cell is such a device that can continually transform the chemical energy in the fuel into the electrical power by electrochemical reaction [2]. It is one of the most promising technologies for the future economy of renewable energy. It is widely acknowledged that in 1839, Sir William Robert Grove first introduced the concept of a fuel cell, which he called a ‘gas battery’ as shown in Fig. 1.4. He accidently found that constant current was generated from the electrodes in hydrogen and oxygen containers respectively by reversing the water electrolysis, which showed the possibility to use hydrogen and oxygen to produce electricity.

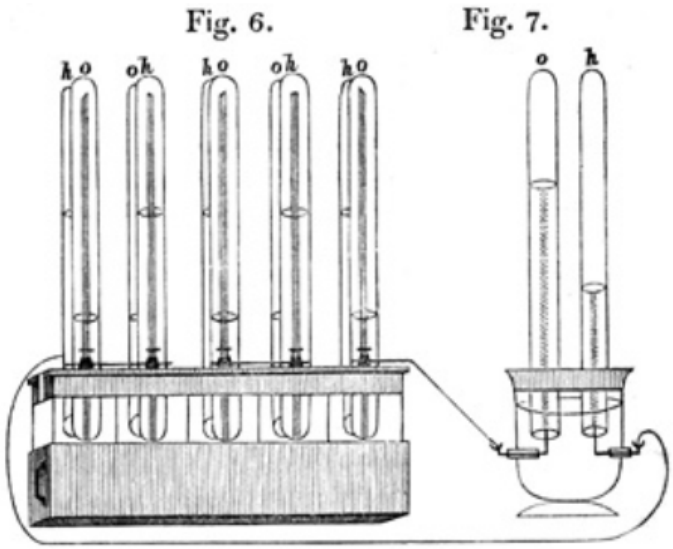

Fig. 1.4 William Grove's drawing of an experimental "gas battery" from a 1843 letter (Proceedings of the Royal Society)

Although the phenomenon was discovered at that early age, there was very little progress of fuel cell development during the 19th century. It was not until 1889 that Charles Langer and Ludwig Mond developed a real fuel cell using coal gas and air. Unfortunately the great advances of internal combustion engines delayed the application

of fuel cells at the beginning of the 20th century. In 1950s, GE firstly invented polymer electrolyte membrane (PEM) fuel cells. Solid polymer electrolyte was used inside a fuel cell instead of aqueous acid electrolyte, which greatly simplified the design of structure [3]. In 1959, Francis Bacon demonstrated a 5kW alkaline fuel cell. In 1962, GE was awarded of the NASA contract for the Gemini space mission, in which the fuel cell system was conducted and tested [4]. A door was slowly opened to the great application of fuel cells in engineering fields. However, due to the short durability and unstable performance of the fuel cell at that time, it was still not widely used. In 1980s, a great improvement in reducing the catalyst usage brought back people's interests on fuel cells. The amount of precious metal used as fuel cells catalyst was reduced by over 100 times, thus the cost decreased to a much lower level [5]. The advance consequently led to the great development of applications in different nature [6], such as auto industry, military and human's life as shown in Fig. 1.5. Since the fuel cell was firstly used in an Allis-Chalmers tractor in 1959, it had been involving in the research and manufacture among most large automobile companies in the current decade. Due to the relatively high cost, the pre-commercial fuel cell vehicle model was still locally tested, such as Honda FCX Clarity in California. But Honda announced that fuel cell vehicles would contribute in auto market in the near future. Another wide application for fuel cells is stationary electric power source and backup. The supply power between these applications varies greatly, from the very high power supply like DFC3000 system by FuelCell Energy over 2.8MW to the power backup for telecommunication facilities as low as 50kW. Moreover, portable fuel cell applications are also developed to provide electrical power to the portable electronic devices, such as the PEM fuel cell charger from PowerTrekk™.

Fig. 1.5 Application of fuel cells in auto industry (Honda FCX Clarity, Honda Motor Co.), power supply (Fuel Cell Energy) and human's life (potable charger, PowerTrekk™)

The great development of fuel cells also provided an opportunity to construct a better energy supply system by renewable energy resources. The Hydrogen Assisted Renewable Power (HARP) project installed in Bella Coola, Canada and operated by GE and its partners was such a system. It included solar, wind, hydro energy and fuel cells as well as electrolyzers to build up a sustainable energy circulation system. The schematic of this cycle is shown in Fig. 1.6. In such a system, the power generated by solar, wind and micro hydro systems can either directly produce electricity for use, or provide power to electrolyze water to approach hydrogen, and fuel cells can be the station to supply power by stored hydrogen when the energy demand exceeds the supply during the high peak of energy consumption. The advantage of such a system is that the energy resources from solar and wind are almost unlimited, which leads to the endless energy supply. Fuel cells are one of the important parts inside this energy circulation.

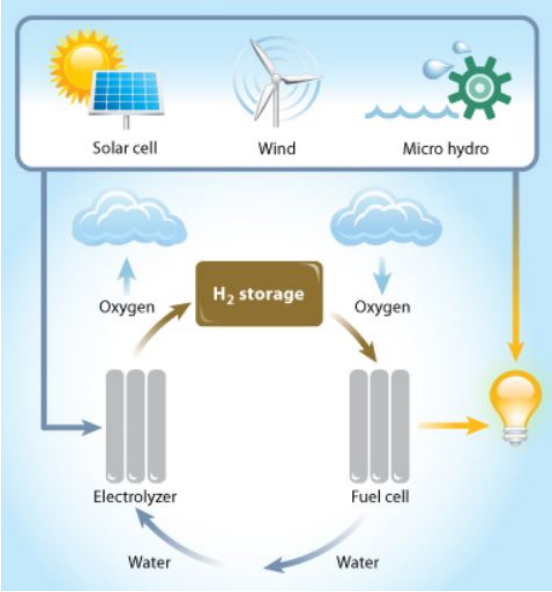

Fig. 1.6 Schematic of Hydrogen Assisted Renewable Power (HARP) project by BC Hydro, GE and Powertech (Figure from National Research Council Canada)

1.2.3 Major types of fuel cell

In the long run of fuel cell development there exist five major types, which are categorized by their electrolyte materials. They are polymer electrolyte membrane fuel cell (PEMFC), phosphoric acid fuel cell (PAFC), alkaline fuel cell (AFC), molten carbonate fuel cell (MCFC) and solid oxide fuel cell (SOFC). Due to their mechanisms, most of them are operated at different temperature ranges, constructed by different materials for electrodes and electrolyte, and also differentiated with their fuel tolerance and characteristics of performance [2].

The PEMFC and PAFC both have the proton-conductible electrolyte. But PEMFC has the solid polymer membrane as the electrolyte, while PAFC's electrolyte is the phosphoric acid. Compared with PAFC, the PEMFC is more flexible and accessible for structure design due to its solid electrolyte. Besides, the PAFC contains pure phosphoric

acid, which keeps evaporating into the environment. Thus the PAFC has to be replenished during the cell operation. Moreover, because of the phase transition above 210 ^{o}C for pure phosphoric acid, the operating temperature for PAFC is generally locates between 180 ^{o}C and 210 ^{o}C. The anode and cathode electrochemical reactions for both types are:

Anode:

$$H_2 \rightarrow 2H^+ + 2e^- \tag{1.1}$$

Cathode:

$$\frac{1}{2}O_2 + 2H^+ + 2e^- \rightarrow H_2O \tag{1.2}$$

Alkaline fuel cell is a type of fuel cell which uses alkaline solution as the electrolyte to let OH^- transport as the charge. Due to the higher rate of oxygen reduction reaction (ORR) at the cathode, an AFC can approach higher operating cell voltage compared with PEMFC. However, the AFC requires pure hydrogen and oxygen as the reactants, while air can be used as the cathode reactant in a PEMFC. In addition, alkaline solution is used as the electrolyte in an AFC, which needs to be replenished occasionally. The AFC anode and cathode electrochemical reactions are:

Anode:

$$H_2 + 2OH^- \rightarrow 2H_2O + 2e^- \tag{1.3}$$

Cathode:

$$\frac{1}{2}O_2 + 2e^- + 2H_2O \rightarrow 2OH^- \quad (1.4)$$

Both molten carbonate fuel cell and solid oxide fuel cell do not require precious metal catalyst. It greatly reduces the cost of catalyst in a fuel cell compared with other types. These two types of fuel cell are both running at the temperature over 600 ^{o}C, which can significantly increase the fuel cell efficiency, especially for those systems conjugated with heat power utilization. However, high temperature also brings challenges to the MCFC and SOFC. For example, materials in the system have to undertake much faster aging than the low temperature fuel cell. The fabrication and construction of cell systems are more expensive and non-flexible. The electrochemical reactions are shown respectively:

MCFC Anode:

$$H_2 + CO_3^{2-} \rightarrow CO_2 + 2H_2O + 2e^- \quad (1.5)$$

MCFC Cathode:

$$\frac{1}{2}O_2 + CO_2 + 2e^- \rightarrow CO_3^{2-} \quad (1.6)$$

SOFC Anode:

$$H_2 + O^{2-} \rightarrow H_2O + 2e^- \quad (1.7)$$

SOFC Cathode:

$$\frac{1}{2}O_2 + 2e^- \rightarrow O^{2-} \quad (1.8)$$

Clearly different types of fuel cell may be suitable to different applications and locations due to their mechanisms. Table 1.1 compares the properties of these five major types of fuel cell introduced above. The PEMFC has relatively wider power density range and power range, so it is promising to focus on this type of fuel cell.

Table 1.1 Comparison summary of the five major fuel cell types [2]

Fuel Cell Type	Electrical Efficiency (%)	Power Density ($mW \cdot cm^{-2}$)	Power Range (kW)	Internal Reforming	CO Tolerance	Balance of Plant
PAFC	40	150-300	50-1000	No	Poison (1%)	Moderate
PEMFC	40-50	300-1000	0.001-1000	No	Poison (<50ppm)	Low-moderate
AFC	50	150-400	1-100	No	Poison (<50ppm)	Moderate
MCFC	45-55	100-300	100-100,000	Yes	Fuel	Complex
SOFC	50-60	250-350	10-100,000	Yes	Fuel	Moderate

1.2.4 Components of a PEM fuel cell

The schematic of components for a general PEM fuel cell is shown in Fig. 1.7. It is constructed by membrane electrode assembly (MEA) for electrochemical reaction and flow plates for conducting reactants at anode and cathode side. Out of the flow plates are

current collector plates coated with gold to collect current produced by the MEA. End plates are used to assemble the fixture to avoid leakage of reactants.

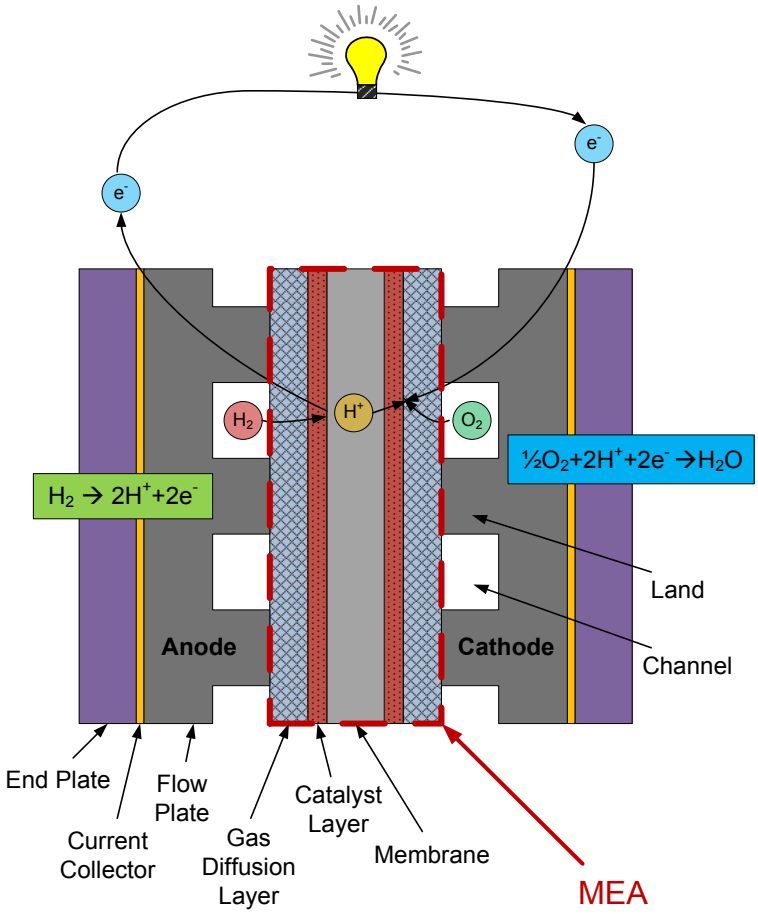

Fig. 1.7 Schematic of a PEM fuel cell and its components

Among these components, MEA is the most critical part for a PEM fuel cell. It is not only the place for electrochemical reactions, but also provides the accessibility of proton transportation. The MEA is constructed by three major parts, i.e. polymer electrolyte membrane (PEM), catalyst layers (CLs) and gas diffusion layers (GDLs) as shown in Fig. 1.7. Hydrogen gas comes into channels at the anode side, and diffuses onto the catalyst surface where hydrogen molecules are split into protons and electrons. While electrons are conducted along the external electrical circuit to the cathode side, protons transfer

through the PEM. After protons reach the reaction sites in the cathode catalyst layer, the electrochemical reaction takes place with the electrons as well as oxygen molecules conducted from cathode channels. Thus the electricity is generated by a PEM fuel cell.

1.2.4.1 Polymer electrolyte membrane

The polymer electrolyte membrane is designed to conduct protons but to avoid electrons transport through it, as the electron conduction beyond the external circuit will mitigate the potential difference between two electrodes thus decreases the open circuit voltage (OCV). Nafion® is one of the most common commercial PEM materials from DuPont. In 1950, a material called Polytetrafluoroethylene (PTFE) was invented by DuPont. Based on PTFE, they developed another material called Nafion. It has PTFE as the backbone and sulfonic groups attached, which provide the mechanical stability as well as the proton conduction accessibility. The proton conductivity of Nafion® is highly dependent on its water content, which is one of the most significant factors to affect the ohmic resistance of a PEM fuel cell. Thus it is very important to provide highly humidified reactant gases to saturate the polymer electrolyte membrane in a PEM fuel cell.

1.2.4.2 Catalyst layer

Due to the relatively slow oxygen reduction reaction (ORR) kinetics at the cathode side of a PEM fuel cell, a catalyst is typically needed to accelerate the electrochemical reaction. Platinum is the general precious metal used as the catalyst in a PEM fuel cell. As Fig. 1.8 shows, there exists electro-chemical area (ECA) at the interface between

electrode and electrolyte materials. It refers to the location where there are catalytic particles, Nafion® materials and gas pores. Clearly the catalytic particles are the substrate for the electrochemical reaction; while reactant gas diffuses from the gas pores and protons transport inside the Nafion® materials. In other words, without these three components, the ECA would not exist and there is nowhere for the reaction happens.

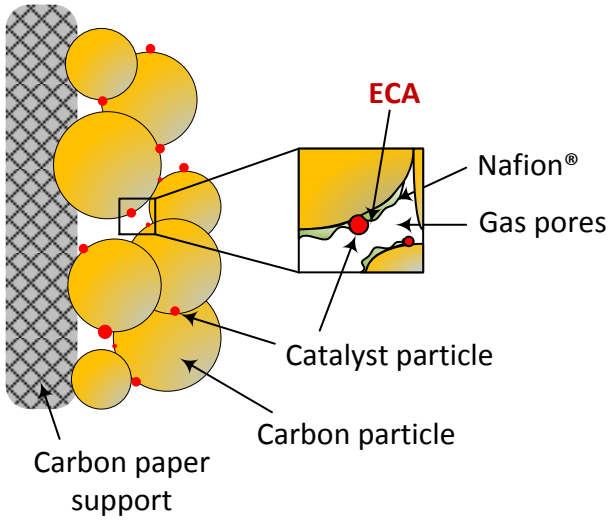

Fig. 1.8 Schematic of electrode-electrolyte interface in a fuel cell (reproduced from [7])

Due to the value of the catalyst layer, Middelman [8] observed the micro-structure using scanning electron microscopy (SEM) in nanometer resolution. The figure at left hand side in Fig. 1.9 shows that on the scale of 200 nm, particles are agglomerates with many smaller particles. The composition of their coatings is analyzed by energy dispersive X-ray analysis (EDX) which proves the presence of the Nafion skin. With further increasing the electron energy in the HR-SEM, the figure at right hand side presents that agglomerates are built up with the substrate of carbon particles (in diameter 30-100 nm), coated with finely dispersed platinum particles (in diameter 2-5 nm).

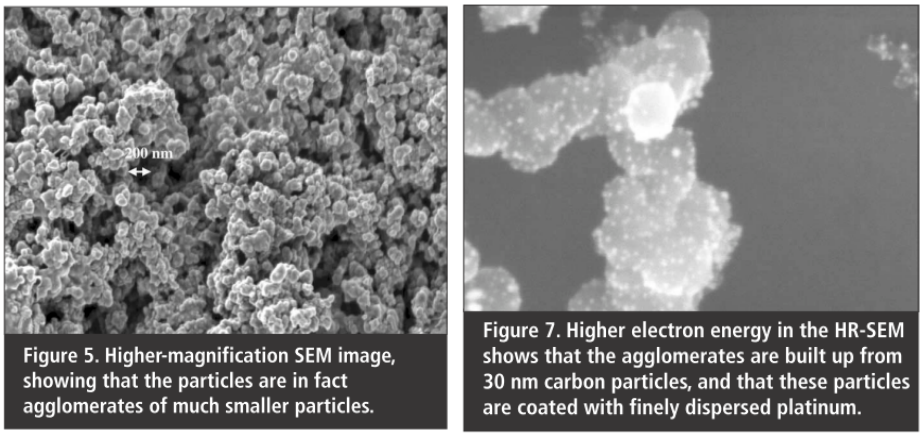

Fig. 1.9 Micro structure of catalyst layer in nanometer resolution [8]

1.2.4.3 Gas diffusion layer

Gas diffusion layers are the functional layers to improve the distribution of reactant gases into the catalyst layers. Fig. 1.10 shows two major kinds of GDL materials popularly used in PEM fuel cell applications [9].

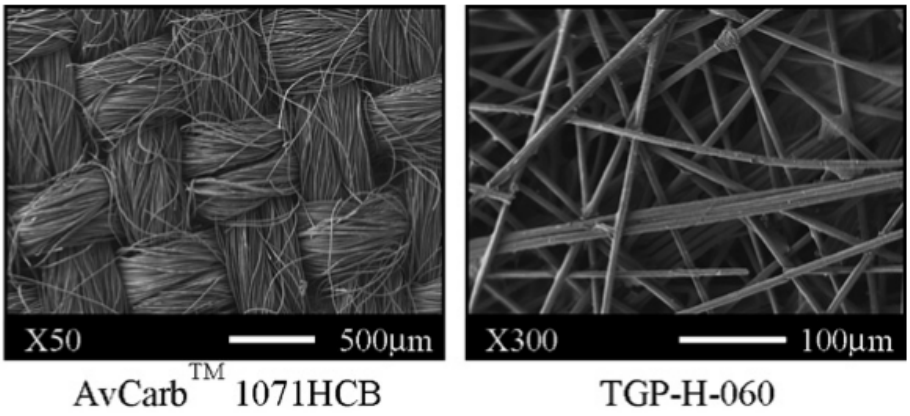

Fig. 1.10 Micro structure of GDL under high resolution [9]

The figure in left hand side is AvCarb™ model from Ballard and the right hand side is from Toray Industries, Inc. It can be seen that the left one is manufactured by carbon cloth, while the right one is more rigid and constructed by carbon fiber. Due to the

mechanism that water produced at the cathode side of a PEM fuel cell, the GDL also helps conducting liquid water out of catalyst layer. Thus for most of condition GDL is also mixed with hydrophobic materials (e.g. PTFE) during manufacture procedure. Moreover, in order to enhance the water management, a micro porous layer (MPL) is usually coated onto the gas diffusion layer to enhance the water transportation and avoid water clogging inside porous materials.

1.3 Characterization of a PEM fuel cell

The theoretical potential of a PEM fuel cell is dependent on the Gibbs free energy change in Equation (1.9). E^0 is the reversible voltage, while at standard temperature and pressure for a PEM fuel cell it equals 1.23V. $\Delta\hat{g}^0_{rxn}$ is the stand-state free energy change for the reaction. n equals the number of moles of electrons transferred per mole reactant. F is Faraday's constant.

$$E^0 = -\frac{\Delta\hat{g}^0_{rxn}}{nF} \tag{1.9}$$

Regardless of the direct mixed potential and other losses due to the reactants crossover the membrane, there are three major losses typically existing in a PEM fuel cell which greatly reduce overall fuel cell performance as shown in Fig. 1.11 [10].

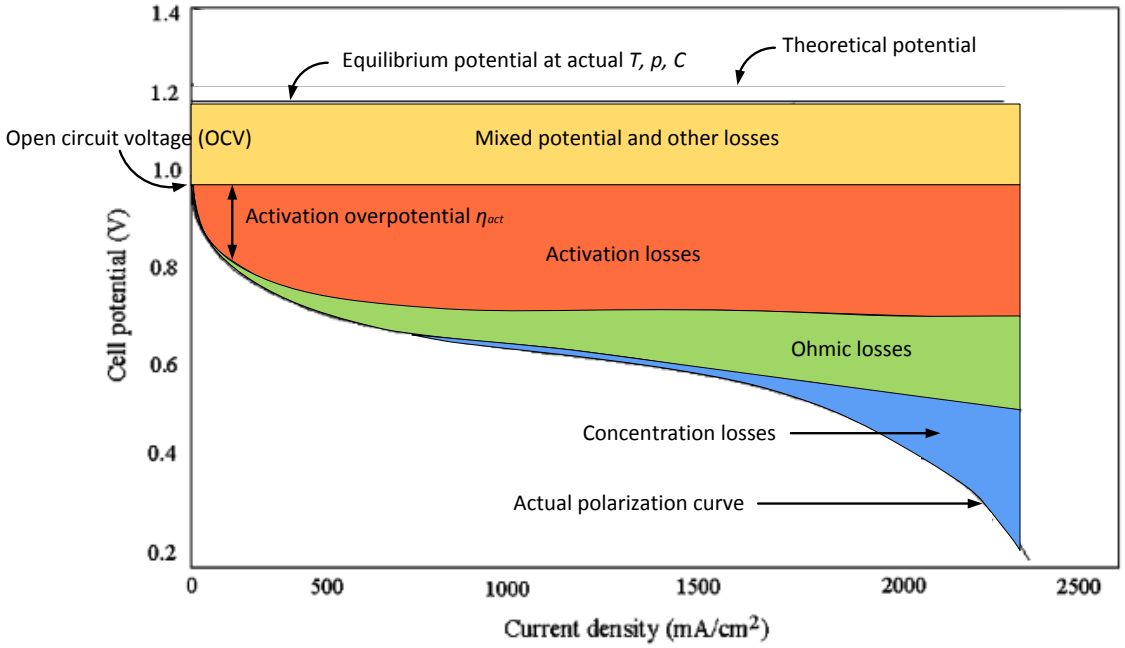

Fig. 1.11 Schematic of a polarization curve with the corresponding losses [10]

Activation loss is related to the electrode kinetics. When the electrochemical reaction proceeds, the activation barrier impedes the conversion. In other words, the reaction cost extra energy to conquer the barrier to reach the product state. This procedure is complicated, and the loss can be expressed from activation overpotential η in Butler-Volmer equation for anode and cathode respectively:

$$j_a = \left(ai_0^{ref}\right)_a \left(\frac{c_{H_2}}{c_{H_2}^{ref}}\right)^{1/2} \left[e^{\left(\alpha_a^a F/RT\right)\eta_a} - e^{-\left(\alpha_a^c F/RT\right)\eta_a}\right] \tag{1.10}$$

$$j_c = \left(ai_0^{ref}\right)_c \left(\frac{c_{O_2}}{c_{O_2}^{ref}}\right) \left[e^{\left(\alpha_c^a F/RT\right)\eta_c} - e^{-\left(\alpha_c^c F/RT\right)\eta_c}\right] \tag{1.11}$$

In Equation (1.10) and (1.11), a is ECA, i_0^{ref} is reference exchange current density, c is mole concentration, α is transfer coefficient, and η is activation overpotential. The subscript a and c indicates anode and cathode respectively.

Ohmic loss is caused by the electrical resistance and ionic resistance in a fuel cell. The electrical resistance is mainly from the solid phase of the fuel cell fixture, such as GDLs, catalyst layers, flow plates as well as the contact resistances between the layers. The ionic resistance is contributed by the polymer electrolyte membrane and generally it is the dominant factor of the total ohmic loss. As it is introduced that the low water content of membrane will lead to the significantly high ionic resistance. The ohmic loss is expressed as the ohmic overpotential in Equation (1.12):

$$\eta_{ohmic} = iR_{ohmic} = i(R_{elec} + R_{ionic}) \tag{1.12}$$

Concentration loss is due to the reactant transport effects, which is also known as mass transport loss. It usually exists in the high current density region because of insufficient reactants on the reaction site. The concentration overpotential is indicated as [2]:

$$\eta_{conc} = \frac{RT}{nF}(1 + \frac{1}{\alpha}) \ln \frac{j_L}{j_L - j} \tag{1.13}$$

In Equation (1.13), α is transfer coefficient, j_L is limiting current density indicating the situation when the reactant concentration in the catalyst layer drops down to zero.

In order to characterize these major losses experimentally, one of the widely used methods is electrochemical impedance spectroscopy (EIS). It has two measuring modes,

galvanostatic mode (constant current) and potentiostatic mode (constant voltage). In the measurement, the station gives a tiny sinusoidal perturbation with its frequency swept from high (e.g., over 10 kHz) to low (e.g., below 0.1 Hz), and meanwhile collects the responses from the system. Equivalent circuit models are generally used to differentiate the major losses by fitting the impedance spectra. A sample is shown in Fig. 1.12 derived from Randles model [11]. In the model, R_o indicates ohmic resistance; R_{ct} is charge transfer resistance contributed by activation loss; CPE is constant phase element indicating the capacitance of double layer; and W_s is Warburg element related to the mass transport loss.

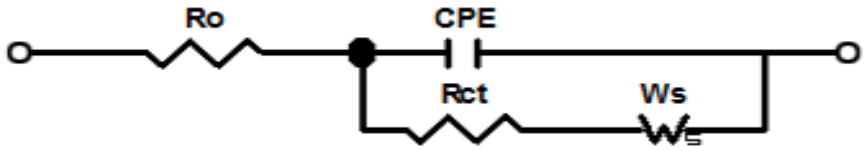

Fig. 1.12 An equivalent circuit model for PEM fuel cells derived from Randles model [11]

Another method to study fundamental mechanisms of a PEM fuel cell is cyclic voltammetry (CV), which can be used to measure the electro-chemical area (ECA) for a PEM fuel cell. A typical cyclic voltammogram for a PEM fuel cell is shown in Fig. 1.13. In the measurement, the potential is swept between two voltage limits while the current is collected. There are two current contributions, one is the capacitive charging current corresponding to the linear voltage change; the other is due to hydrogen adsorption/desorption reaction on the catalyst surface [2]. The real ECA of a PEM fuel cell can be integrated by either absorption or desorption area (shaded area) in the cyclic voltammogram.

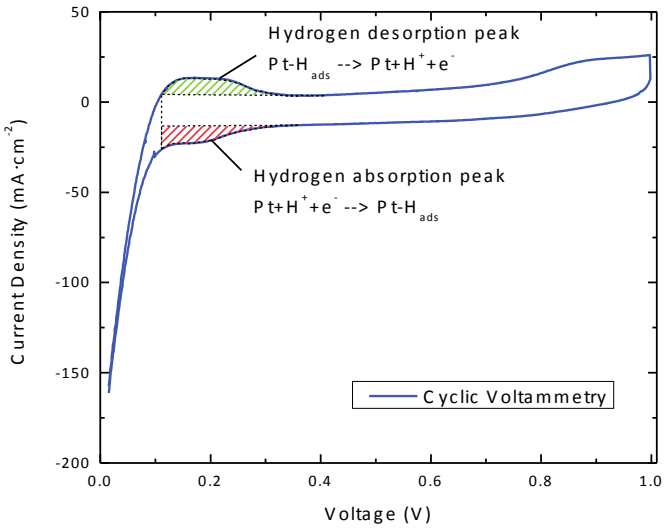

Fig. 1.13 A typical cyclic voltammogram with hydrogen adsorption and desorption reactions

CHAPTER 2

LITERATURE REVIEW

Recently, the polymer electrolyte membrane (PEM) fuel cell is well known as a promising device to convert chemical energy into electrical energy. However, there still exist some barriers for this device to be widely used compared to the conventional energy resources. Non-uniform current density in a PEM fuel cell is one of the significant problems which hinder the cell to reach higher overall performance. Thus comprehensive studies on the lateral current density distribution in a PEM fuel cell, especially under different land and channel areas, is critical for the further improvement of the cell performance and can also benefit the optimization of the cell design. Within the past decade, some researchers studied on this specific topic for the lateral current density distribution in a PEM fuel cell by both experimental and numerical methods.

2.1 Experimental studies

2.1.1 Measurement of current distribution

In the last ten to fifteen years, novel experiments were conducted to indicate the local current density performance in PEM fuel cells.

Stumper [12] first introduced three main experimental methods, i.e., partial MEA approach, subcell and current mapping technique to in-situ determine current distribution in PEM fuel cells. A lot of following designs on local current measurement were based on these three original methods. One of the methods is shown in Fig. 2.1 as the partial MEA approach.

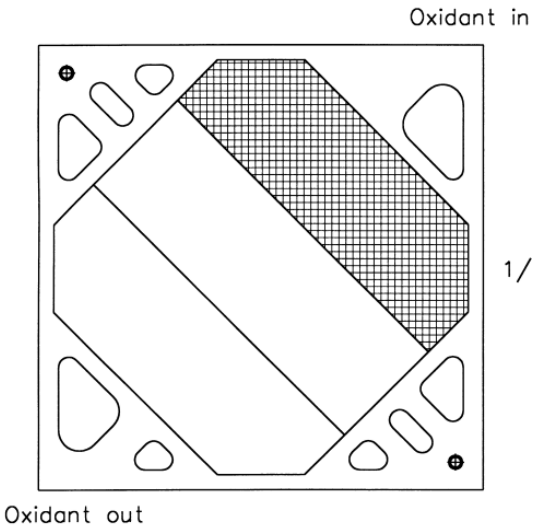

Fig. 2.1 Sketch of MEA design showing active cathode area for partial MEA [12]

Cleghorn, et al. [13] applied a printed circuit board (PCB) technology to segment the current collector and flow field to achieve the local current performance at different reactant gas flow rates and humidification strategies. The schematic of design was shown in Fig. 2.2.

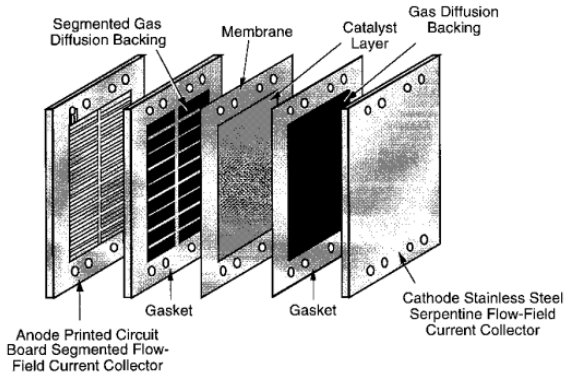

Fig. 2.2 Schematic of the printed circuit board (PCB) segmented electrode [13]

Wieser et al. [14] developed a new technique by using Hall sensors to measure current distribution in a PEMFC. The most advantage of this design was the independence of the hall sensors from the fuel cell operation.

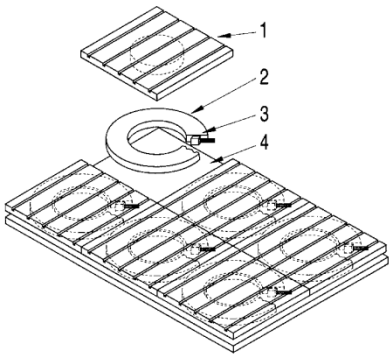

Fig. 2.3 Schematic of Hall sensors in current collector with flow field segment [15]

Brett et al. [15, 16] used the PCB technology at cathode side to measure the current distribution in a fuel cell in real-time in high resolution as Fig. 2.4 shows. Later they also investigated the membrane resistance and current distribution along a single linear channel. Results showed that under high air flow rate, current was observed increasing along the channel, and electrolyte resistance decreased consequently.

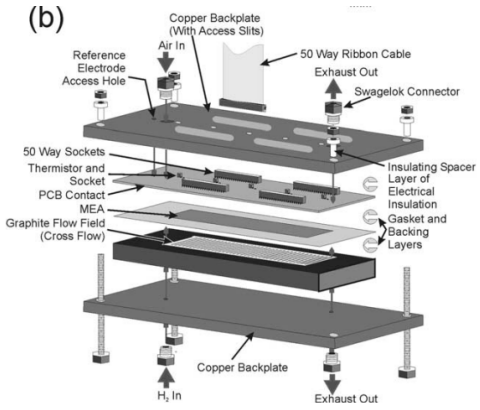

Fig. 2.4 Diagram of fixture measuring the current density distribution along the single channel [17]

Noponen et al. [17] used a special design for mapping current in a full size PEM fuel cell. The gold coated stainless steel lands were segmented to approach the current distribution. The operating temperature effect on the current distribution was studied. Under certain conditions, the optimal cell temperature and fairly homogenous current density distribution were obtained.

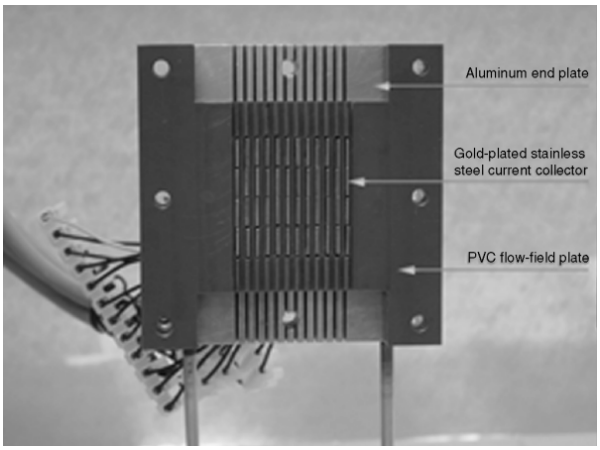

Fig. 2.5 Photograph of flow-field plate and current collectors [18]

Mench et al. [18] measured the current distribution in a full PEM fuel cell with segmented flow field and multichannel potentiostat. The effects from cathode stoichiometry and transient flooding were studied in their research.

Natarajan and Nguyen [19] used a segmented current collector and MEAs to measure current density and potential distribution along a single linear channel in a PEM fuel cell. Their experiments were conducted under two commercial gas diffusion layers, both segmented and unsegmented electrodes, and both galvanostatic and potentiostatic discharge modes.

Hakenjos et al. [20] applied special designed fixture to simultaneously obtain the current, temperature and water distribution in a PEM fuel cell as shown in Fig. 2.6. Local

currents were measured by separated stainless steel segments and partially segmented diffusion layer. Temperature distribution was obtained by infrared thermal imaging, and the water droplets as well as flooding were monitored by optical camera.

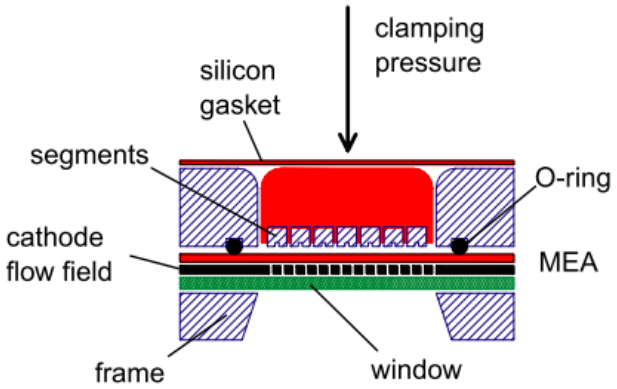

Fig. 2.6 Principle design of the test fuel cell [21]

Basu et al. [21] examined the variation of water partial pressure and temperature which affected the current density performance under stead or unsteady conditions.

Freunberger et al. [22] used potential probes to study the current density distribution under the land and channel in a sub-millimeter resolution in a PEM fuel cell as shown in Fig. 2.7. Very thin probes were inserted at the interface of gas diffusion layer and catalyst layer. And current densities were calculated by Laplace's equation with potentials and boundary conditions. Their results indicated that electrical and ionic resistances dominated the current distribution in the low current range, while mass transport limitations hindered local currents at high load of the cell. With the same design, Reum et al. [23, 24] investigated the operating parameters and flow field geometries on the current distribution and resistances under the land and channel areas. Results showed that the distribution of water and oxidant are the major cause of current differentiation. While

humidity mainly affected the membrane resistance under channels, reactant concentration influenced values of current under the land. Moreover, the geometry study indicated that the design on channel/land dimensions along the flow path might lead to more uniform current density distribution in the full size cell. Schneider and von Dahlen [25] further studied the start-stop phenomena at different locations under channel and land areas.

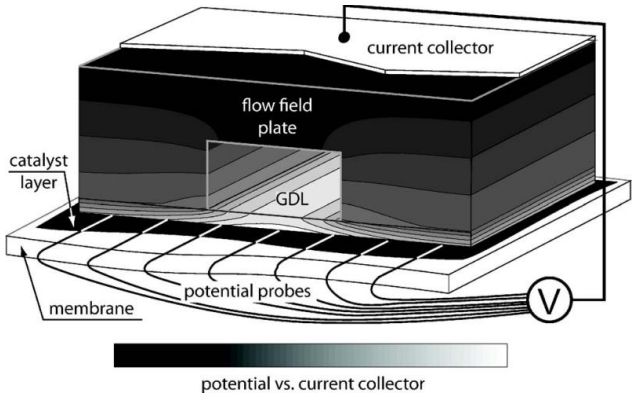

Fig. 2.7 Schematic of the potential measurement principle which used to gain the corresponding current distribution [23]

Sun et al. [26-28] designed a special measuring gasket to collect the local current by current collecting strips shown in Fig. 2.8. Due to its independence of fuel cell, no any other modification needs to be made on the components or fixture. It is easily applied to any of the fuel cell or stack, and is also inexpensive at all. They used this gasket firstly studied current density distribution from the effects of humidification temperature, cell temperature, flow rates, and operating pressure in a single serpentine channel PEM fuel cell. And in order to specify the effects from humidification temperature, they further studied both anode and cathode side with a co-flow serpentine flow field. With the same technique, they investigated the dynamic characteristics of a single serpentine channel PEM fuel cell. Their results showed that very different local dynamic responses of

current density existed throughout the fuel cell surface even when the response was very little. And the humidification temperature differentiated greatly on the dynamic response between upstream and downstream.

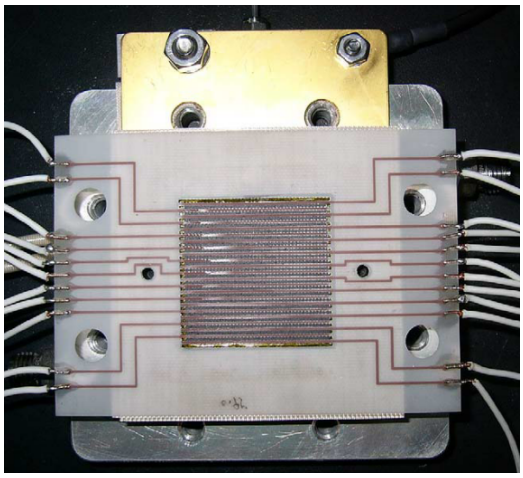

Fig. 2.8 A special designed gasket for local current study [27]

Zhang et al. [29-31] also applied this technique onto the interdigitated flow field. And they found for most operating conditions, the interdigitated flow field led to more uniform current distribution than serpentine flow field. By considering the effects from temperature distribution in a PEM fuel cell, they inserted thin thermocouples between the catalyst layer and gas diffusion layer at cathode side to simultaneously measure in-plane current and temperature distribution. The results showed that there existed a good correlation between local current density and local temperature. They further studied the reactant starvation by measuring the dynamic variation of local current density and temperature in a single serpentine flow field under both current controlled and voltage controlled mode.

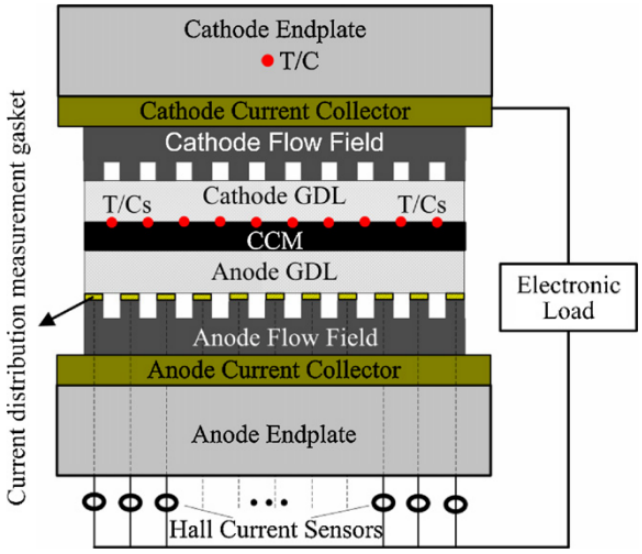

Fig. 2.9 Schematic of the design for simultaneously measurement of current and temperature distribution [30]

Wang and Liu [32] used partially catalyzed treatment on the MEAs to directly achieve the current performance at certain locations as Fig. 2.10. They found the current density performance under the land was higher than that under the channel on most operating voltages in the parallel flow field PEM Fuel Cell. Higier and Liu [33] later investigated the serpentine flow field and found the same results between the land and channel. The detail of their methodology was using the partial catalyst layer either under the land or under the channel area to obtain the single performance from either location. However, these results only indicated the average performance either from land or from the channel, the performance at the intersection place between the land and channel had not been studied at all. Besides, the accuracy was not enough to investigate the different locations through the land and channel as the previous measurement was only divided into two parts, i.e., either land or channel.

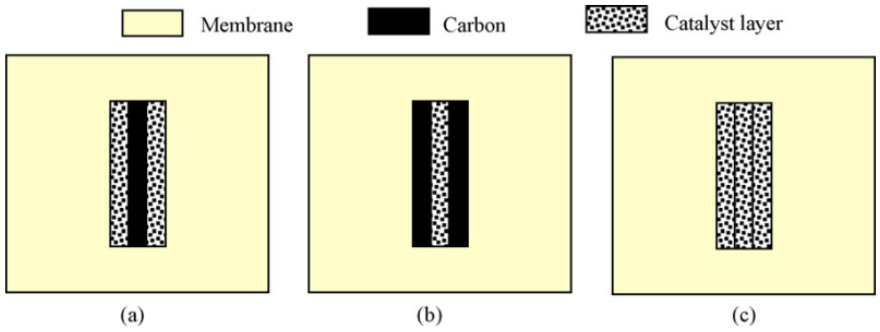

Fig. 2.10 A set of MEAs for separately measurement of current density under the channel and land [33]

Hartnig et al. [34] studied local water content effects by neutron radiographic imaging combined with resolved current density measurement. And non-uniform current density distribution was observed in the inlets and outlets due to the water flooding and starvation.

Alaefour et al. [35] used the current mapping approach by separating the flow field into sixteen square segments and studied the various flow arrangement style effects on the current distribution in the full size flow field.

Gerteisen et al. [36] used the segmented plate with serpentine configuration to measure current density distribution and high frequency resistance (HFR). The results showed current density increased with cell voltage decreasing, while HFR decreased. Besides, at the bends of channels, a large decrease of current performance existed while the HFR was not affected in most cases.

As it is indicated above, most of the current measurements were focused on the full flow field and neither differentiated the current densities between land and channel. Some of the methods might even have the congenital disadvantage on the separation of performance under land and channel locations. For instance, neither the segmented lands nor the PCB gasket could approach the performance under the channel because current

had to go through the land structure to collecting plates. And there was no direct contact between the current collectors and electrode areas under the channel. So the current performance in channel area can only be obtained by combining with that under the land. The problem was partially solved by Wang and Liu [32], and they used partial catalyzed MEAs to separately measure the performance under the land and channel. But their measurement only considered either land or channel, and eventually not enough to investigate the distribution in this lateral land-channel direction. Freunberger et al. [22] used potential probes to get the sub-millimeter resolution but the measurement was indirect due to the transformation from potential field to current density field. Thus further comprehensive study to differentiate the current density in the lateral land-channel direction at high resolution should be conducted.

2.1.2 Study by electrochemical methods

In order to study the contribution from different potential losses as well as their mechanisms, electrochemical impedance spectroscopy (EIS) and cyclic voltammetry (CV) are two effective methods widely used in PEM fuel cell area. In an EIS analysis, equivalent circuit models are needed to fit the impedance spectra thus to differentiate the effects from three major losses in a fuel cell. Models used in the PEM fuel cell study was originally from the Randles equivalent circuit model in 1947, which was widely used for electrochemical cells [37]. Due to the complexity of a fuel cell, a lot of revised models had been built to meet the requirement of the study. For instance, a parallel CPE and resistor combination was connected in series to the Randles model to simulate the diffusion effects [38-40]; a parallel capacitor and resistor combination was used instead

of the Warburg element in [41]; another CPE and resistor combination was simulated as the loss effect from the anode side [42, 43]. Eventually the model had to be fitted to the curves obtained from the EIS measurement and the different cells might have different EIS spectra.

Although it was pointed out in the previous section that the current performance under the land was different from that under the channel [22, 24, 32, 33, 44, 45], there was not too many applications with the electrochemical analysis to find out the fundamentals of the current variations between land and channel.

2.2 Modeling studies

2.2.1 General models

The earliest realistic models of PEM fuel cells were constructed in one dimension in the beginning of 1990s. Due to the different layers of polymer membrane, catalyst and gas diffusion layer, the mechanisms inside the fuel cell was studied. Springer et al. [46] firstly presented an isothermal 1-D steady state model for a PEM fuel cell. The model predicted water content of polymer membrane vs. water diffusion, protonic conductivity and electro-osmotic water drag. Bernardi and Verbrugge [47] also indicated a 1-D PEM fuel cell model to investigate the factors and mechanism which affect the cell performance. These studies had built up a valuable fundamental framework for the PEM fuel cell modeling, and even nowadays most equations in papers were still referred to these two papers.

After a few years of development on PEM fuel cell modeling, more analytical and numerical works were proposed to study the fuel cell mechanism. Gurau et al. [48]

studied analytical solution of a 1-D half-cell model. The gas diffusion layer was modeled as a series of parallel layers with different parameters and current density, mass fraction, phase potential were investigated through the layers.

Mazumder & Cole [49, 50] studied the 2-D, 3-D models with varying porosity and permeability at different layers. Dual phase potential with catalyst loading and pore size effects were formulated for electrodes; and Stefan-Maxwell for species transport. As it was modeled in single phase, no water flooding was considered and performance at the high current density was over estimated.

Du et al. [51] investigated protonic and electronic conductivity of the catalyst layer using three different packed sphere structures as the bulk conductivity was highly sensitive to the empirical parameters.

Nguyen et al. [52] studied a 3-D single phase model for the serpentine flow field. The voltage-to-current algorithm has been used to model more realistically on the electrodchemical kinetics. They found the maximal current density under the land at low load while the maximum under the channel area at the high load. But no specific differences of the property between land and channel areas were discussed.

Wang and Liu [53] investigated the interdigitated flow field with land and channel performance, and a 3-D model was applied to investigate the different cell temperature and back pressure performance compared to the experimental results.

You and Liu [54] studied 2-D two phase model was investigated to study the PEM fuel cell, and the current density through the cathode catalyst layer was increasing due to the “active region” near the membrane.

Since the higher current density existed at the channel areas, Roshandel & Farhanieh [55] studied the non-uniform catalyst loading distribution in the catalyst layer and by this pattern of higher catalyst loading at the channel, the more uniform reactant mole fraction was accomplished, therefore to obtain more uniform current density.

Nitta et al. [56] found that the uneven compression by the land structure can cause different electrical contact resistance between the GDL and catalyst layer, therefore, the current densities at the land and channel areas were not identical.

Bapat and Thynell [57, 58] built a 2-D two phase model to analyze the effects of anisotropic electrical resistivity on current density and temperature distribution in a PEM fuel cell. Their results showed that higher in-plane resistivity of GDL adversely affected the current performance.

Su et al. [59] used a porometer to get the pore distribution w/o compression on the GDL, and built up a 3-D single phase model comparison between homogeneous and non-homogeneous GDL characteristics (porosity, permeability). The results showed that current density under the channel was larger than that under the rib except at the inlet the maximum occurs near the corner of the rib due to the counter balance between mass transfer resistance and electrical resistance in the GDL. Kleemann et al. [60] also examined compression distribution in GDL with a 2-D FEM model.

Shi et al. [61] studied the effects of properties such as porosity, permeability, wettability and thickness of the GDL by compression on the saturation distribution. As the compression and deformation was modeled by the finite element analysis, the fuel cell was built with two phase 2-D model.

Chippar et al. [62] worked on a two phase 3-D single straight channel cell with the GDL compression model, which considered not only the properties of GDL such as porosity, permeability, and thickness, but the GDL intrusion under the channel was also investigated.

Garcia-Salaberri et al. [63] also developed the FEM models (isotropic and nonlinear orthotropic) to achieve the inhomogeneous assembly compression on GDL. By applying different compression stress, different GDL thickness and the radius of the land corner, the porosity and pressure distribution were obtained.

2.2.2 Modeling of current distribution

The investigation on current distribution at early age was mostly by numerical method because the experimental fixture for measuring the lateral current density was not easy to design. Any intrusion at the gas diffusion layer or catalyst layer would lead to the uncertainty for the current distribution measurement. Thus, most of the contribution in this area was the estimation of the current density distribution under various conditions by modeling.

Zhou & Liu [64] developed a general 3-D model and found the current density under the land is lower due to the obstruction of mass transfer exerted by the plate structure.

Natarajan and Van Nguyen [65] also studied the two-dimensional, two-phase transient model for the cathode of PEM fuel cell. They compared different size of the land and channel as well as the ratio, and found within all the cases the channel current density performance was higher than that at the land areas.

Berning et al. [66] investigated the three-dimensional non-isothermal model for a PEM fuel cell and their results showed that the local current density under the channel was higher than that under the land area even at low nominal current density. With the increase of the nominal current density, the fraction of the total current generated under the channel area was further increasing. Obviously, their results were contradicted with the previous study.

Meng and Wang [44] used a three-dimensional, single-phase and isothermal model to study the electron transport phenomenon inside the PEFC. By considering the lateral electrical resistance of gas diffusion layer, the current density under the channel was less than that under the land at high cell voltage; while the trend opposed at low cell voltage, where the higher current density existed under the channel areas due to the oxygen concentration.

Zhou and Liu [45]'s three-dimensional model results showed that most of the conditions led to the higher current density performance under the channel and the lateral electrical resistance of the gas diffusion layer could be negligible. Nevertheless, there was no ultimate conclusion made by all of the simulation works.

2.3 Optimization of cell performance

In order to achieve higher performance, both experimental and simulation studies have been conducted to optimize gas diffusion electrodes [67-70].

Almost two decades ago, it was pointed out that the optimal properties for catalyst layer were hydrophilicity, thinness, uniformity, with the proper ratio of ionomer and

supported catalyst [71, 72]. In their work it was found that high catalyst utilization was approached when the catalyst layer was as dense and as thin as possible.

Three years later, Uchida et al. [73-75] looked into the detailed structure and distribution of the pores inside the catalyst layer of a PEMFC and found there were two main void scales, and the “secondary pores” were much larger than the “primary pores”. By observing the micro-structure of the catalyst layer using Scanning Electron Microscopy (SEM) method, it was found that at the secondary pore scale, a large part of the platinum catalyst particles was located deep inside the agglomerates of the catalyst, which was hardly accessible for gas reactants [8]. Besides, it was pointed out that good contact between the membrane, GDL and catalyst layer was a primary factor to achieve high cell performance. It was also indicated that pressing the catalyzed GDL against the membrane might cause the ionomer to embed in the electrode structure and thereby improved the proton’s accessibility [76].

Freunberger et al. [22] found that at low current loads the maximum current density lied near the edge of the rib, while increasing the current to a higher value the reactant starvation began to take place under the rib which led to much higher current distribution under the channel. Wang and Liu [32] also found that the local current density under the land was higher than that under channels at the low current density region, which was attributed to the direct compression from the land structure. A further study was conducted by applying this method on a serpentine flow-field design and led to similar results [33]. Besides, the optimization work of the different land and channel widths showed that the indirect compression under narrow channels mitigated the current density difference between land and channel areas and improved the overall performance [77]. It

was also shown that the ECA under the land areas was higher than that under the channel due to the direct contact compression from the land structure [78].

2.4 Objective of study

From the literature survey it shows that local current densities under land and channel are not equal in a PEM fuel cell, and it may lead to the reduction of the overall cell performance. However there is no direct current density measurement with high resolution indicating the distribution in the lateral direction so far.

Thus the objective of this study is to directly measure the current density distribution in the lateral direction across land and channel areas in millimeter resolution; use electrochemical impedance spectroscopy and cyclic voltammetry to analyze the fundamental mechanisms of the lateral current density variations; apply a method called cold pre-compression treatment try to enhance the performance under the channel area; and develop a 3-dimensional numerical model to simulate the current density distribution in a PEM fuel cell with a serpentine flow field.

CHAPTER 3

CURRENT DENSITY DISTRIBUTION IN LATERAL DIRECTION

3.1 Experimental system

The schematic of the PEM fuel cell testing system is shown in Fig. 3.1. Hydrogenics® FCATS-G60 Test Station with HyWARE II™ software is used to control operating parameters, such as anode and cathode inlet temperatures, flow rates, cell temperature and back pressure, inlet humidification temperatures, etc. Pure hydrogen in the anode and air or oxygen (Airgas, Inc.) in the cathode is used as reactants respectively.

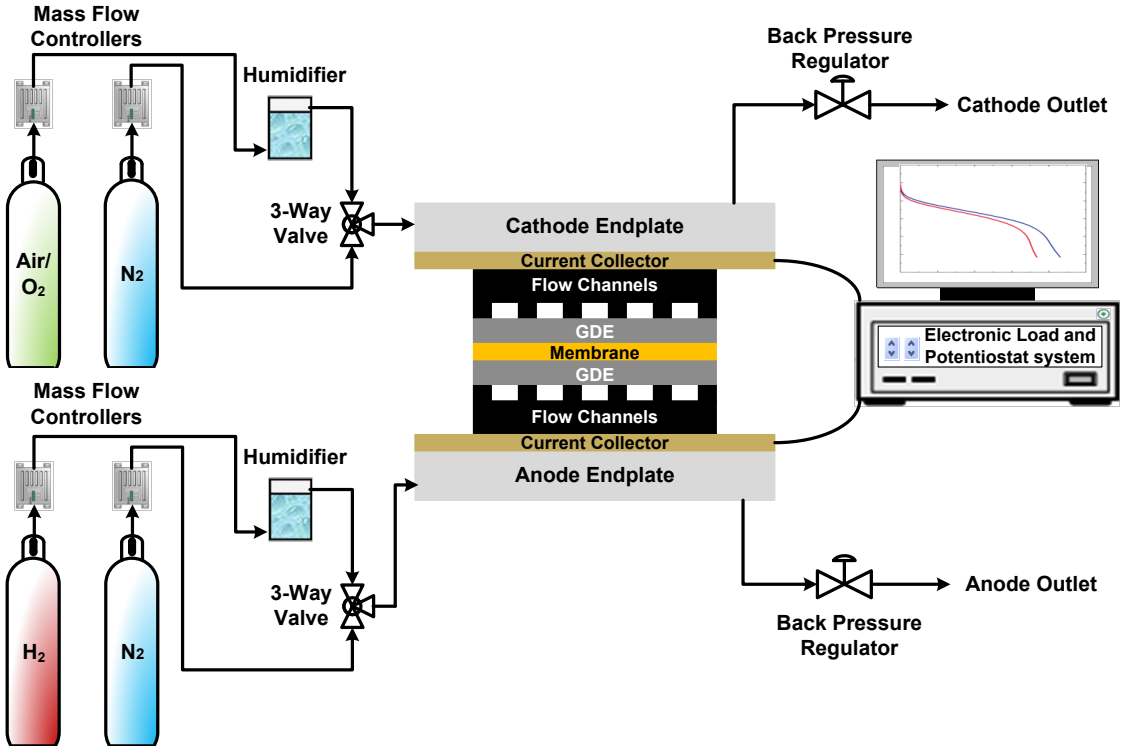

Fig. 3.1 Schematic of the PEM fuel cell experimental system

For each electrode side, reactant first flows from a high pressure tank to the station under controlled by a mass flow controller. Then it flows through a humidifier, which humidifies the reactant as well as supplies sufficient humidity to the fuel cell. A three-way valve is used to switch between the reactant and inertial gas before the inlet of the cell. Nitrogen is used here as the inertial gas to purge the station before and after tests in order to remove the reactants and products inside the cell. A back pressure regulator is also used to control the operating pressure of the fuel cell. For all of the tests, the cell operating temperature is maintained at 70^{o}C, and inlet humidification temperatures for both anode and cathode are 75^{o}C. Due to a smaller active area of the cathode electrode compared to the total membrane area, higher humidification temperatures are selected to make sure the full hydration of MEAs. At the anode side, pure hydrogen with 1000sccm constant flow rate is used; while at the cathode side, air or pure oxygen is used with various flow rates to investigate the effects from different conditions. The back pressure is set up as 2×10^{5}Pa for all the experiments. After each new MEA assembled, a break-in procedure is conducted to activate the performance of the cell. During the tests, VersaStat3® station (Princeton Applied Research, Inc.) is used to conduct electrochemical measurements. It is attached to the fuel cell with both potential and current collectors. Polarization curves are used to characterize the fuel cell performance at steady state. Results are repeated three times to obtain averages of the measurement. During the study, polarization curves are achieved by sweeping the fuel cell voltage from open circuit voltage to 0.1V with a step of $-10\text{mV}\cdot\text{s}^{-1}$.

3.2 Partially catalyzed design

The fuel cell fixture has two stainless steel end plates, with two golden-plated copper plates employed to collect the current generated from the cell. Two Teflon™ gaskets are used to seal the fuel cell as well as to protect the MEA from over-compression. MEAs are prepared in house with Nafion™-117 membrane (from Alfa-Aesar) and ELAT™ carbon cloth type GDEs (from BCSFuelCells) by hot pressing. The catalyst loadings on the gas diffusion electrodes for both anode and cathode are $0.4 mg \cdot cm^{-2}$.

In order to measure the current density variation in the lateral direction, the fuel cell has different designs for anode and cathode flow fields. At the anode side, it has a 6.6cm×6.6cm full size serpentine flow field, with 1mm channel width and 1mm land width, as shown in Fig. 3.2. At the cathode side, the flow plate is specially designed with a single serpentine channel of 2mm channel and 2mm land widths in order to separately measure the current densities at different locations. The land structure is 5.7cm in length. The main idea of the partially-catalyzed MEA method is to use a cathode gas diffusion electrode with only part of the area is loaded with catalyst while at the anode side the full electrode is used to minimizing the effects of the anode [19, 20]. As the smaller cathode electrode area limits the overall fuel cell performance, no matter how large the anode side is, the overall current collected by the station is generated only by the area catalyzed in the cathode side. Thus the local current density can be calculated from dividing the total current measured by the catalyzed cathode electrode area.

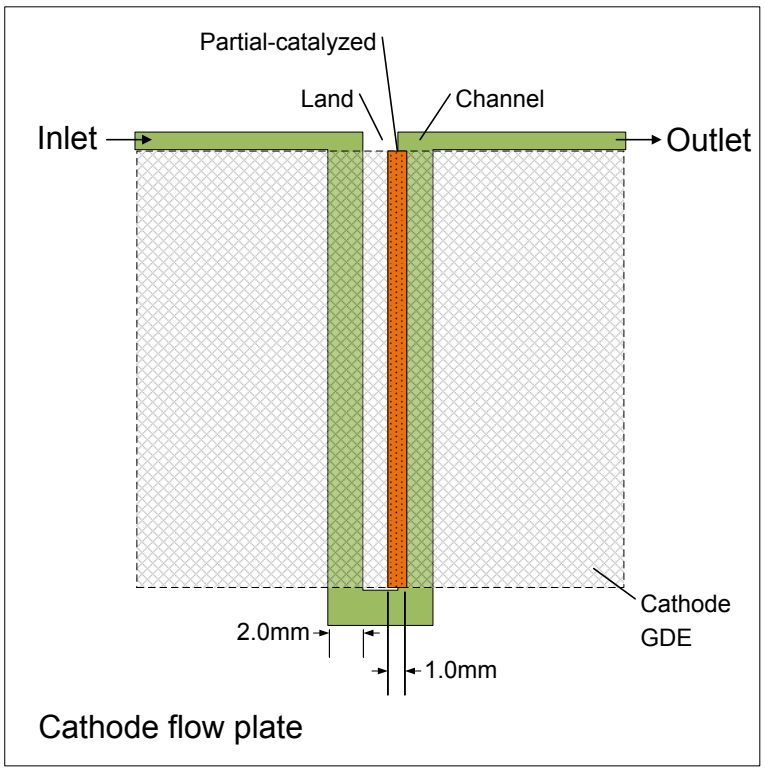

Fig. 3.2 The schematic of the cathode flow field and partially-catalyzed MEA design (top view)

The schematics of the particular MEA design and their catalyzed locations are shown in Fig. 3.3. Five partially-catalyzed MEAs are made in house, each with only a 1mm width strip catalyzed, corresponding to a location from the center of the land (Location 1) to the center of the channel (Location 5). One of the MEAs is assembled in a fuel cell at a time and the cell performance is obtained. With the current densities for all the five different MEAs, the current density distributions in the lateral direction are obtained.

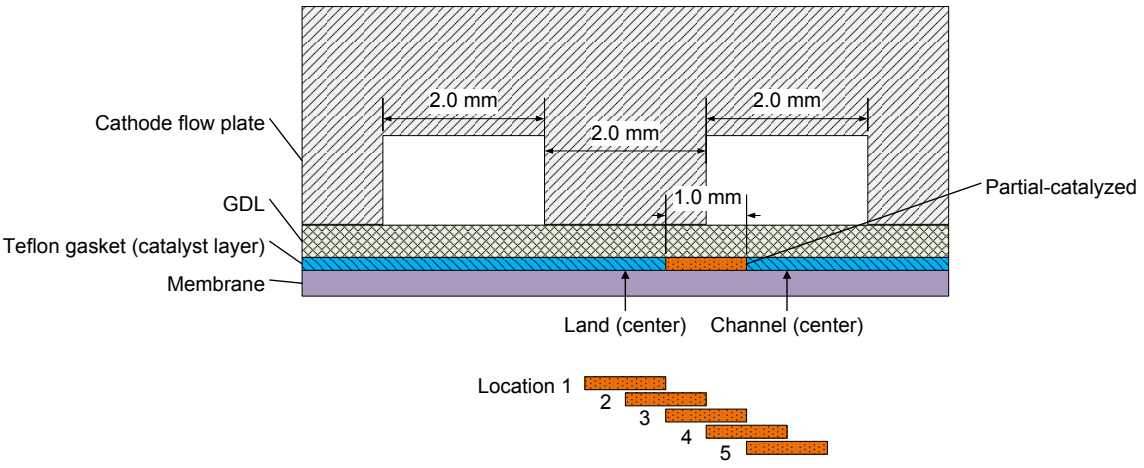

Fig. 3.3 Schematic of five catalyst loading locations across the lateral land-channel direction (lateral view)

3.3 Polarization curves

The direct measuring polarization curve results of five locations in the lateral direction are shown with air and oxygen inlet respectively. Different flow rate of the reactant at cathode side is conducted as air inlet 2000 sccm and 1000 sccm in Fig. 3.4(a) and (b), and oxygen 1000 sccm and 500 sccm in Fig. 3.4(c) and (d). It clearly shows for all cases that in the high and medium cell voltage region, the current density performance under the land is higher than that under the channel, while the maximal value locates at the center of the land and the minimum at the center of the channel in the lateral direction. However when the cell voltage keeps decreasing till a certain value, the variation from land to channel is reversed and the current density under the channel becomes higher than that under the land. It is also discussed as the direct compression effect from the fixture leads to the various current densities in ref. [32, 33]. However it should be noticed that at the low cell voltage the concentration effect is a critical issue on the local current density although the stoichiometric number at the cathode side is absolutely high. Compared with

the loss in channel area, the performance under the land is much more affected by the concentration loss. The model [63] shows the GDL porosity is significantly decreased under the land, therefore the reactant diffusion from the channel to catalyst layer under the land will be hindered correspondently. Clearly either in Fig. 3.4(a)-(b) after 0.35V or (c)-(d) after 0.25V, the mass transport effect becomes the dominant factor which leads to the current performance under the channel to be higher than that under the land area. Besides, it should also be indicated that the mass transport not only takes effects after the crossing point but before it, the polarization curve starts to bend over. Compared with the curve under the channel, the bending is more significant under the land.

Furthermore, it can be seen that the overall current density performance is significantly affected by the flow rate both for air and oxygen inlet. Investigating the curves in Fig. 3.4(a), the maximum current density is higher than that in Fig. 3.4(b). Although the special fixture is designed as a small electrode area at cathode side and the cathode reactant is abundant for the reaction, the larger flow rate still enhances the overall current density performance. As it is known that in the serpentine flow field there exists not only the diffusion from the channel area to land in GDL, but also the convection under the land due to the pressure difference between two adjacent channels. Thus the higher flow rate not only provides more reactant at the cathode side, it also enhances the diffusion and convection of the reactant transportation from the channel to the electrode surface. In addition, the liquid water generated in the cathode can be removed by the higher flow rate, which leads to the better water management in GDL and catalyst layer.

Moreover, there shows higher overall performance for the oxygen inlet compared with air at the same flow rate 1000 sccm in Fig. 3.4(b) and (c). This can be explained that the higher oxygen concentration c_{O_2} leads to the less activation overpotential η_c from the Butler-Volmer equation (3.1) at the constant current density [2, 45].

$$j = j_0^{ref}\left(\frac{c_{O_2}}{c_{O_2}^{ref}}\right)\left(e^{\alpha_a^c F\eta_c/(RT)} - e^{-\alpha_c^c F\eta_c/(RT)}\right) \tag{3.1}$$

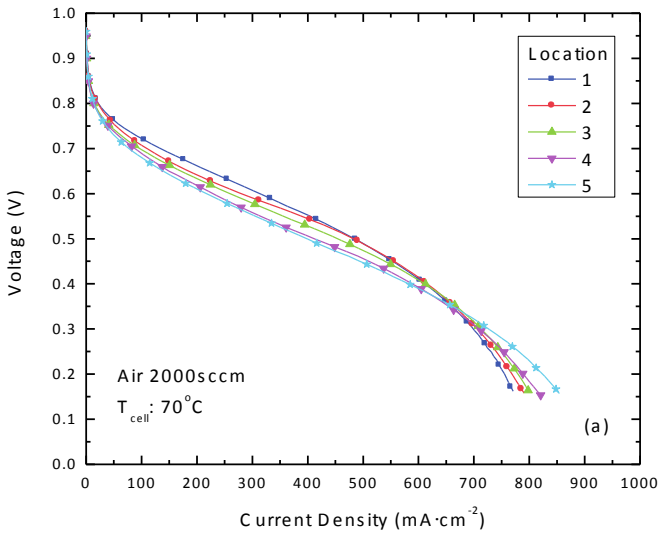

Fig. 3.4(a) Polarization curves for partially-catalyzed MEAs under different land-channel locations with air 2000sccm

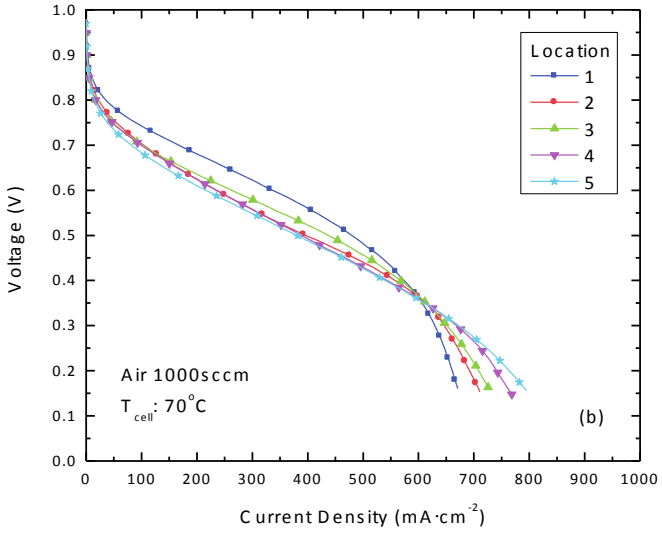

Fig. 3.4(b) Polarization curves for partially-catalyzed MEAs under different land-channel locations with air 1000sccm

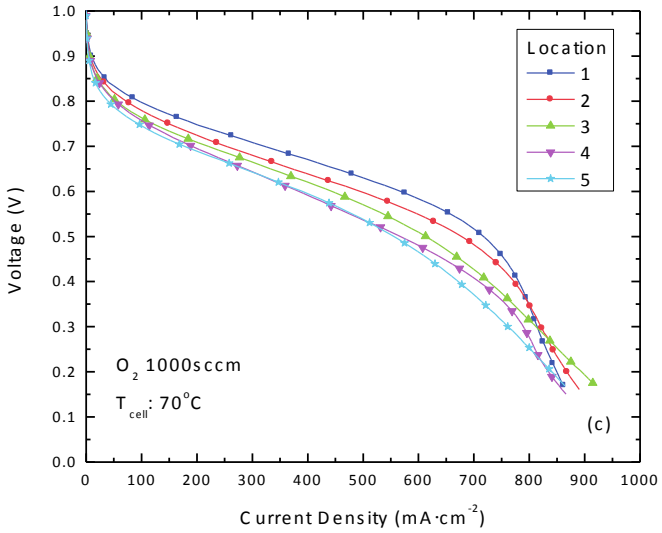

Fig. 3.4(c) Polarization curves for partially-catalyzed MEAs under different land-channel locations with oxygen 1000sccm

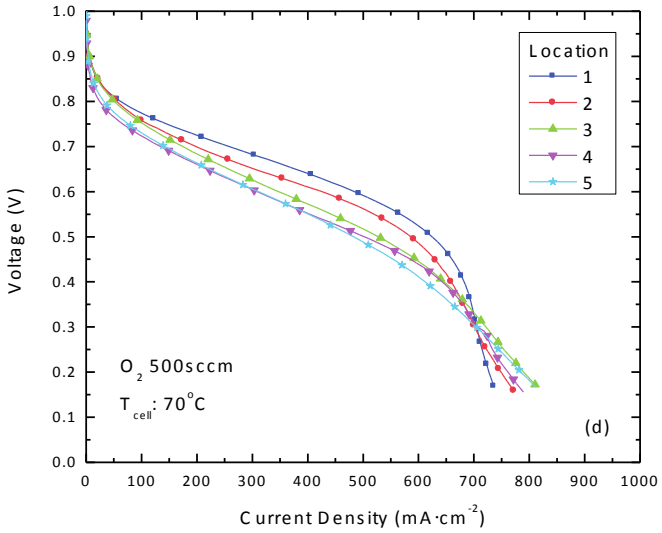

Fig. 3.4(d) Polarization curves for partially-catalyzed MEAs under different land-channel locations with oxygen 500sccm

3.4 Lateral current density distribution

The lateral current density distribution at different land-channel locations are shown in Fig. 3.5. Each interpolated point is obtained by the average result of two adjacent values which are directly measured from the experiment. It is obviously shown in Fig. 3.5(a) that for air inlet, the current density in the lateral direction decreases from the land to channel on the high cell voltage (0.8V and 0.6V). When the cell voltage is on 0.4V, the differentiation between the land and channel becomes less. While the cell voltage further decreases to 0.2V, the current density performance under the channel area obtains even higher value than that under the land. While the air inlet at the cathode side is replaced by oxygen in Fig. 3.5(c), the curves show that all the current density performance at those four voltage stages are shifted up by 100mA·cm^{-2} to 200mA·cm^{-2}. And not as the air inlet

the current variation becomes mitigated on 0.4V, it is only till 0.2V that the performance under the land becomes to be close to that under the channel.

Although for the absolute values in Fig. 3.5(a) and (c), the current density variation on 0.6V in the lateral direction appears larger than that of 0.8V, the normalized current density j_x/j_0 in Fig. 3.5(b) and (d) shows that the most significant differentiation exists at the cell voltage 0.8V. Here j_x means the current density at certain location under the land and channel in the lateral direction, and j_0 means the current density value under the center of the land structure. While on 0.8V the cell performance is mainly due to the activation loss, therefore it is obvious that the activation overpotential under the land is much less than that under the channel. When the cell voltage decreases further, the mass transport loss becomes more significant. With regardless of the ohmic resistance difference between locations in the lateral direction due to the same contact structure and membrane condition, the mass transport effect is the main factor on the current performance in the low cell voltage region. On the contrary of the activation loss higher under the channel, the mass transport loss is higher under the land due to the lower accessibility of the reactant from the flow channel to the electrode surface under the land. Thus the lower cell voltage leads to the enhancement of current density performance under the channel area.

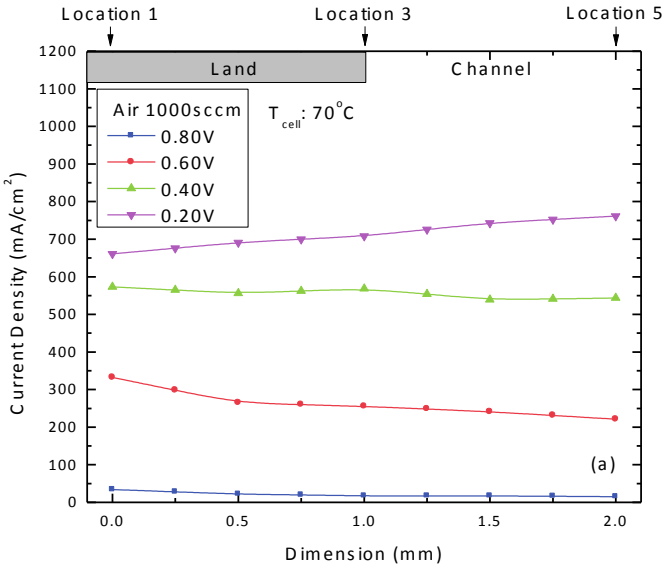

Fig. 3.5(a) Lateral current density distribution along the land-channel direction at four voltage stages with air 1000sccm

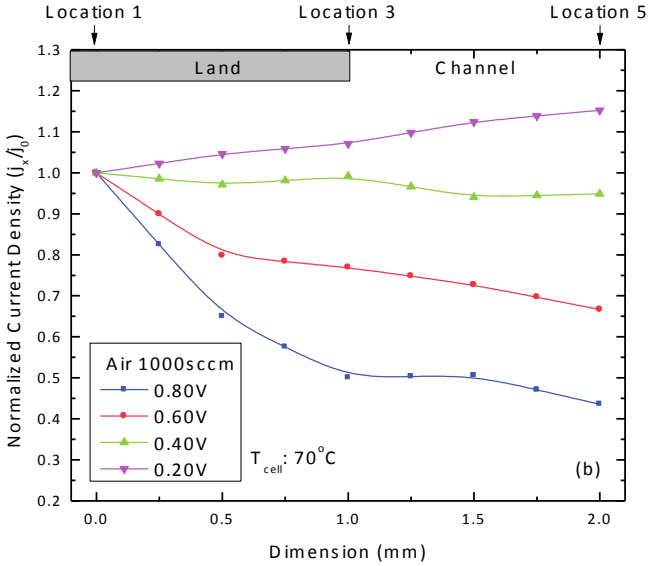

Fig. 3.5(b) Normalized lateral current density distribution along the land-channel direction at four voltage stages with air 1000sccm

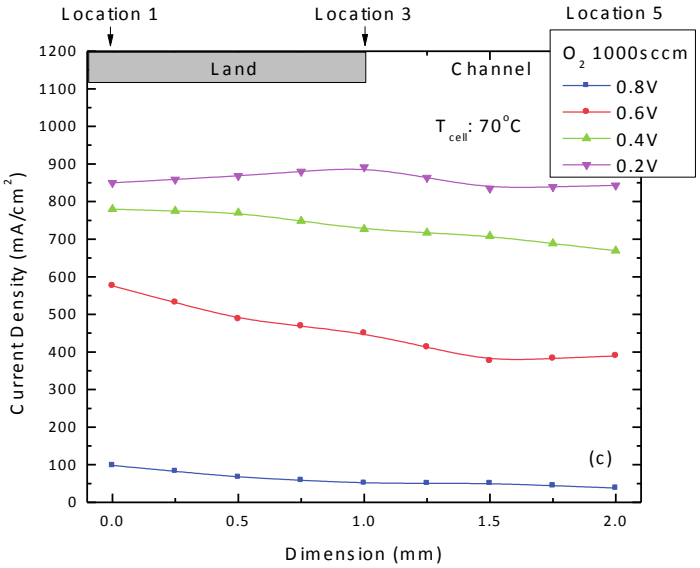

Fig. 3.5(c) Lateral current density distribution along the land-channel direction at four voltage stages with oxygen 1000sccm

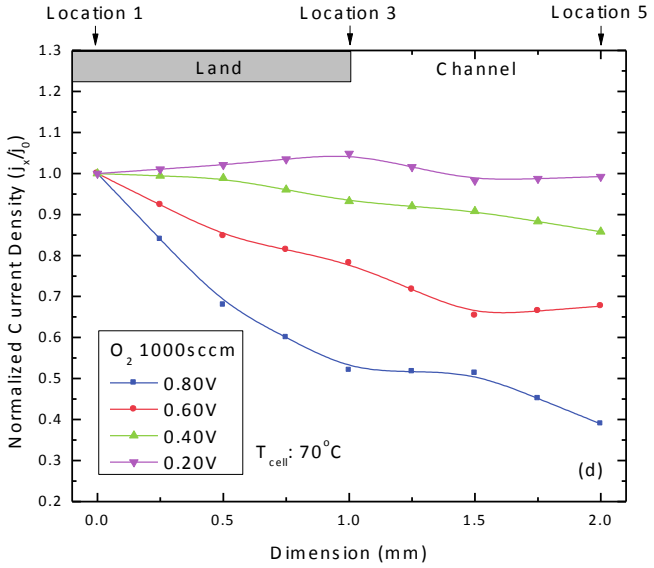

Fig. 3.5(d) Normalized lateral current density distribution along the land-channel direction at four voltage stages with oxygen 1000sccm

3.5 Cathode flow rate

The polarization curves with air flow rate 2000sccm and 1000sccm are shown in Fig. 3.6. In this figure, the current density performance at the center of land (Location 1) and channel (Location 5) is analyzed in order to study the effect of cathode flow rate on the current density distribution in the lateral direction. It shows that the performance under the land is drastically higher than that under the channel in high cell voltage region under the same flow rate, while the current density performance becomes lower under the land in low cell voltage region below 0.35V. Besides, the figure shows that the flow rate does not have big effects on the current density performance in high cell voltage region for both Location 1 and 5. This phenomenon could be explained that throughout the high and medium cell voltage region, the current density is relatively small and the air flow in the experiment has the ability to offer abundant reactant for the electrochemical reaction. As the effect from cathode flow rate is ultimately the concentration effect, the concentration does not play such an important role in high and medium cell voltage region. Furthermore, when the cell voltage decreases to 0.55V, the two overlapping curves start to detach from each other due to the concentration effects. This means that although the significant concentration loss does not exist on this voltage, the oxygen concentration starts to play an effect next in lower voltages. With further decreasing the cell voltage, the current density differentiation between two flow rates becomes even more significant and the mass transport loss leads to the sharp performance reduction for Location 1. Although the inlet reactant is sufficient in this voltage region, the effects from concentration loss on the reaction site clearly hinders the cell performance. Moreover, the flow rate variation leads to a more evident effect on the current performance under the

land compared to the channel, i.e., 100mA·cm^{-2} versus less than 50mA·cm^{-2} at 0.2V. It is because the cell is operated on a high current density value, the insufficiency of the reactant under the land is more significant than that under the channel due to the longer transport distance and lower permeability.

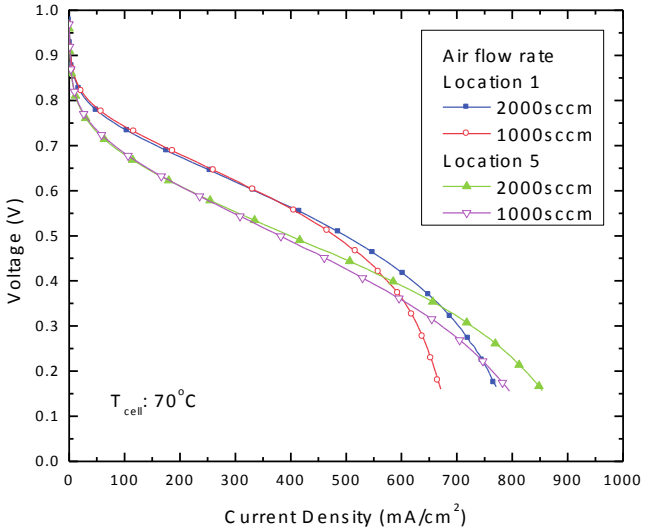

Fig. 3.6 Comparison of polarization curves between location 1 and location 5, with air flow rate 2000sccm and 1000sccm

The current density distribution in the lateral direction with flow rate 2000 sccm and 1000 sccm is also compared on cell voltage 0.6, 0.4 and 0.2V in Fig. 3.7. Eventually, these three voltage stages present the condition at activation loss, ohmic loss and concentration loss dominant region. For cell voltage 0.6V in Fig. 3.7(a), there exist almost identical values and tendency for these two flow rates. It is obvious that on 0.6V the current density is relatively small and the concentration is not a big effect on the overall cell performance. As the ohmic resistances between locations are equal, these two close curves indicate that the activation loss is not highly related to the cathode flow rate

on the high cell voltage. Moreover, the current density performance decreases drastically from the land to channel. This indicates that the activation loss under the land would be much less than that under the channel at high cell voltage.

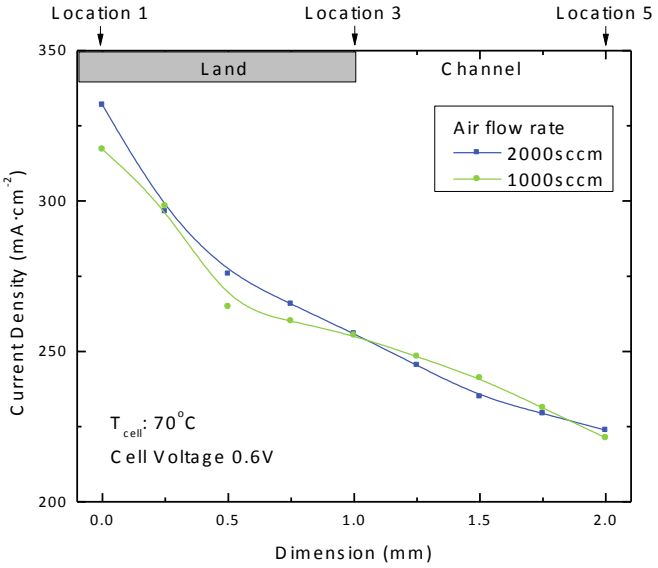

Fig. 3.7(a) Lateral current density distribution at different locations in the land-channel direction at cell voltage 0.6V with different air flow rate

When the cell voltage further decreases till 0.4V in Fig. 3.7(b), the current distribution curves become detaching from each other and the higher flow rate leads to the higher overall current density performance. As higher mass flow rate in the serpentine flow channel eventually diffuses more reactant to the gas diffusion layer and catalyst layer, the performance is increased under both land and channel areas. Furthermore, the differentiation between two flow rates is more significant in Fig. 3.7(c) due to the higher demand of the reactant at cathode side. Besides, in Fig. 3.7(b) there exists an optimal current density value at the interface between the land and channel, where the current performance both benefits from the low activation loss and high reactant accessibility. In

conclusion, the cathode flow rate has the great effects on the cell current density performance in low cell voltage region.

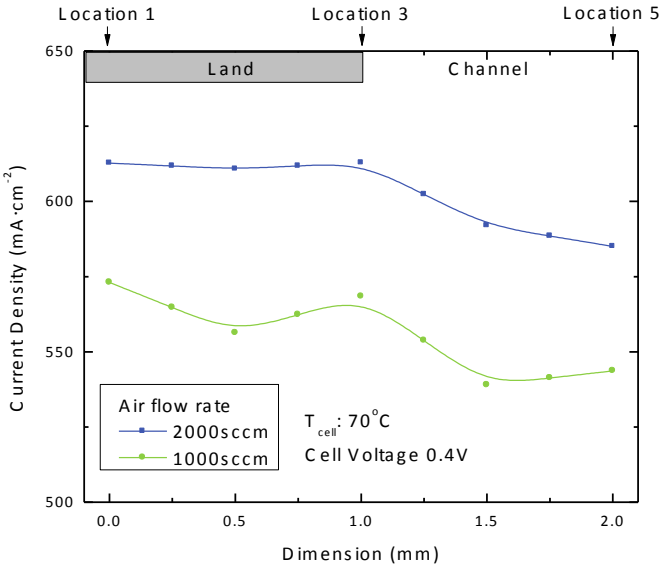

Fig. 3.7(b) Lateral current density distribution at different locations in the land-channel direction at cell voltage 0.4V with different air flow rate

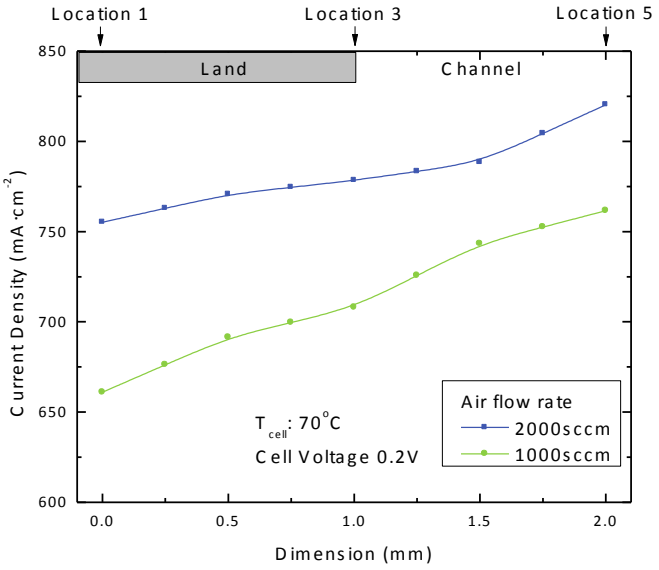

Fig. 3.7(c) Lateral current density distribution at different locations in the land-channel direction at cell voltage 0.2V with different air flow rate

3.6 Concentration effect

In Fig. 3.8, the polarization curves are compared between air and oxygen with 1000 sccm flow rate under the center of the land (Location 1) and the center of the channel (Location 5). The results show that the overall current density performance is significantly higher with oxygen inlet instead of using air at both two locations throughout the whole cell voltage range. This is due to the extremely higher oxygen concentration when the pure oxygen (99.99%) is used compared with the air inlet. As Butler-Volmer equation shows the concentration on the reaction surface is inversely related to the overpotential of the fuel cell, which means at the same current density stage the overpotential would be greatly reduced by the improvement of concentration on the reaction site. The figure also shows that the variation between air and oxygen under the channel is not as significant as the land. Especially at low cell voltage, the performance under the land is tremendously enhanced by the oxygen inlet.

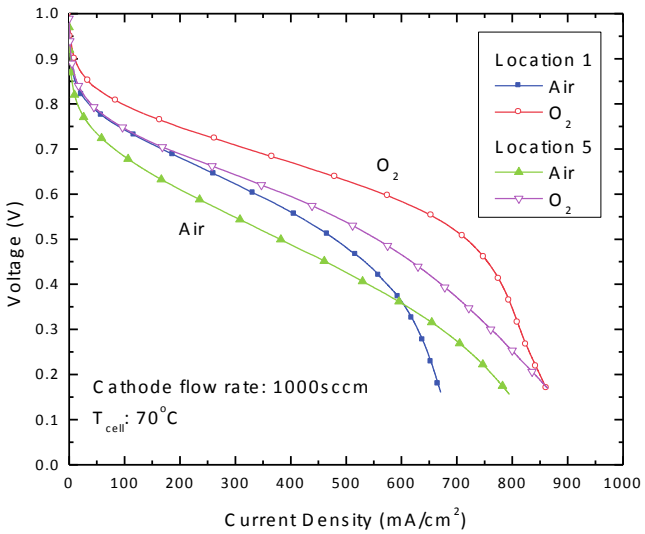

Fig. 3.8 Comparison of polarization curves between two different inlets: air and oxygen, with the same flow rate 1000sccm at location 1 and location 5

However, it should be noticed that the mass transport effects still exist under the center of the land even with the oxygen inlet. Due to the 2mm width of the land structure while only 1mm width of the cathode electrode located at its center, the oxygen accessibility to electrode surface is not as easy as the case of electrode under the channel [77]. Nevertheless, compared with the flow rate effect on mass transport in the low cell voltage region in section 3.5, clearly the improvement on the inlet concentration leads to a much more significant intensification on the cell performance. On the other hand, at center of the channel there is no significant concentration loss for either air or oxygen. As the porosity and permeability under the channel is barely reduced by the compression from the fixture, the mass transport would not be a problem for the overall performance at this location.

In addition, the current density distribution in lateral direction is compared in Fig. 3.9(a)-(c) at cell voltage 0.6, 0.4 and 0.2V. Clearly in Fig. 3.9(a) the current density performance obtains the maximal performance under the center of land for both inlets. The value shows that the current is almost doubled by the oxygen inlet compared with air. While the ohmic loss is identical for all the locations, the current density is strongly related to the activation process at this voltage. The higher performance under the land compared to channel indicates that the activation overpotential under the land is enhanced maybe due to some reasons that strengthen the active area for the electrochemical reaction.

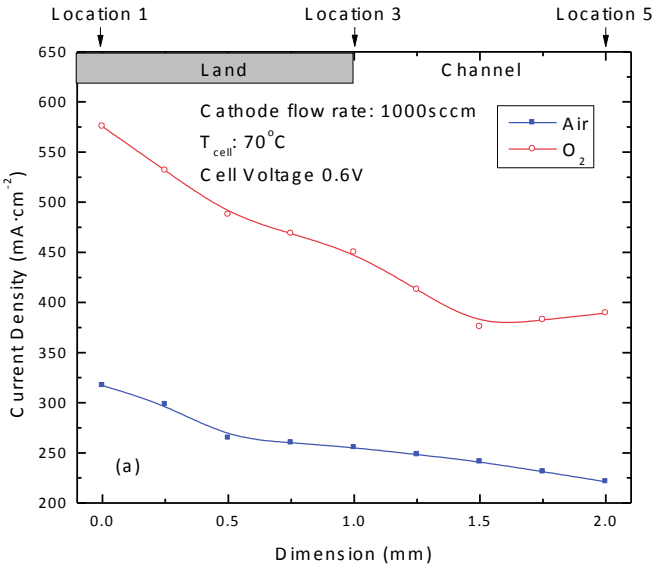

Fig. 3.9(a) Lateral current density distribution at different locations in the land-channel direction at cell voltage 0.6V with air and oxygen

When the cell voltage decreases to 0.4V in Fig. 3.9(b), the variation between land and channel area has been mitigated. It is because the cell voltage value moves towards the higher concentration dependency region. It is due to the channel area has the advantage on reactant diffusion due to the shorter path and higher permeability compared with land. With the further decrease of the cell voltage to 0.2V in Fig. 3.9(c), the tendency of the current density distribution becomes increasing from the land to channel, and the air inlet has the more significant results. Eventually at voltage 0.2V the cell loss mainly depends on the concentration effects. For air inlet, the low concentration under the land is already the critical factor which reduces the current performance; while the concentration condition is still not significant for oxygen inlet. Besides, from all of the three figures it clearly shows that the variation of the current distribution tendency with oxygen inlet is lagged compared with air due to the concentration effect, which is also coincided with

Fig. 3.8 that the crossing point of the land and channel polarization curve is at voltage 0.2V for oxygen inlet while it is at 0.35V for the air. Thus the higher concentration of the reactant at cathode side leads to the higher overall current density, and the current density performance under the land is benefited more than the channel area. In addition, the higher concentration also postpones the concentration loss domination at low cell voltage.

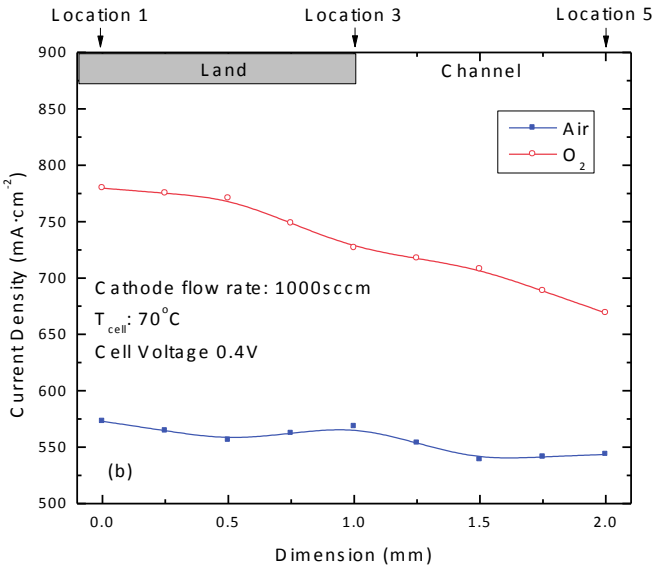

Fig. 3.9(b) Lateral current density distribution at different locations in the land-channel direction at cell voltage 0.4V with air and oxygen

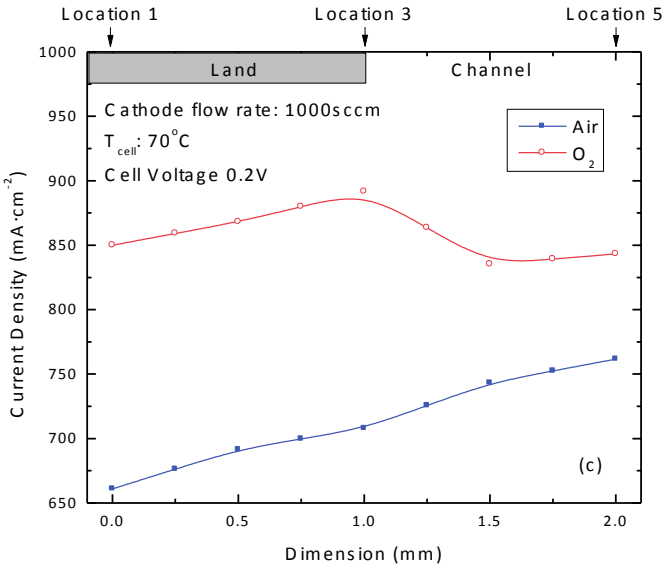

Fig. 3.9(c) Lateral current density distribution at different locations in the land-channel direction at cell voltage 0.2V with air and oxygen

CHAPTER 4

ELECTROCHEMICAL INVESTIGATION ON CURRENT DENSITY DISTRIBUTION

4.1 Electrochemical measurement

VersaStat3® station (Princeton Applied Research, Inc.) is used to measure the electrochemical impedance spectra and cyclic voltammograms. There are four connectors attached on the gold-plated current collector plate of the cell, for voltage and current measurement at both anode and cathode side during the test. In the cyclic voltammetry (CV) analysis, the aim is to study the electro-chemical area (ECA) of a PEM fuel cell. Due to the much slower kinetics of oxygen reduction reaction in the cathode compared with hydrogen oxidation reaction at anode, the working/potential electrode for the CV test is kept on the cathode side of the cell; while the reference/counter electrode is on the anode side.

The mechanism of the CV test is the hydrogen adsorption/desorption process on the catalyst particle surface in a PEM fuel cell. ECA (cm^2/mg_{Pt}) can be calculated from Equation (4.1):

$$\mathrm{ECA} = \frac{Q_H}{0.21 \times [\mathrm{Pt}]} \tag{4.1}$$

Q_H is adsorption/desorption charge per unit area of the cell (mC/cm^2), which is integrated from the adsorption/desorption peak in cyclic voltamograms. [Pt] is catalyst loading on the electrode geometry (mg_{Pt}/cm^2), and coefficient 0.21 (mC/cm^2) is the charge based on the smooth catalyst surface area for PEM fuel cells [79, 80].

The CV test is running at the same temperature and pressure conditions with polarization curve measurement. However, the cathode reactant is replaced by nitrogen gas instead of oxygen/air to study the hydrogen adsorption/desorption on the cathode catalyst surface. The flow rates for both nitrogen in the working electrode and hydrogen in the counter/reference electrode are 500sccm. The back pressure is kept on the ambient pressure. The cell voltage is swept between 0.0V and 1.0V with a scan rate of $150mV \cdot s^{-1}$. For each case five cycles are conducted to obtain the average result.

The equivalent circuit model used to fit the spectra of electrochemical impedance spectroscopy (EIS) in the present study is as Fig. 4.1 shows: a resistor (R_o) which indicates the high frequency resistance of the fuel cell; a parallel combination of a CPE and a resistor representing double layer capacitance and charge transfer resistance in the anode; a parallel connection of a CPE and a combination of a resistor with a Warburg element (W_s) in series connected indicates the charge transfer loss and the mass transport loss in the cathode.

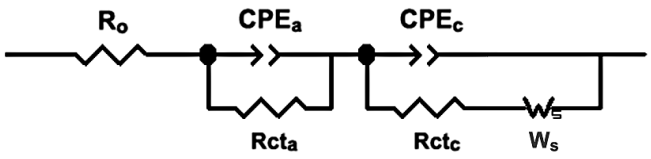

Fig. 4.1 Equivalent circuit model for EIS simulation

Constant current density mode is applied during the measurement. The impedance spectra are acquired by sweeping the frequency from 50 kHz to 0.1 Hz, with 10 points per decade. The amplitude of the AC impedance equals 5% of the DC current. The test is running at the cell temperature of 70^oC, and the humidification temperature is set of 75^oC

for both anode and cathode. This setting is based on the concern that the active reaction surface area at the cathode is relatively small and it may not be able to produce enough water to keep the high water content for the membrane. The higher dew point temperature will bring more water vapor into the cell, thus increase the relative humidity inside the fuel cell. The back pressure of the fuel cell is 2×10^5 Pa through the EIS measurement. At the anode, pure hydrogen with 1000sccm constant flow rate is used; while at the cathode side, the inlet gas is switched between the oxygen at 1000sccm and compressed air at 2000sccm. Before the test, a break-in procedure of MEA humidification and catalyst activation is conducted. The current densities used in the test are 20, 100, 200, 400mA·cm^{-2} respectively.

4.2 Cyclic voltammetry

In order to study the ECA performance in the lateral land-channel direction, there are still five MEAs with different location of catalyst loading at the cathode. The Cyclic voltammograms are shown in Fig. 4.2 and the shaded area of hydrogen desorption is integrated to approach the ECA value. Clearly the performance of two locations under the land performs much better than the others. Location 3 is at the interface between the land structure and the channel area, where the ECA is already reduced. Furthermore at Location 4 and 5 under the channel area the ECA becomes much less than that under the land locations.

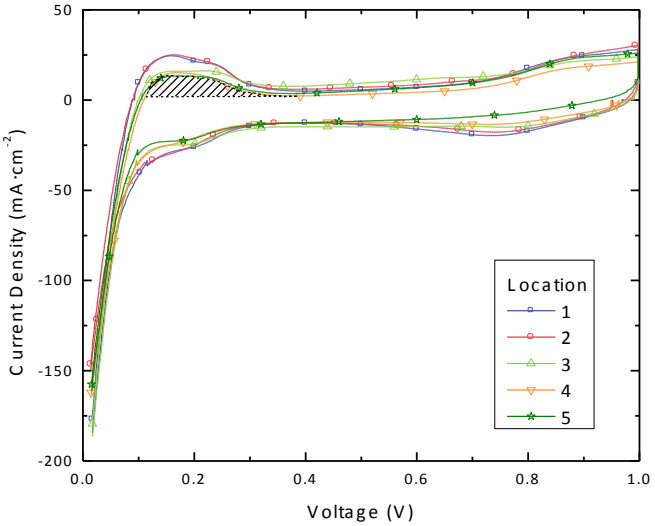

Fig. 4.2 Cyclic voltammogram of MEAs with different partially-catalyzed locations in the lateral direction

Due to the mechanism of the PEM fuel cell, there exist three major losses which reduce the overall current density performance, i.e. activation loss, ohmic loss and concentration loss. In the small current density range the activation loss dominates the cell loss, while the ohmic loss and concentration loss are not significant. Equation (4.2) is the expression of the cell current density with the function of variables ECA a ($cm^2_{Pt}\cdot mg^{-1}_{Pt}$), oxygen concentration on the reaction site c_{O_2} and activation overpotential η_{act} [2, 45]. It should be noticed that a^{ref} ($cm^2_{Pt}\cdot mg^{-1}_{Pt}$) is the reference area depends on the catalyst loading on the electrode, j_0^{ref} represents the exchange current density and $c_{O_2}^{ref}$ is the reference concentration in the gas channel.

$$j = j_0^{ref}\left(\frac{a}{a^{ref}}\right)\left(\frac{c_{O_2}}{c_{O_2}^{ref}}\right)e^{\alpha_c F\eta_{act}/(RT)} \qquad (4.2)$$

And the function of activation overpotential can be obtained as:

$$\eta_{act} = \frac{RT}{\alpha_c F}\left[\ln\frac{j}{j_0^{ref}} - \ln\frac{a}{a^{ref}} - \ln\frac{c_{O_2}}{c_{O_2}^{ref}}\right] \tag{4.3}$$

Therefore, it clearly shows that the activation overpotential is enhanced by the current density, but weakened by the higher ECA and concentration at constant temperature. Because of the negligible effects from mass transport at very small current density 20mA·cm^{-2}, the performance of ECA and the activation overpotential in the lateral land-channel direction is compared in Fig. 4.3. The activation overpotential is calculated from the polarization curves Fig. 3.1(b) as open circuit voltage subtracts the cell voltage at current density 20mA·cm^{-2} [81]. Clearly at certain current density, higher ECA leads to the lower activation overpotential. While the ECA value may be positively affected by the proper compression from the land structure [78, 82], the performance under the land area is increased compared to the channel. Besides, the distribution of ECA in the lateral direction is curve fitted by polynomial function. Thus the reduction of the current density performance from land to channel in the polarization figure is due to the decrease of ECA in the land-channel direction.

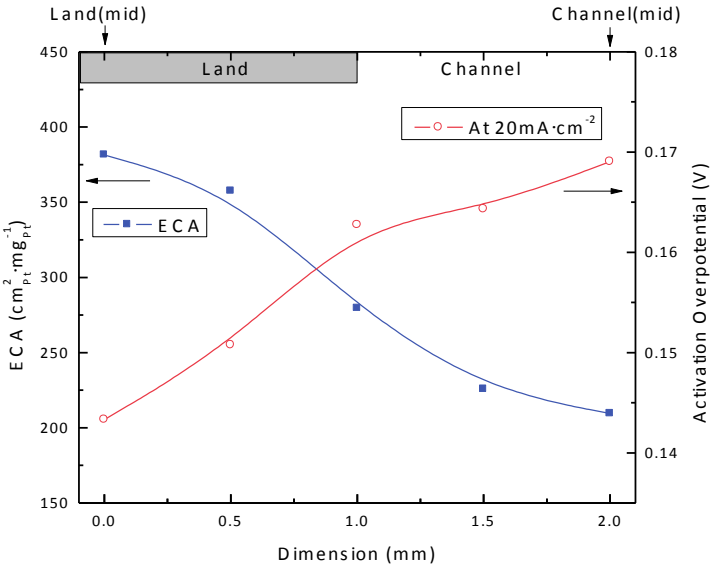

Fig. 4.3 Comparison between the ECA from CV test and the activation overpotential at cell current density 20mA·cm^{-2} from polarization curve

4.3 Electrochemical impedance spectroscopy

Although the ECA variation explains the current density reduction from land to channel in the high cell voltage region, the reversal tendency in the very low voltage stage 0.2V in polarization curves is still not clear. Therefore the EIS method is applied to investigate the individual effect from the main losses in a PEM fuel cell. By changing the current density from 20 to 400mA·cm^{-2} the impedance spectra under five locations with hydrogen inlet 1000 sccm and air 2000 sccm are shown in Fig.4.4-4.6 respectively. The equivalent circuit model is used to fit the plots and the results are listed in Table 4.1-4.3. Due to the limited mass transport distance in the electrode in a PEM fuel cell, usually there exists a third semicircle in low frequency range which represents the concentration effect. While the Warburg effect is unavailable in the first two cases, the mass transport effect is not significant at all due to the small value of current density.

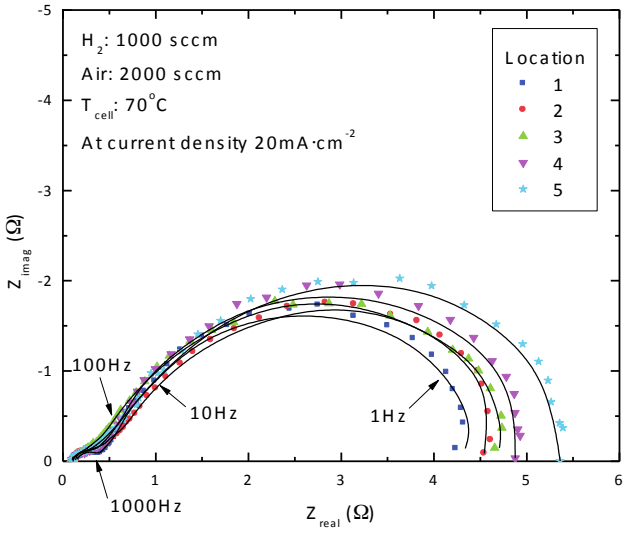

Fig. 4.4 Electrochemical Impedance Spectroscopy with partially-catalyzed MEAs at lateral land-channel locations. Condition: At current density of 20mA·cm^{-2}; Cell temperature 70^{o}C; Hydrogen flow rate 1000 sccm; Air flow rate 2000 sccm.

Table 4.1 Fitting values with air inlet at current density 20mA·cm^{-2}

Location	**R_o(Ω)**	**Rct_a(Ω)**	**Rct_c(Ω)**	**CPE_c**	
				C(mF)	α
1	0.10	0.362	4.054	16.42	0.86
2	0.10	0.362	4.382	15.83	0.86
3	0.10	0.362	4.457	13.49	0.86
4	0.11	0.362	4.777	12.79	0.84
5	0.11	0.362	5.303	10.70	0.80

Clearly in all three figures at high frequency, the intersection point between the curve and the Z_{real} axis which is widely considered as the ohmic resistance is almost constant.

Although paper [83] states that the ex-situ direct compression from the structure may lead to the lower total contact resistance under the land, it is not significant in our in-situ study. Besides, it has been experimentally verified that the lateral electrical resistance in the gas diffusion layer is negligible [32]. In Fig.4.4, the main semicircle is contributed by the charge transfer resistance and double layer capacitance at the cathode side. Due to the sluggish oxygen kinetics, the charge transfer resistance from the cathode is the main part of the cell loss at this low current stage. Obviously the charge transfer resistance at the cathode increases from the land to channel area, while the double layer capacitance obtains the higher values under the land rather the channel. As Fig. 4.3 clearly shows the higher ECA under the land leads to the lower activation overpotential, the charge transfer resistance could be calculated by the partial derivative of overpotential by current, therefore the lower charge transfer resistance under the land. On the other hand, the double layer capacitance approaches the maximal value under the land. Obviously the greater electrochemical active area under the land is able to hold more charges on the reaction surface, which means the higher capacitance.

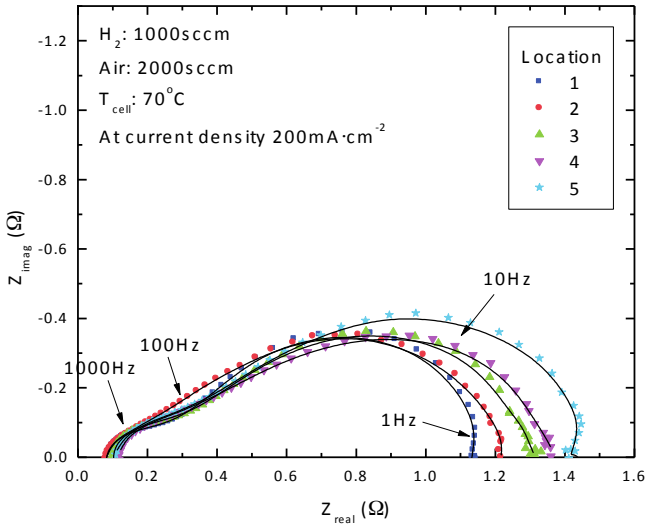

Fig. 4.5 Electrochemical Impedance Spectroscopy with partially-catalyzed MEAs at lateral land-channel locations. Condition: At current density of 200mA·cm^{-2}; Cell temperature 70^{o}C; Hydrogen flow rate 1000 sccm; Air flow rate 2000 sccm.

Table 4.2 Fitting values with air inlet at current density 200mA·cm^{-2}

Location	**R_o(Ω)**	**Rct_a(Ω)**	**Rct_c(Ω)**	**CPE_c**	
				C(mF)	α
1	0.09	0.210	0.860	10.30	0.83
2	0.09	0.210	0.933	8.42	0.81
3	0.10	0.210	1.003	7.22	0.78
4	0.11	0.210	1.045	5.45	0.78
5	0.11	0.210	1.141	4.36	0.78

Besides, the tiny semicircle above the frequency of 1 kHz is contributed by the anode side effect which is barely changed among the locations. As most of the papers show this

semicircle is independent of the cathode supply or the operating conditions [43, 84-86], Boillot et al. [42] found the high frequency loop was increased with the dilution rate of hydrogen. Romero-Castanon et al. [87] also indicated the high frequency region was not associated with any faradaic process or mass transport limitations, but only subsequently related to the unvaried construction of the MEAs. Freire and Gonzalez [88] stated the independence was attributed to the distributed resistance effects in the electrolyte within the catalyst layer. It is concluded that the semicircle in this high frequency region above 1000Hz is independent of the locations or the operating conditions in this study.

When the current density is increased to 200mA·cm^{-2} the results are shown in Fig. 4.5 and Table 4.2. It has almost similar variation tendency between the land and channel locations as 20mA·cm^{-2}. However, the values of the charge transfer resistance are greatly decreased at increased current density stage. Besides, the semicircle is more depressed due to the reduction of the phase angle α, which also means the CPE is more deviated from pure capacitance effect at high current density.

It also shows the EIS spectra at current density 400mA·cm^{-2} in Fig. 4.6 and Table 4.3. The charge transfer resistance and double layer capacitance at the cathode side obtain the same variation tendency at this current. However it is obvious in the figure that there comes out a third arc after frequency 1Hz. This means the mass transport loss becomes more significant than the previous two current stages. And the Warburg element cannot be negligible anymore and must be valued in the equivalent circuit model. Due to the small cathode electrode area, the arc from the mass transport loss is not well formed. But the results show that the Warburg resistance under the land is higher than that under the

channel area, which is attributed to the higher electrode porosity and permeability under the channel.

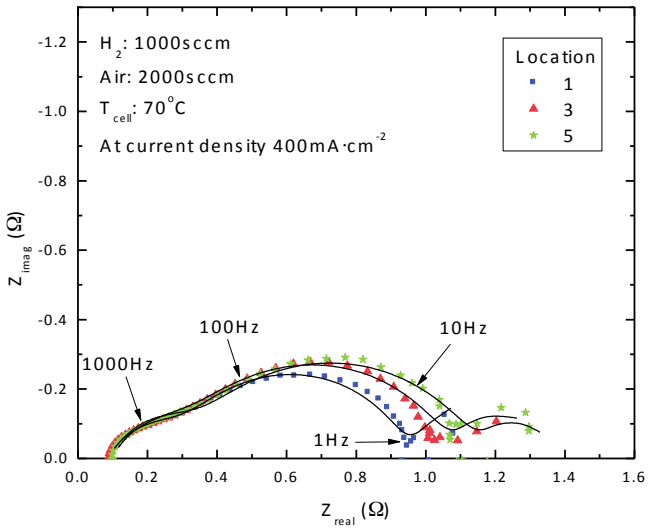

Fig. 4.6 Electrochemical Impedance Spectroscopy with partially-catalyzed MEAs at lateral land-channel locations. Condition: At current density of 400mA·cm^{-2}; Cell temperature 70^{o}C; Hydrogen flow rate 1000 sccm; Air flow rate 2000 sccm.

Table 4.3 Fitting values with air inlet at current density 400mA·cm^{-2}

Location	**R_o(Ω)**	**Rct_a(Ω)**	**Rct_c(Ω)**	**CPE_c**		**W_s**	
				C(mF)	α	Rmt(Ω)	τ(s)
1	0.09	0.235	0.597	5.01	0.84	0.369	5.05
3	0.10	0.235	0.708	3.53	0.80	0.293	2.06
5	0.10	0.235	0.791	2.28	0.76	0.235	1.35

4.4 Lateral distribution

The distribution of the charge transfer resistance, double layer capacitance and mass transport resistance at 20mA·cm^{-2} and 400mA·cm^{-2} is shown in Fig. 4.7 and Fig. 4.8 respectively. Clearly the charge transfer resistance increases from the land to the channel area, while inversely the double layer capacitance at the cathode side decreases due to the reduction of the ECA. The mass transport resistance is mainly affected by the concentration loss that the channel area is more feasible for oxygen to diffuse in the catalyst layer onto the electrochemical active surface. Thus the mass transport resistance also decreases from land to channel area. Moreover, by analyzing equation (4.3) the charge transfer resistance R_{ct} of the fuel cell can be obtained as the derivative of the activation overpotential by current. Therefore by using current i (A) instead of the current density j (A·cm^{-2}), the charge transfer resistance becomes the function of current, ECA and concentration:

$$R_{ct} = \frac{\partial \eta_{act}}{\partial i} = \frac{RT}{\alpha_c F}\left[\frac{1}{i} - \frac{1}{a}\cancel{\left(\frac{\partial a}{\partial i}\right)} - \frac{1}{c_{O_2}}\left(\frac{\partial c_{O_2}}{\partial i}\right)\right] \tag{4.4}$$

It should be noticed that although the charge transfer coefficient α_c is mostly independent of the operating conditions, the artificial values may be obtained in the experiment during the cell voltage change due to the mass transport loss [89, 90]. While the concentration derivative is negative inside the bracket, the concentration term provides the positive effect on the charge transfer resistance. Nevertheless, the concentration variation under the land and channel is still unavailable and should be further investigated in future.

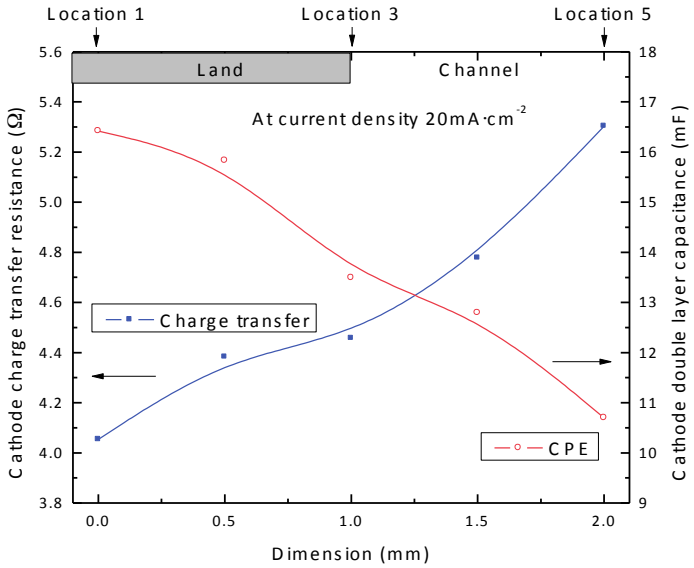

Fig. 4.7 The distribution of charge transfer resistance and double layer capacitance at current density 20mA·cm^{-2} in cathode side

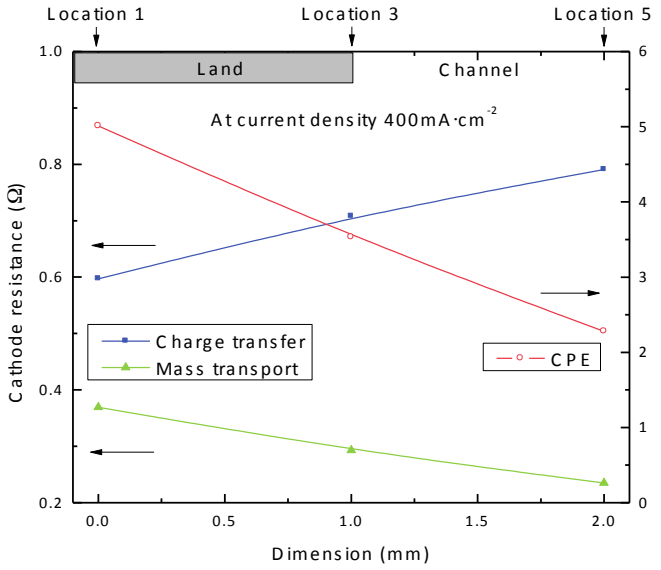

Fig. 4.8 The distribution of charge transfer resistance, mass transport resistance and double layer capacitance at current density 400mA·cm^{-2} in cathode side

4.5 Current density effect

As equation (4.4) indicates that the charge transfer resistance is also a function of the current, the impedance spectra are also conducted under different current stage of the cell. It shows the variation of cathode charge transfer resistance at location 1 and 5 from current density 20mA·cm^{-2} to 400mA·cm^{-2} in Fig. 4.9.

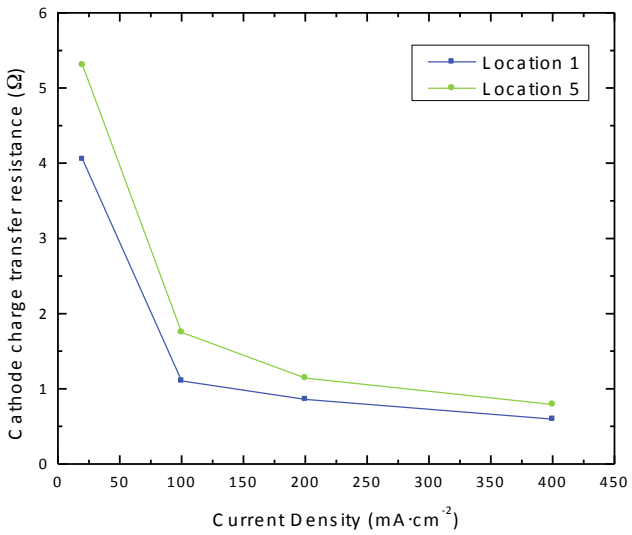

Fig. 4.9 Cathode charge transfer resistance variation with current density at Location 1 and 5. Condition: Cell temperature 70^{o}C; Hydrogen flow rate 1000 sccm; Air flow rate 2000 sccm

Obviously the increasing current density leads to the reduction of the cathode charge transfer resistance. If there only considered with the current term, the variation should be linear with the current. But when the current is increased, the concentration on the catalyst surface is also reduced. Besides the concentration is very sensitive to the current change at high current density which means its gradient is also larger than the low current stage. As the concentration variation is reversed of the current, it has the negative sign for

the concentration gradient term in the bracket, thus the positive effect on the charge transfer resistance. Clearly higher current leads to the higher effect from the concentration term, which deviates the linear change but enhance the charge transfer resistance in the high current density range.

4.6 Concentration effect

It is shown in Fig. 4.10 and Table 4.4 that the oxygen inlet has the same variation tendency with the air inlet above. However the cathode charge transfer resistance is reduced for all cases compared with the air inlet. As the oxygen inlet provides much more reactant for the fuel cell, the concentration on the reaction surface c_{O_2} as well as its gradient with current between different land-channel locations are mitigated in equation (4.4). Regardless of the charge transfer coefficient artificial variation α_c at low current density, the only contribution on the different charge transfer resistance is from the ECA term. It is possible that due to the more water produced by increasing current, which decreases the active reaction surface, also leads to the negative sign in the bracket of ECA term.

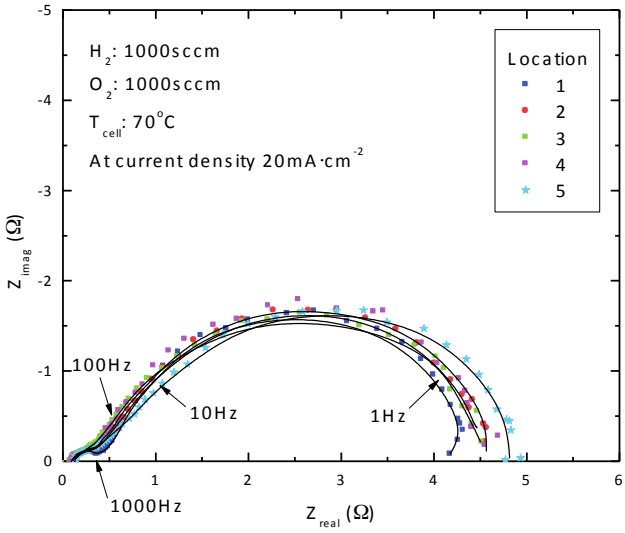

Fig. 4.10 Electrochemical Impedance Spectroscopy with partially-catalyzed MEAs at lateral land-channel locations. Condition: At current density of 20mA·cm^{-2}; Cell temperature 70^{o}C; Hydrogen flow rate 1000 sccm; Oxygen flow rate 1000 sccm

Table 4.4. Fitting values with oxygen inlet 1000 sccm at current density 20mA·cm^{-2}

Location	**R_o(Ω)**	**Rct_a(Ω)**	**Rct_c(Ω)**	**CPE_c**	
				Q(F)	α
1	0.10	0.297	4.028	11.33	0.85
2	0.10	0.297	4.150	10.26	0.84
3	0.10	0.297	4.332	9.22	0.81
4	0.11	0.297	4.421	8.60	0.81
5	0.11	0.297	4.479	7.96	0.81

CHAPTER 5

COLD PRE-COMPRESSION ON MEMBRANE ELECTRODE ASSEMBLY

5.1 Cold pre-compression

The cold pre-compression treatment is applied at room temperature (ca. 25°C). To differentiate this compression process from the commonly known hot-press process for making the MEAs, this process is termed as *cold pre-compression* as Fig. 5.1.

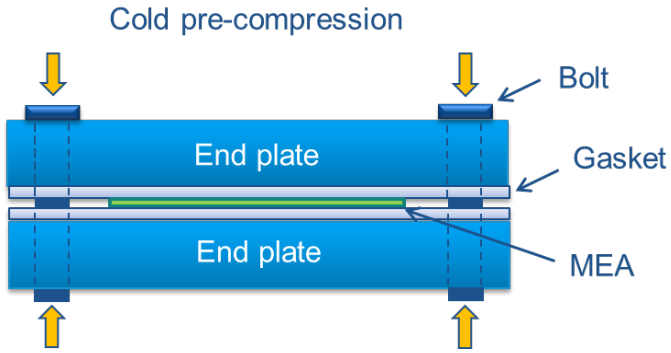

Fig. 5.1 Schematic of cold pre-compression on MEA

In this procedure, the MEA is placed between two hard Teflon sheets, which are in turn sandwiched by two stainless plates using eight ¼-inch bolts. Five compression levels are applied on the different MEA samples. The tension force on the MEA can be converted by the bolt equation (5.1). As the diameter of the bolt listed in USA Size Designation (UNF), the tension force is calculated from the empirical equation:

$$T = 0.2 \times D_n \times F \tag{5.1}$$

Where T is the torque on each bolt in (N-m), D_n is the nominal diameter in (m), and F is the tension force (N) on the MEA produced by the assembly bolts. Thus the pressure

on the MEA can be calculated from the tension force divided by the total contact area. As the pre-compression method deforms the GDE structure, the thicknesses under different cold pre-compression conditions are also listed. The values are the average of multiple measurement results. It is important to point out that the thickness of the GDE remains almost constant after it was removed from the assembling plates, thus the compressions are considered as permanent. Fig. 5.2 provides the variation of thickness of the GDEs after the five different cold pre-compression levels. From zero pressure to the first compression stage of 33×10^5Pa, the MEA thickness decreases to 92% of its original value and the decrements become smaller with further increase in the pre-compression pressure.

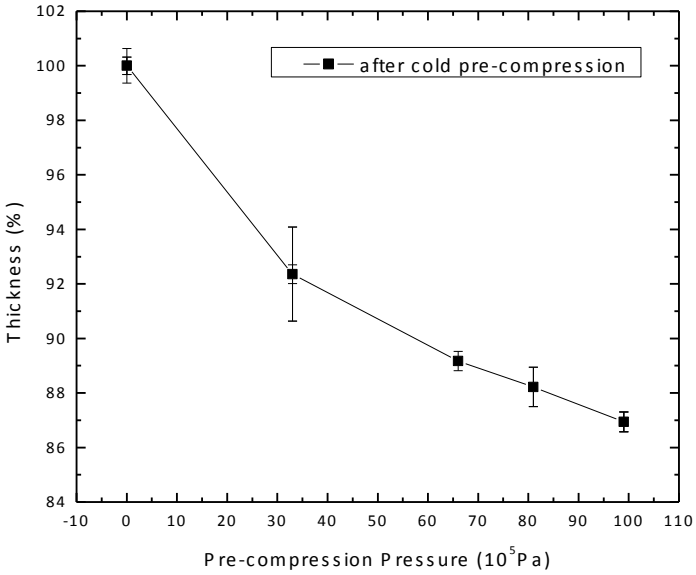

Fig. 5.2 The comparison of MEAs thickness percentage after different pressures of cold pre-compression treatment

5.2 Polarization curves

The results of polarization curves are shown in Fig. 5.3. Both the cell temperature and the flow rate of gases are maintained constant during the tests. The performance of five fuel cells, one used the original GDE without pre-compression and the other four each used a GDE that was treated with different level of cold pre-compressions, were studied. The experimental results definitively show that the performance of the fuel cell can increase significantly by the cold pre-compression treatment. However, the results also show that over-compression can have a detrimental effect on the cell performance, i.e., if the MEA has been over-compressed, the performance decreases and it can be even lower than that for the untreated MEA.

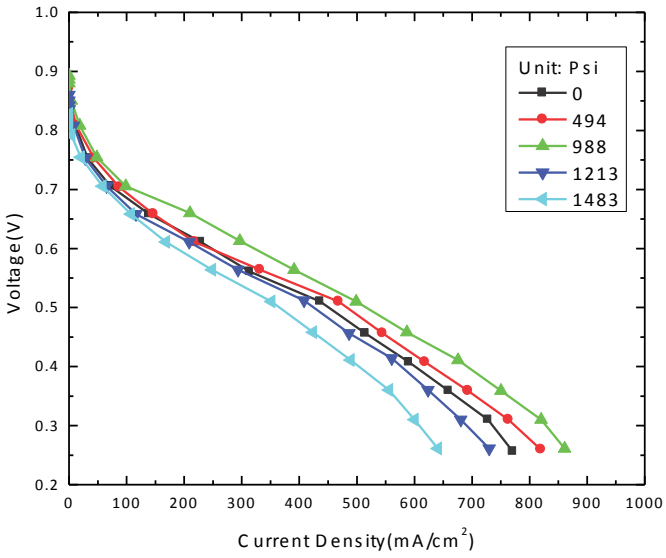

Fig. 5.3 Performance of polarization curves with five different cold pre-compression pressures: 0, 33, 66, 81, 99 (10^5Pa). Temperature: 70^{o}C; hydrogen flow rate 8.33 cm^3/s; air flow rate 33.33 cm^3/s

At the cell voltage 0.75V, the current density of the fuel cell using the untreated MEA is about 35 $mA \cdot cm^{-2}$; while the current density of the fuel cell using the pre-compressed MEA at a pressure of 66×10^5Pa increases to 50mA/cm^2. Then the cell performance decreases with the further increase in the pre-compression pressure. At the treatment pressure of 99×10^5Pa, the current density is significantly lower than that without the cold pre-compression. In this cell voltage region, the dominant loss is the activation over-potential due to the slow kinetics of the oxygen reduction reaction (ORR). From Fig. 5.3, it can also be deducted that the pre-compression do not have very large effect on the ohmic loss. Thus neither the pre-compression affects the contact resistance in an assembled fuel cell, nor does it affect the ionic resistance of the membrane. Besides, at the very high pre-compression pressure of 99×10^5Pa, the polarization curve shows somewhat increased mass transport losses.

5.3 Electrochemical impedance spectroscopy

A typical equivalent circuit model called Randles circuit model for the PEM fuel cell is used as shown in Fig. 5.4 [11]. In a PEM fuel cell, since the reaction at the anode is much faster than that at the cathode, the kinetic loss of the fuel cell mostly depends on the cathode side. Thus the charge transfer resistance for both anode and cathode are simplified to R_{ct} [91]. R_o is the total ohmic resistance for the cell, and W_s is the finite-length Warburg impedance used to simulate the mass transport loss. The double layer capacitance effects normally modeled by a plane capacitor is replaced by a constant phase element (CPE) parallel connected to the charge transfer resistance and Warburg impedance, as the effect of capacitance is distributed along the length of the pores in the

GDE. With this model, the values of ohmic resistance and charge transfer resistance can be fitted from the Nyquist curves at different current density regions.

The impedance spectra with different pre-compression conditions at the current densities of 100mA/cm^2 and 500mA/cm^2 are shown in Fig. 5.4 and 5.5. The variations of the ohmic and charge transfer resistances with cold pre-compression pressure are shown in Fig. 5.6. The parameters fitted from the curves are listed in Table 5.1. For the current density of 100 mA·cm^{-2}, the cell overpotential is dominated by the activation losses, while around 500 mA·cm^{-2} the ohmic losses are also significant. From Fig. 5.4 and 5.5 the results show that the ohmic resistances under different pre-compression pressures are very close to each other. It means that the cold pre-compression treatment does not have an observable effect on the ohmic resistance, thus has hardly any effect on the ohmic overpotential. This result confirms the general observations from the polarization curves. These results are as expected. First, the ionic resistance of the membrane should not change due to the levels of pre-compression pressures used in this study, which are not large enough to deform the backbone structure of Nafion polymer electrolyte membrane. Secondly, the contact resistances for all the cases should be the same because the assembly compression pressure are identical for all the cells and the pre-compression on the channel area has no effect on the contact resistance. The only factor may lead to different results in the ohmic resistance is the reduction in GDE thickness and compactness. Clearly, the results show that such a change, if any, is insignificant in the total resistance. Therefore, the total ohmic resistance for the PEM fuel cell measured in the EIS keeps almost identical and the cold pre-compression treatment has no observable effect on the ohmic loss.

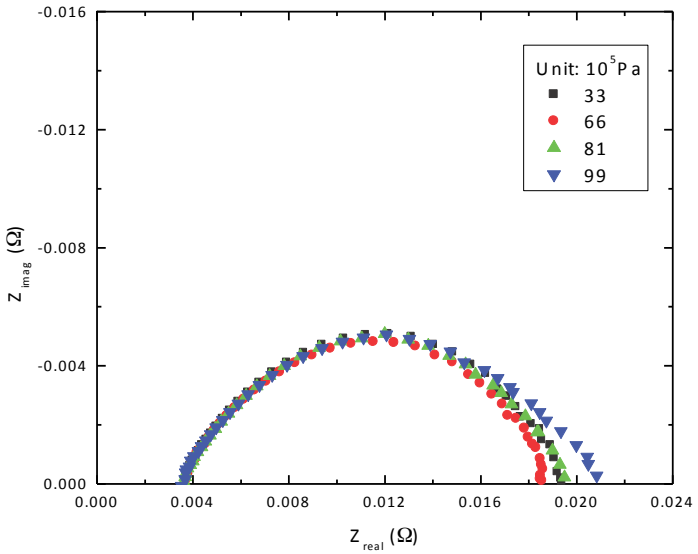

Fig. 5.4 Electrochemical impedance spectroscopy with different cold pre-compression pressures at current density 100mA/cm^2

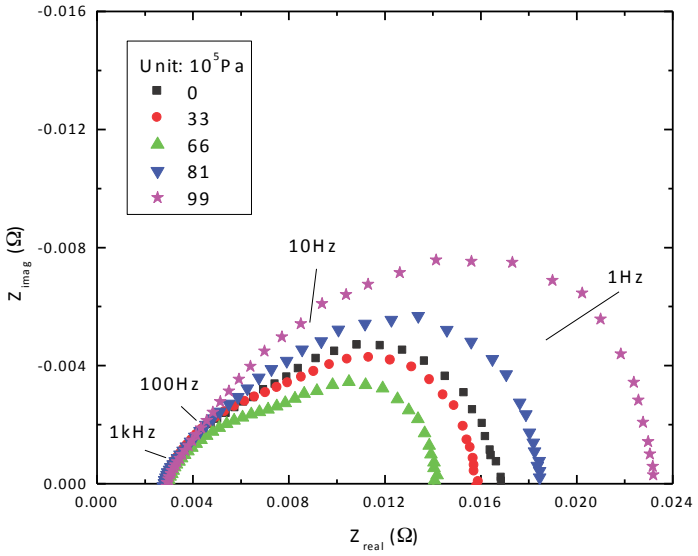

Fig. 5.5 Electrochemical impedance spectroscopy with different cold pre-compression pressures at current density 500mA/cm^2

In contrast to the results of the ohmic resistance, it is shown in Fig. 5.6 that the charge transfer resistance is affected significantly by the cold pre-compression treatment. Essentially, the charge transfer resistance decreases as the pre-compression pressure increases, and reaches a minimum and then increases sharply as the compression pressure further increases. At about 66×10^5Pa, the charge transfer resistance reaches the minimum. Further increases in the compression pressure, the charge transfer resistance becomes even greater than that for the original GDE without pre-compression treatment. As it is known that charge transfer resistance is related to the activation loss, which is a major loss in PEM fuel cells. With the treatment of cold pre-compression, the charge transfer resistance can be significantly reduced, thus a PEM fuel cell performance can be enhanced by such a pre-treatment.

Although the EIS results at both 100 mA/cm^2 and 500 mA/cm^2 shown in Fig. 5.4 and 5.5 have the same trend: the impedance first decreases with the pre-compression pressure and then increase significantly, the magnitudes of increase in impedance for the pressures of 81×10^5Pa and 99×10^5Pa at 500mA/cm^2 are much greater than those at current density of 100 mA/cm^2. Such large increases in impedance are also due to the mass transport loss. At large current density region, the mass transport loss becomes important. As the method of cold pre-compression applied on the GDEs, the total porosity is reduced by the compression, and its permeability is reduced, thus leading to greater mass transport losses. In summary, the EIS results clearly show that there exists an optimal compression pressure that results in a maximum of fuel cell performance, and such maximum is due to its combined effects on charge transfer and mass transfer resistances.

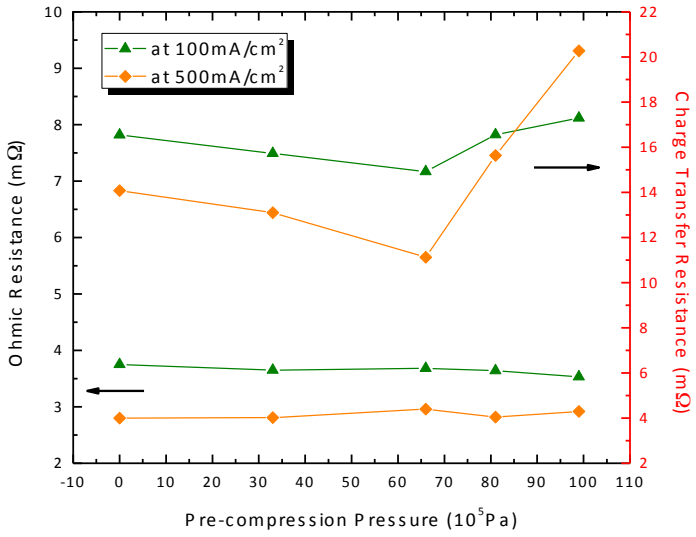

Fig. 5.6 Variations of ohmic resistance and charge transfer resistance

5.4 Cyclic voltammetry

From the above results of EIS, the effect of cold pre-compression treatment on PEM fuel cell performance mainly comes from the variation of charge transfer resistance. Charge transfer resistance is inversely proportion to the charge transfer area in the electrode, which is also considered as the ECA. Thus cyclic voltammetry is applied to investigate the ECA performance under different pre-compression pressure as Fig. 5.7.

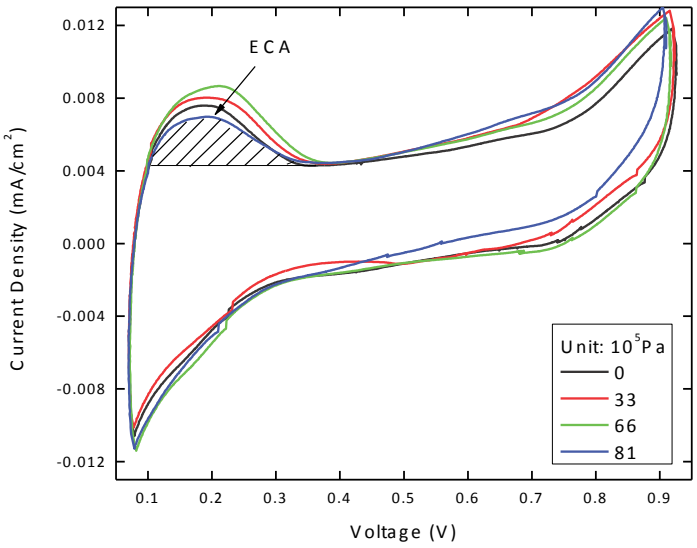

Fig. 5.7 Cyclic voltammogram of scan rate 40mV/s with different cold pre-compression pressures: 0, 33, 66, 81 ($\times 10^5$Pa)

In this region, the effects from the activation loss are dominant while the ohmic loss and concentration loss are negligible. In order to facilitate the following discussion, the Butler-Volmer equation (5.2) for current density per unit volume of the catalyst layer i is reproduced as below:

$$i = a j_0 \left(\frac{c_R^*}{c_R^{0*}} e^{\alpha n F \eta/(RT)} - \frac{c_P^*}{c_P^{0*}} e^{-(1-\alpha) n F \eta/(RT)} \right) \tag{5.2}$$

where a is the active area per unit volume of the catalyst layer (m^2/m^3); j_0 is the exchange current density (A/m^2) per unit active catalyst area; c_R^* is the reactant concentration; α is the transfer coefficient; n is the number of electrons transferred in the rate-determining-step of the reactions; F is the Faraday constant; η is the activation overpotential; and T is the cell temperature. It is reasonable to state that in the low current

density region, the reaction on the electrode surface is moderate and the actual concentration with different pre-compression case will not vary much from each other. So the concentration term in the equation is not a significant factor. While the operation conditions are the same for all the different compression cases, the only factor that is different is the active reaction area ratio *a*. Since the value of *a* is directly related to the ECA, the cyclic voltammetry measurement has been carried out to investigate the pre-compression effects on the ECA.

During the measurement, the voltage is swept between 0.00 and 1.00 V by a scan rate of 40 mV/s. Each of the case is conducted by 5 cycles and the ECA (cm^2/mg_{Pt}) can be calculated from integrating the column charge areas [79, 80]. The ECA values are integrated from the shaded areas in cyclic voltammogram as shown in Fig. 6.8, and the final results are shown in Table 5.1 and Fig. 5.8. The basic integrated area is for hydrogen desorption from the catalyst particles surface at the working electrode between the left side and the voltage around 0.4 V.

The CV results show that the ECA increases with pre-compression pressure and reaches its maximum at $66x10^5$Pa, and then decreases with further increase in pre-compression pressure. These results clearly show that the dominant fundamental reason for the effects of cold pre-compression on PEM fuel cell performance is the changes in ECA due to the compression. It is reasonable to induce that the cold pre-compression can increase the contact area between the catalyst particles and the ionomer structure inside the catalyst layer, thus leading to the increase of ECA; while over-compression may compact some of the micro-pores causing some of the catalyst particles become inaccessible by the reactant, thus reducing the ECA.

Table 5.1 Five different cold pre-compression conditions

Cold pre-compression condition	Torque/ bolt (N-m)	Pressure on GDE (10^5Pa)	Thickness (mm)	Current at 100mA/cm^2		Current at 500mA/cm^2		ECA (cm^2_{Pt}·mg^{-1}_{Pt})
				R_o (mΩ)	R_{ct} (mΩ)	R_o (mΩ)	R_{ct} (mΩ)	
1	N/A	N/A	0.798	3.75	16.55	2.8	14.08	448.1
2	6.21	33	0.737	3.65	15.73	2.81	13.1	477.0
3	12.43	66	0.711	3.68	14.92	2.96	11.12	588.7
4	15.25	81	0.704	3.64	16.56	2.82	15.64	484.4
5	18.64	99	0.693	3.53	17.3	2.92	20.27	427.7

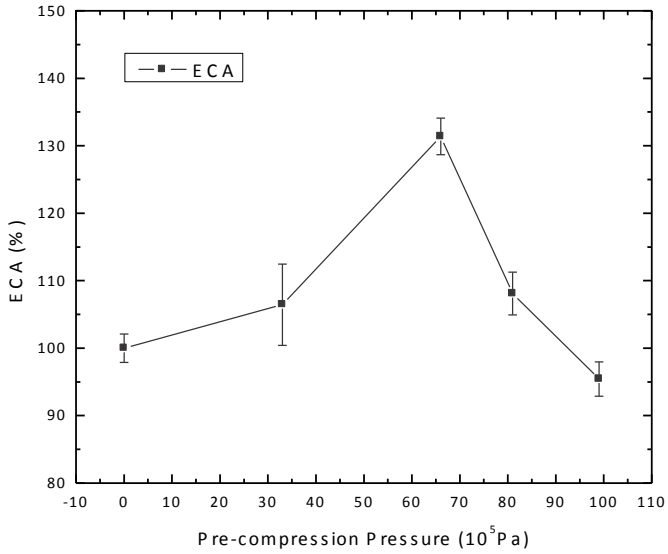

Fig. 5.8 Comparison of ECA values between five pre-compression conditions

CHAPTER 6

MODELING OF CURRENT DENSITY DISTRIBUTION

6.1 Model geometry

A comprehensive 3-Dimensional model for a single serpentine flow field PEM fuel cell is shown in Fig. 6.1. In this model, only cathode side is modeled due to the relatively slow oxygen reduction reaction (ORR) compared to hydrogen oxidation reaction (HOR) at the anode side. The model is mainly constructed by four layers, in z direction from bottom to top, as the land-channel domain, cathode gas diffusion layer, cathode catalyst layer, and polymer electrolyte membrane. In this model, velocity and pressure field are calculated by Navier-Stokes equation. And then a species transport equation and two potential equations in representative of sold phase and membrane phase are coupled and solved. Interfaces between the layers are continuous and no specific boundary conditions are needed. The model is developed of the SIMPLE algorithm in FORTRAN 95.

It shows the program flow chart in Fig. 6.2. The velocity field is prior solved to obtain the velocity and pressure distribution in the domain. And after the convergence of iteration, the velocity values are input into the potential field calculation subroutine. The species equation and potential equation in solid phase and membrane phase are solved simultaneously. Finally after the iteration of coupled equations reaches convergent, the concentration field and current density field are obtained.

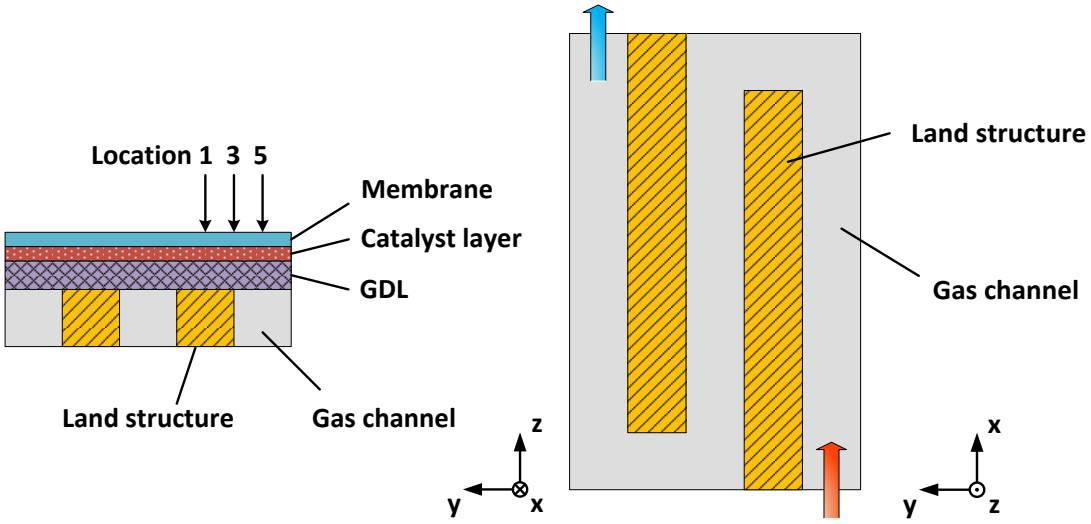

Fig. 6.1 Model geometry of a single serpentine flow field PEM fuel cell

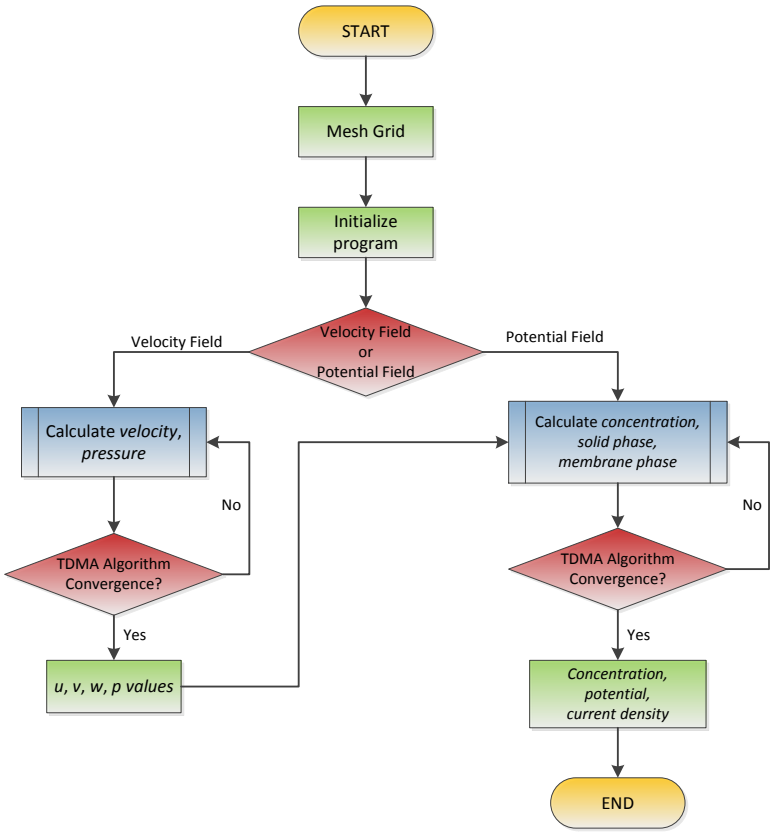

Fig. 6.2 Program flow chart

6.2 Governing equations

The model is based on the three-dimensional PEM fuel cell model (Zhou and Liu, 2006). And there are a couple of assumptions made in this model:

1) The flow field is laminar inside the fuel cell due to the small Renolds number
2) Steady state condition is applied to this model due to the constant reaction condition
3) Only single phase is considered inside the cell
4) Gas is ideal and incompressible (Ma<0.3)

Continuity equation:

$$\nabla \cdot \rho \mathbf{V} = 0 \tag{6.1}$$

Momentum equation:

$$\rho \mathbf{V} \cdot (\nabla \mathbf{V}) = -\nabla p + \begin{cases} \mu \Delta \mathbf{V} & \text{Channel} \\ r^{(2)} \mu \Delta \mathbf{V} - \varepsilon \mu / k_p \mathbf{V} & \text{GDL, catalyst layer, membrane} \end{cases} \tag{6.2}$$

Parameter $r^{(2)}$ is defined as:

$$r^{(2)} = \begin{cases} 0 & \text{Channel} \\ 2.25(1-\varepsilon)^2 / \varepsilon^2 & \text{GDL, catalyst layer, membrane} \end{cases} \tag{6.3}$$

Species equation:

$$\rho \mathbf{V} \cdot (\nabla X_k) = \varepsilon \rho D_{eff} \Delta X_k + \begin{cases} 0 & \text{Channel, GDL, membrane} \\ \varepsilon \rho S_k & \text{catalyst layer} \end{cases} \tag{6.4}$$

Where the effective diffusivity D_{eff} and source term S_k are defined in (6.5) and (6.6) respectively:

$$D_{eff} = \begin{cases} D_k & \text{Channel} \\ D_k \varepsilon^{1.5} & \text{GDL, catalyst layer, membrane} \end{cases} \tag{6.5}$$

Due to the single phase assumption, only

$$S_k = j / 4Fc \tag{6.6}$$

And transfer current density j is calculated from Butler-Volmer equation:

$$j = \left(a i_0^{ref} \right) \left(\frac{X_{O_2}}{X_{O_2,ref}} \right) \left[e^{(\alpha_a F/RT)\eta} - e^{-(\alpha_c F/RT)\eta} \right] \tag{6.7}$$

Due to the variation of ECA in the lateral land-channel direction, a is defined as a function of y:

$$a = F(y) \tag{6.8}$$

The overpotential η is defined in the catalyst layer as:

$$\eta = \phi_s - \phi_m - E_0 \tag{6.9}$$

And two potential equations are coupled to complete the calculation of potential and current density values. For membrane phase, the equation is only applied to catalyst layer and membrane, it shows as:

$$\nabla \cdot (\sigma_m \nabla \phi_m) = \begin{cases} j & \text{Catalyst layer} \\ 0 & \text{Membrane} \end{cases} \tag{6.10}$$

For solid phase, it shows,

$$\nabla \cdot (\sigma_s \nabla \phi_s) = \begin{cases} -j & \text{Catalyst layer} \\ 0 & \text{GDL, land} \end{cases} \tag{6.11}$$

6.3 Boundary conditions

The continuity equation, momentum equation and species equation are solved in the whole domain. All the parameters are assumed to be continuous on the interfaces between different domains, i.e., interface between channel and GDL, GDL and catalyst layer, catalyst layer and membrane. Thus the only boundaries needed are the outer surface of the whole domain. Due to the zero flux, Neumann conditions are applied in all boundaries except the inlet and outlet of the channel as well as non-slip conditions are applied for velocity calculation. At the inlet, the initial velocity and concentration of oxygen are given and at the outlet reference pressure is set.

For the membrane phase potential equation, the domain only includes the catalyst layer and membrane. Due to the negligible potential loss at the anode side, the boundary on the membrane side which is supposed to be contacted with anode is assumed to be zero. All other boundaries follow Neumann conditions, which mean no potential gradient on the boundaries.

The boundaries for the solid phase potential equation follow the same rules except the different calculation domains and the boundary on the top of the land. Domains for solid phase include catalyst layer, gas diffusion layer and land structure. On top of the land, the potential equals the fuel cell operating voltage.

The fuel cell model geometry values and properties are listed in Table 8.1. Most of the values are from ref. [64, 92].

Table 6.1 Fuel cell geometry values and properties

Gas channel length L	1.0×10^{-2} m
Gas channel width W	1.0×10^{-3} m
Gas channel depth D	1.0×10^{-3} m
Gas diffusion layer thickness t_g	2.0×10^{-4} m
Catalyst layer thickness t_{cl}	1.0×10^{-5} m
Membrane thickness t_m	3.0×10^{-5} m
Gas diffusion layer porosity ε_g	0.5
Catalyst layer porosity ε_{cl}	0.3
Membrane porosity ε_m	0.25
Gas diffusion layer permeability k_{p_g}	1.76×10^{-11} m^2
Catalyst layer permeability k_{p_cl}	1.76×10^{-13} m^2
Membrane permeability k_{p_m}	1.58×10^{-18} m^2
Electrical conductivity σ_s	145.0 $S\cdot m^{-1}$
Ionic conductivity σ_m	1.7 $S\cdot m^{-1}$
Reference exchange current density i_0^{ref}	5.0×10^{-4} $A\cdot m^{-2}$
Air diffusivity D_k	5.2197×10^{-6} $m^2\cdot s^{-1}$
Anodic transfer coefficient α_a	0.0
Cathodic transfer coefficient α_c	1.0
Cell temperature T	70 ^oC
Inlet velocity u_{in}	6.0 $m\cdot s^{-1}$
Inlet pressure p	1.0 atm
Inlet oxygen mole fraction	0.21

6.4 ECA lateral distribution

Due to the direct experimental result, the ECA varies in the lateral land-channel direction. As it is introduced in previous section, the ECA under the land has been enhanced by the compression from land structure, while at the channel it keeps original ECA value. In the model, Function (6.8) is defined from curve fitting results. The experimental data is fitted with 4th polynomial equation in Fig. 6.3. a ($m^2 \cdot m^{-3}$) is derived from ECA, catalyst loading amount and the electrode size geometry.

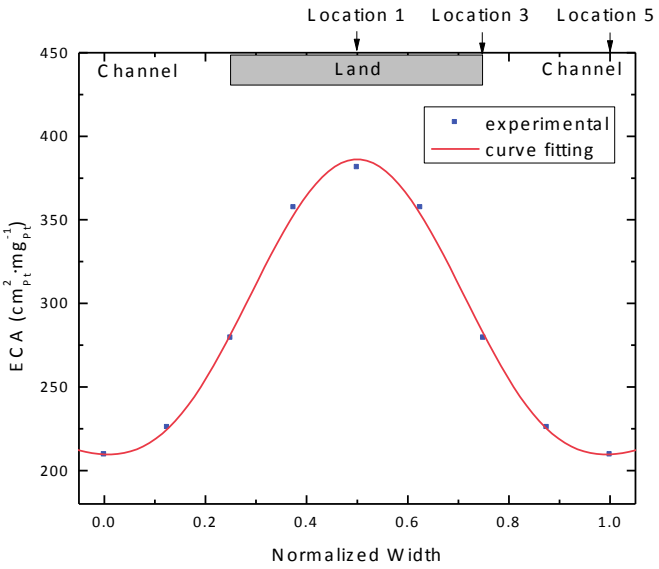

Fig. 6.3 Experimental and curve fitting of ECA distribution in lateral land-channel direction

6.5 Model validation and velocity field

The model is tested under three different configurations with (I) 21×32×40, (II) 21×62×40, (III) 21×92×40 elements in the x-, y- and z-direction to validate the grid independence. As the study focuses on the performance in the lateral direction, the grid configuration is mainly considered in the y-direction. The oxygen mole fraction inside

the catalyst layer in the lateral direction under land and channel is compared under three configurations in Fig. 6.4. Clearly grid (II) and (III) are very close to each other, and the maximal variation is 3.6%. While the grid (I) is greatly different from (II) and (III) due to its sparse mesh configuration in y-direction, and the maximal variation between (I) and (II) is as large as 15.8%. Thus, grid configuration (II) is selected in this study to compromise the usage of computation resource and accuracy.

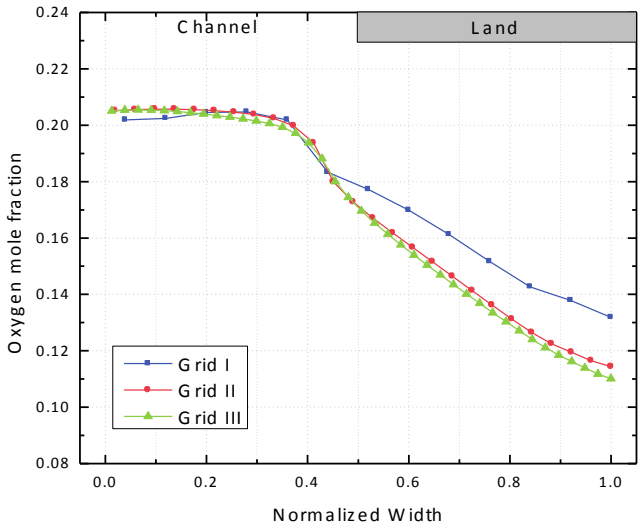

Fig. 6.4 Oxygen mole fraction in lateral direction under three grid configuration: (I) 21×32×40, (II) 21×62×40, (III) 21×92×40

It shows the velocity field in XY-plane at the middle height of the channel in Fig. 6.5 with different grid configuration. Due to the non-slip boundary condition, the velocity profile near the land equals zero, while the maximal velocity locates at the center of channel. Reynolds number of flow inside the channel is less than 2300, which means the flow is laminar. In Fig. 6.6, the flow field in YZ-plane through the GDL and catalyst layer over the land shows that the velocity across the lateral direction is also significant.

Due to the pressure difference between two adjacent channels in serpentine flow field, there exists mass transportation in GDL and catalyst layer across over the land structure. Besides, it indicates that the velocity inside the catalyst layer is much smaller than that in GDL because of lower porosity and permeability.

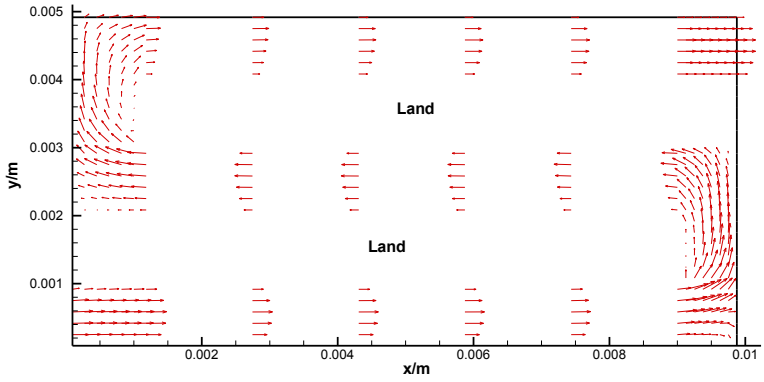

Fig. 6.5(a) Flow field in XY-plane at the middle height of channel with grid 21×32×40

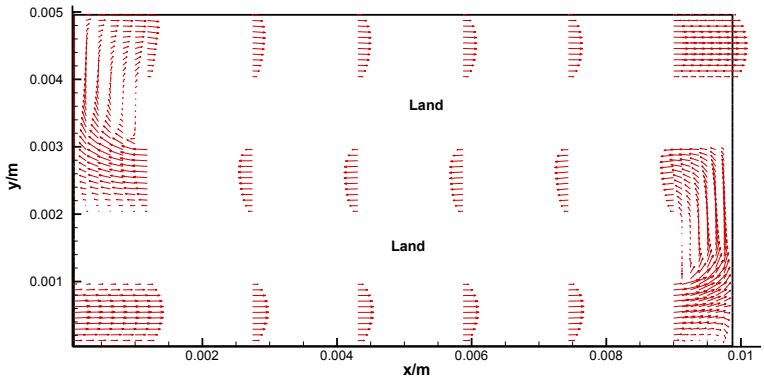

Fig. 6.5(b) Flow field in XY-plane at the middle height of channel with grid 21×62×40

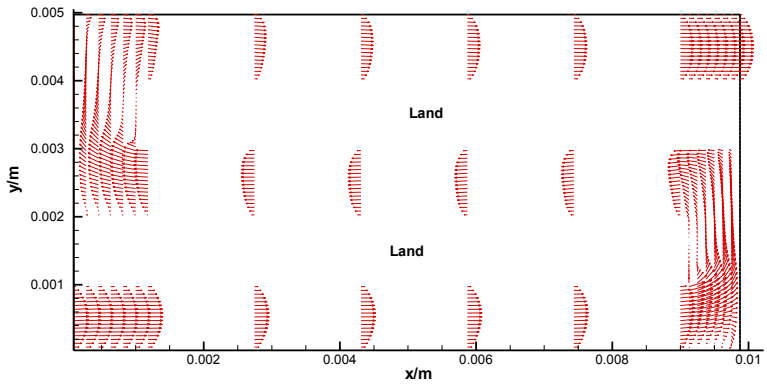

Fig. 6.5(c) Flow field in XY-plane at the middle height of channel with grid 21×92×40

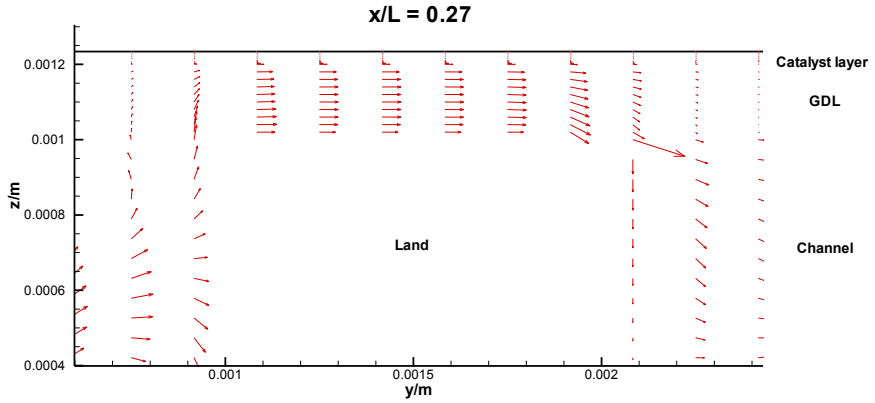

Fig. 6.6 Flow field in YZ-plane through the GDL and catalyst layer across the land

6.6 Concentration field

The oxygen mole fraction contours in XY-plane in different domains for cell voltage 0.8V are shown in Fig. 6.7(a)-(c). At this cell voltage, the inlet oxygen for reaction is abundant and only little amount has been consumed. In Fig. 6.7(a), at the layer of middle height of channel the land structure is distinct from the channel area. Due to the little consumption, even at the outlet of channel the oxygen mole fraction is still as high as 0.17. And the concentration reduces continuously along the channel from inlet to outlet.

When the profile is selected at the middle height of GDL in Fig. 6.7(b), the oxygen mole fraction along the channel and land has changed. As the oxygen transmits in pores of GDL from channel area to land, the mole fraction near the inlet varies gradually in the lateral direction (y-direction). Obviously near the inlet the pressure difference between adjacent channels are larger than the location at the end of land, which causes more convection under the land in GDL and catalyst layers. Thus the transmission effect from channel to land is more significant near the beginning of land structure in both Fig. 6.7(b) and (c). Due to the porous properties of GDL and catalyst layer, the oxygen distribution becomes more uniform inside Fig. 6.7(c). This is very important for the fuel cell reaction because electrochemical area under the land is more difficult for oxygen to access, which may lead to non-uniform current density in the lateral direction and hinder obtaining higher performance of fuel cell.

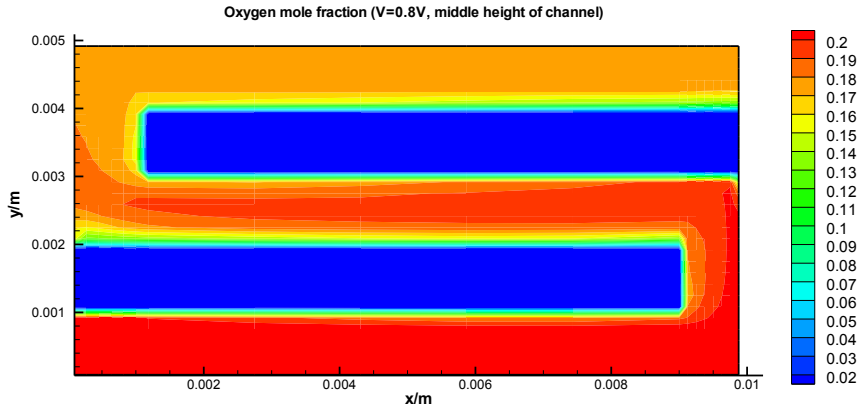

Fig. 6.7(a) Oxygen mole fraction in XY-plane at 0.8V at the middle height of channel

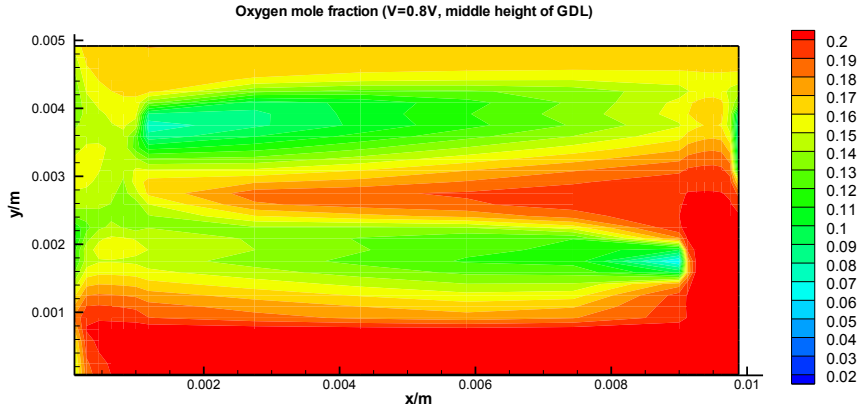

Fig. 6.7(b) Oxygen mole fraction in XY-plane at 0.8V at the middle height of GDL

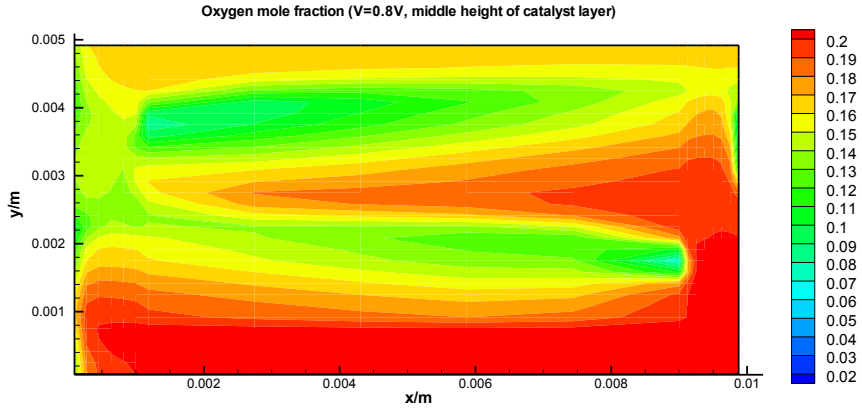

Fig. 6.7(c) Oxygen mole fraction in XY-plane at 0.8V at the middle height of catalyst layer

The oxygen mole fraction contours in XY-plane in different domains for cell voltage 0.6V are shown in Fig. 6.8(a)-(c). Compared with voltage 0.8V, the mole fraction in channel domain does not change visibly in Fig. 6.8(a). However in GDL and catalyst layer domain, the value has significantly decreased. The maximal oxygen mole fraction in Fig. 6.8(b) exists at two locations. One is near the inlet between channel and land, which is caused by the convection effect due to high pressure difference. The other locates near the turning corner of the channel where the velocity is lower and pressure

between channel and GDL is higher, which leads to more oxygen disperses into the porous media. The minimal oxygen mole fraction is at the end of land structure where the convection under land is not significant due to the less pressure drop between adjacent channels. Although in Fig. 6.8(c) some areas may face severe oxygen starvation, the whole fuel cell does not meet the limitation.

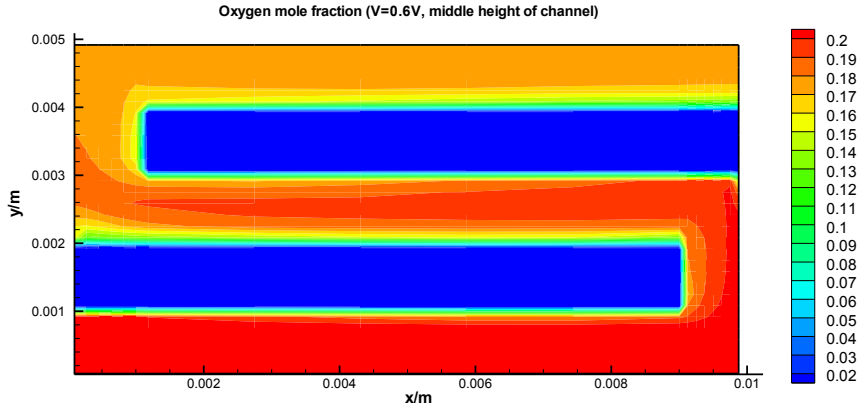

Fig. 6.8(a) Oxygen mole fraction in XY-plane at 0.6V at the middle height of channel

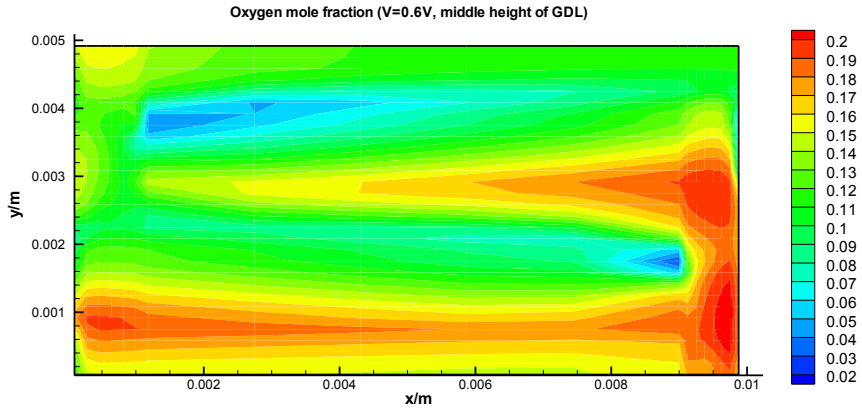

Fig. 6.8(b) Oxygen mole fraction in XY-plane at 0.6V at the middle height of GDL

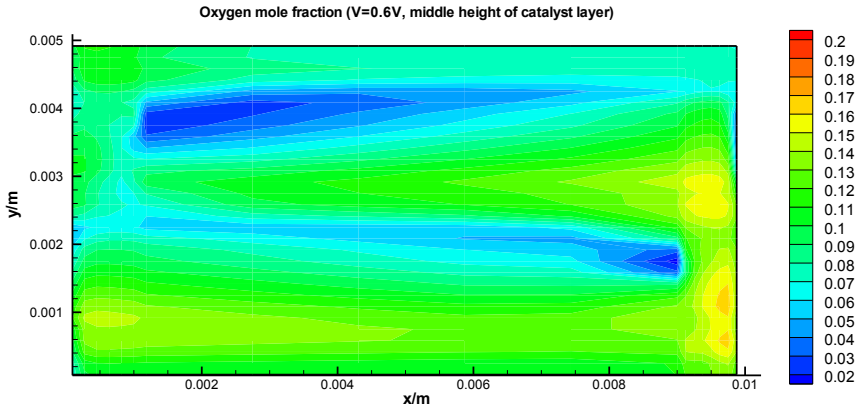

(c)

Fig. 6.8(c) Oxygen mole fraction in XY-plane at 0.6V at the middle height of catalyst layer

The oxygen mole fraction contours in XY-plane in different domains for cell voltage 0.4V are shown in Fig. 6.9(a)-(c). If the three figures of at middle height of channel are compared, the oxygen mole fraction does not have significant variation. However, the contours inside GDL and catalyst layer are totally different. Clearly due to the high current density at low cell voltage, the high consumption of oxygen greatly reduces the mole fraction inside catalyst layer. And due to the low porosity and permeability of GDL and catalyst layer, the current limitation exists at low cell voltage. In Fig. 6.9(c) it shows that most of the areas are lack of oxygen while the concentration loss may exists locally at those areas.

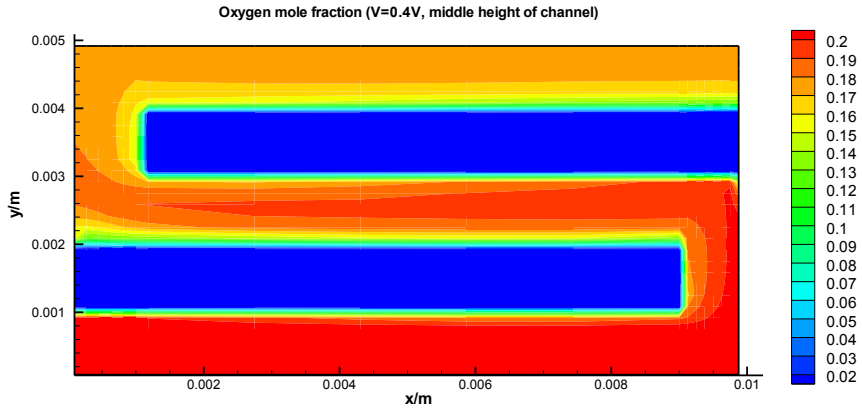

Fig. 6.9(a) Oxygen mole fraction in XY-plane at 0.4V at the middle height of channel

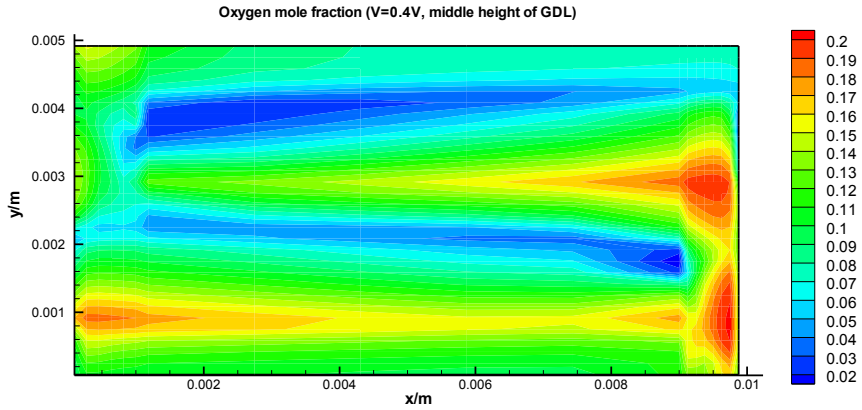

Fig. 6.9(b) Oxygen mole fraction in XY-plane at 0.4V at the middle height of GDL

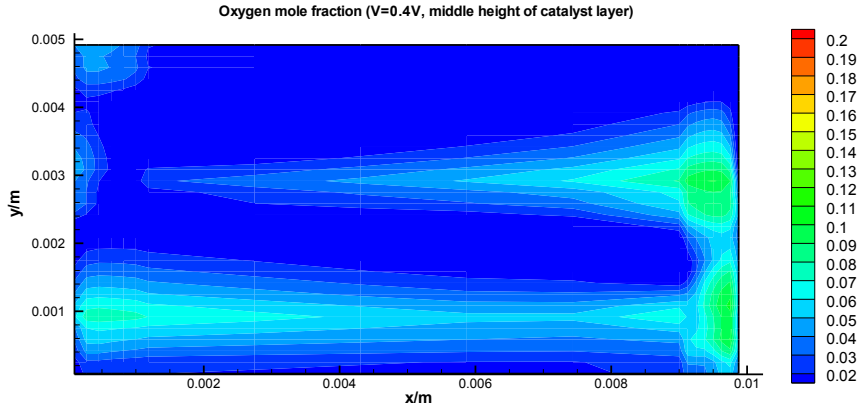

Fig. 6.9(c) Oxygen mole fraction in XY-plane at 0.4V at the middle height of catalyst layer

6.7 Concentration in lateral direction

It shows the oxygen mole fraction in YZ-plane at different cell voltage in Fig. 6.10(a)-(c). The fraction profile indicates the oxygen distribute through GDL and catalyst layer crossover the land structure at the middle length of channel. At 0.8V in Fig. 6.10(a), the distribution of oxygen is under the ordinary condition, mainly depends on the convection effect of the flow inside the porous media. When the voltage decreases to 0.6V, the mole fraction in land area reduces more significantly than the channel due to higher consumption of oxygen. Furthermore, it is obvious that near the location z=0.0012m in Fig. 6.10(b), which indicates the interface between GDL and catalyst layer, the mole fraction drops much faster. As it is known that the electrochemical reaction exists inside the catalyst layer, the demand of oxygen increases while at the low cell voltage. And it requires longer distance for oxygen transmitting from channel to the reaction site in land areas. Thus the reaction in land areas faces more severe concentration conditions than channel areas. Moreover, when the cell voltage decreases till 0.4V in Fig. 6.10(c), the condition of oxygen mole fraction at downstream side of land structure becomes very significant, in some areas near x=0.002m the oxygen for the reaction is no more abundant. And the deficiency of oxygen will eventually impede the increase of current density with further cell voltage decreasing. While the current limitation in land areas comes earlier than that within the channel.

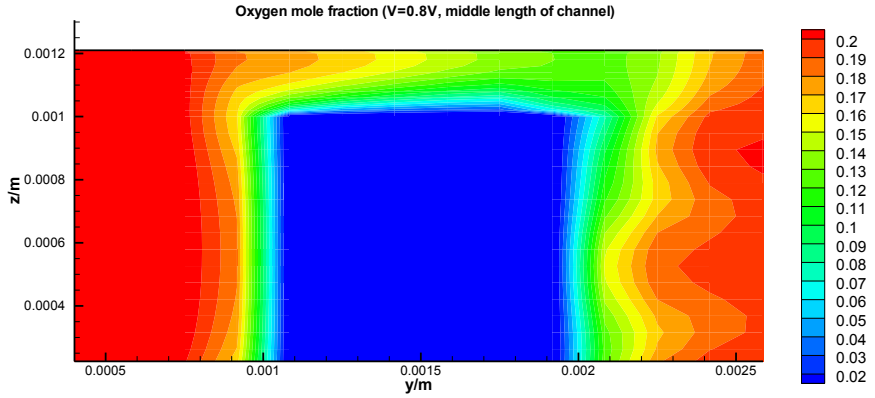

Fig. 6.10(a) Oxygen mole fraction in YZ-plane at the middle length of channel at 0.8V

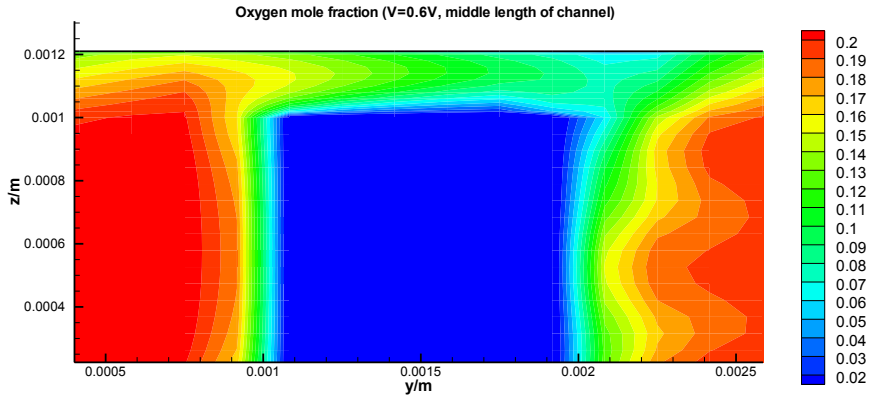

Fig. 6.10(b) Oxygen mole fraction in YZ-plane at the middle length of channel at 0.6V

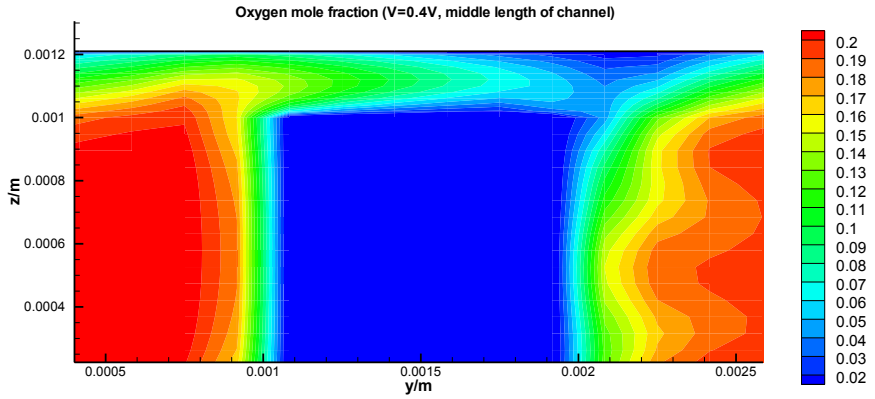

Fig. 6.10(c) Oxygen mole fraction in YZ-plane at the middle length of channel at 0.4V

The oxygen mole fraction distribution in lateral land-channel direction is also analyzed in Fig. 6.11 and 6.12. It illustrates the fraction distribution for different cell voltages in Fig. 6.11. Commonly the mole fraction has the maximal value under the channel and decreases from channel to land due to the mechanism of concentration distribution. However when the cell voltage decreases, the location 5 (center of channel) is no more the maximum. Clearly at 0.6V the highest mole fraction starts to move leftward, and at 0.4V the location of maximal fraction value is at the channel side close to the interface between land and channel. This may be a little controversy as the general idea comes out the highest concentration always locates in channel areas. However, in serpentine flow field the convection effect under the land has strengthened the oxygen molecules migrating into catalyst layer, while in channel areas the diffusion movement is only enforced by the concentration gradient between the channel and catalyst layer. Clearly at low cell voltage this effect becomes significant.

Moreover, at high cell voltage as 0.8V, the ratio between land and channel is not so large based on the high fraction value 0.20 at location 5; while at 0.4V the difference between maximal and minimal values is almost double. Thus as the Butler-Volmer Equation (6.8) indicates, the concentration effect becomes more important to the current density distribution in the lateral land-channel direction at low cell voltage.

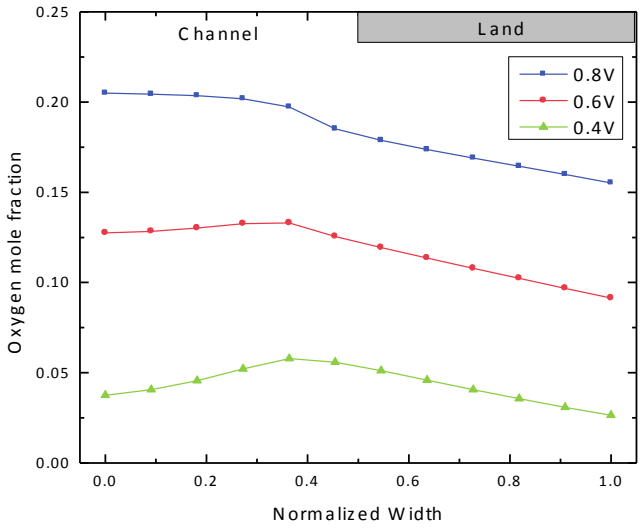

Fig. 6.11 Oxygen mole fraction distribution inside catalyst layer in lateral land-channel direction

Fig. 6.12 also compares the lateral oxygen mole fraction distribution at different locations along the channel at cell voltage 0.8V. All three locations show the mole fraction in channel area is higher than that in land area. However it can be seen that the difference at channel is much less than that under land. This is because the oxygen convection effect across the land is more significant near the inlet than that near the end of land due to pressure gradient between two adjacent channels. While the diffusion effect in channel areas does not have big difference between these locations along the channel direction.

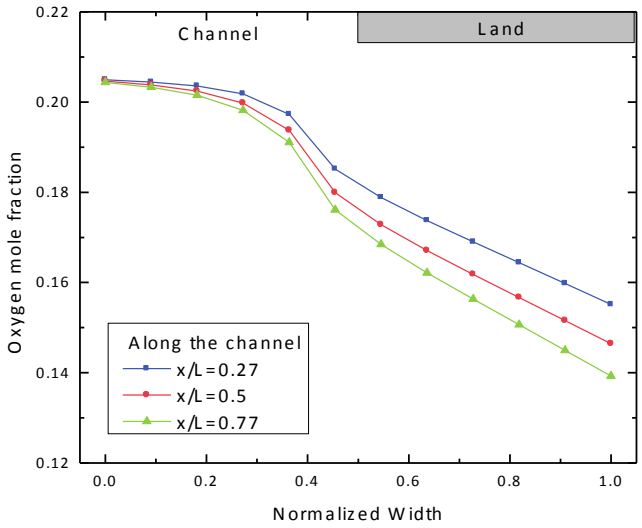

Fig. 6.12 Oxygen mole fraction distribution inside catalyst layer in lateral land-channel direction at 0.8V

6.8 Current density field

It shows the current density contours in the lateral direction at different cell voltages in Fig. 6.13(a)-(c). Due to the non-uniform ECA distribution in land-channel direction, at high cell voltage 0.8V the current density in land area is almost double of that in channel area. This is because the concentration difference at high cell voltage as shown above is not significant between land and channel, while the ECA at land is almost double of the value at channel area. Thus the current density in the lateral land-channel direction mostly depends on the ECA distribution. When the cell voltage decreases to 0.6V in Fig. 6.13(b) and 0.4V in Fig. 6.13(c), the current density variation between land and channel has been mitigated. Clearly the concentration plays an important role at these voltages. Furthermore, as all three contours are selected with the same level numbers, from 0.8V to 0.4V it shows the highest region expands and starts to move towards the interface of land

and channel. This means the current density becomes more uniform in the whole area. Although in Fig. 6.13(a) the current density at the center of channel (y=0.0025m) is significantly lower than other areas due to the ECA value, it has been enhanced by concentration effect since the cell voltage decreases in Fig. 6.13(b) and (c).

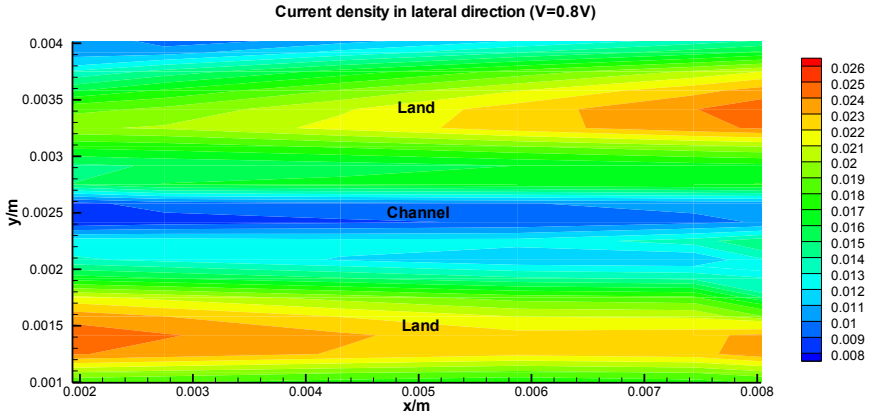

Fig. 6.13(a) The current density contours in XY-plane with temperature 70 oC and inlet velocity 6.0m·s-1 at 0.8V

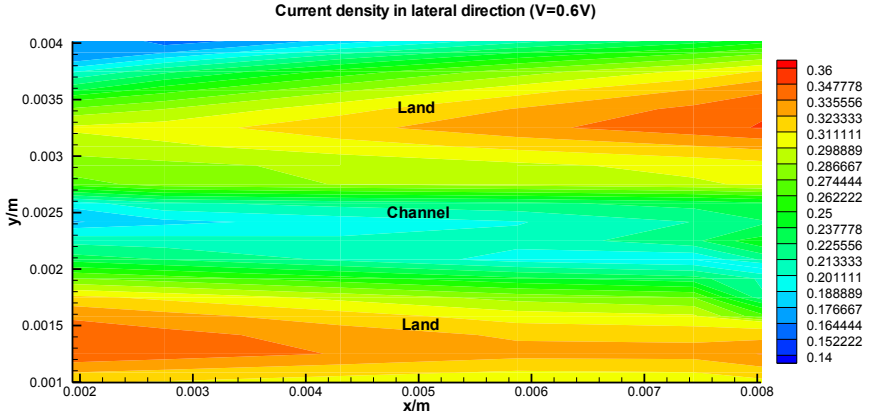

Fig. 6.13(b) The current density contours in XY-plane with temperature 70 ^{o}C and inlet velocity 6.0m·s^{-1} at 0.6V

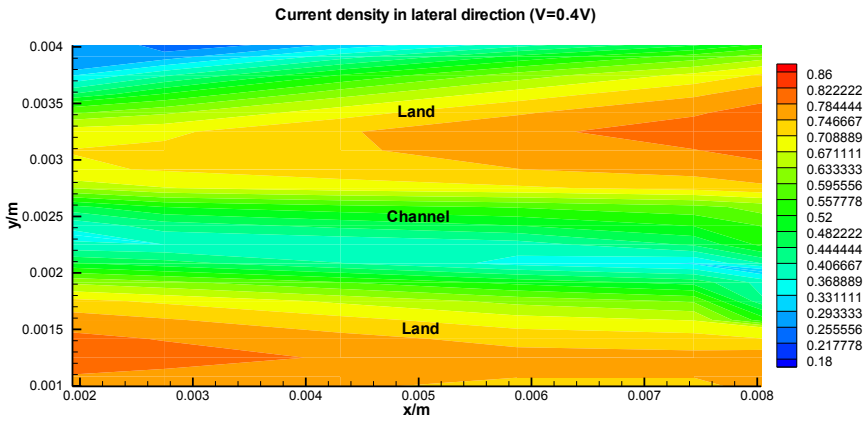

Fig. 6.13(c) The current density contours in XY-plane with temperature 70 ^{o}C and inlet velocity 6.0m·s^{-1} at 0.4V

The modeling results are compared with the experimental results under the same operating conditions. The experimental conditions are introduced in the previous sections. In Fig. 6.14, the polarization curves of 3D model under location 1 (center of land) and location 5 (center of channel) agree well with the experimental results. At the very low cell voltage, the current density under the channel from model is a little higher than the experimental result. It may be because the channel domain also experiences partial deformation due to the land compression, which leads to the sharper concentration drop than the model.

Clearly from Fig. 6.15, the normalized lateral current distribution under 0.8, 0.6 and 0.4V also coincides with the experimental result. At 0.8V, the curve from simulating result fits well with the experiment. However, the model result is slightly higher than the experimental results at 0.4V. Again it may be due to the reduction of porosity and permeability in real fuel cell, while the model does not include their variations by land

compression. Nevertheless, the difference between the modeling and experimental results is less than 5%.

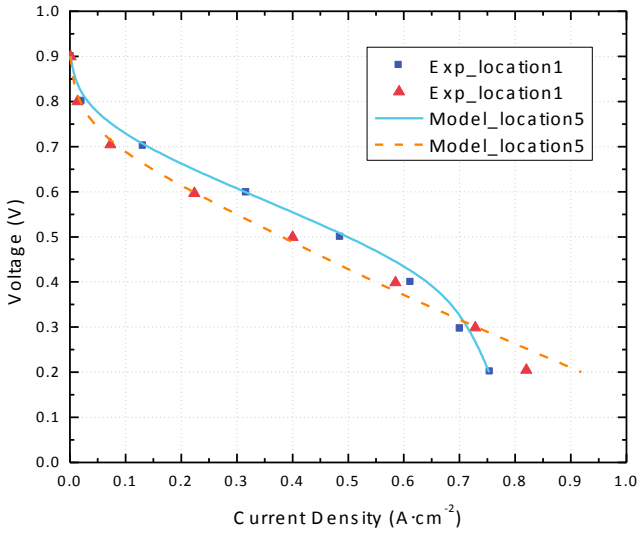

Fig. 6.14 Comparison of experimental and numerical polarization curve results under location 1 and 5. Temperature: 70°C.

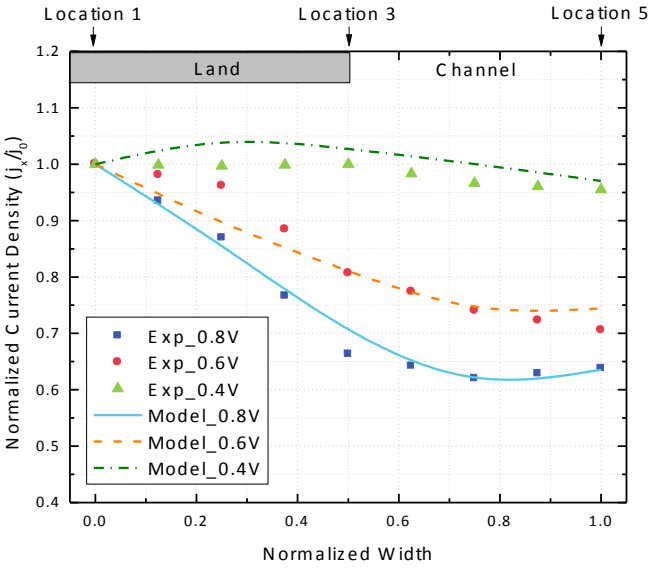

Fig. 6.15 Comparison of experimental and numerical normalized lateral current distribution at 0.8, 0.6 and 0.4V

It also shows the current density distribution inside catalyst layer in lateral direction at two locations along the channel at 0.8V in Fig. 6.16. The current density under the land is much higher than that under the channel. The difference at the center of land is significant, while at the channel the current density is close to each other due to the stable concentration distribution along the channel. The higher performance near inlet than the downstream of channel is due to the stronger convection effect across the land.

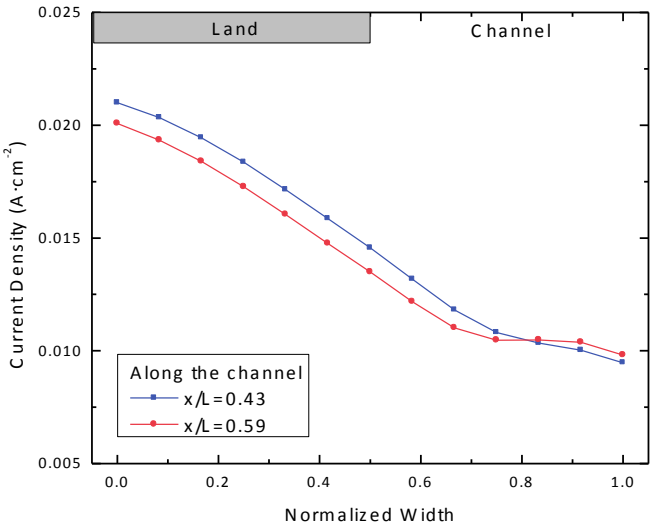

Fig. 6.16 Current density distribution in lateral land-channel direction at 0.8V

CHAPTER 7

CONCLUSION AND SUGGESTIONS FOR FUTURE WORK

7.1 Conclusion

In this study, partially-catalyzed MEAs are used to directly measure the local current density distribution in the lateral direction under land and channel areas. Cyclic voltammetry (CV) and electrochemical impedance spectroscopy (EIS) are used to investigate the mechanism of the current density variations in the lateral direction.. Since the results show that the current density is enhanced under the land, a cold pre-compression treatment is applied on the MEA to improve the overall cell performance. In addition, a 3-dimensional numerical model is developed to simulate the current density distributions. The following conclusions are obtained from these studies:

(a) Current density distribution in lateral direction

- Partially-catalyzed method is a simple and effective way to study the lateral current density distribution in millimeter resolution.
- Polarization curves show that in the high cell voltage region, the current density distribution decreases drastically from land to channel, with the maximum value under the center of the land. However, in the low cell voltage region the current density increases from land to channel, with the maximum under the center of the channel.
- The different reactant flow rates at the cathode side do not have observable effects on the current density distribution in the high cell voltage region, but in

the low cell voltage region high flow rate significantly enhances the performance under the land.

- The higher oxygen concentration in the cathode improves the current density both under land and channel, but the effects under land areas are more significant.

(b) Electrochemical investigation on current density distribution

- CV results show that the main factor for the large lateral current density variations in the high cell voltage region is the lateral ECA variations, i.e. the ECA under the land is much higher than that under the channel.
- EIS results show that the distribution of ohmic resistance is almost constant in the lateral direction. However, the charge transfer resistance in the cathode increases from the land to the channel, while it approaches the maximum under the center of the channel.
- The mass transport loss is negligible in the high cell voltage region, but in the low cell voltage region, the EIS result shows that the mass transport resistance decreases from land to channel.
- The charge transfer resistance decreases with the increase of cell current density, and it is also lower when oxygen is used as the cathode reactant.

(c) Cold pre-compression treatment on MEA

- The cold pre-compression treatment with proper compression pressure on the MEA indeed increases the overall PEM fuel cell performance.
- There exists an optimum compression pressure for this cold pre-compression treatment, and over-compression may have a significantly detrimental effect

on the cell performance.

- EIS results show that the effects on the overall performance, either positive or negative, are mainly due to the change of charge transfer resistances.
- CV results show that the fundamental mechanism of overall performance variations is the ECA changed under different cold pre-compression pressures.

(d) Modeling of current density distribution

- A 3-dimensional fuel cell model incorporated with the variations of ECA in the lateral direction is developed. The model results agree well with the experimental data.
- In the high cell voltage region, the concentration under the channel reaches its maximal value, but the difference between land and channel is not significant; while in the low cell voltage region, the highest concentration in the catalyst layer occurs near the interface between the land and the channel due to the under land convection.
- The non-uniform current densities are distributed both along and across the land and channel directions. The current density is higher under the land in the high cell voltage region where the ECA dominates. When the cell voltage decreases, the difference between land and channel is reduced due to the concentration effects.

7.2 Suggestion for further study

Based on the present research, some areas can be improved in the future.

- The accuracy of this partially-catalyzed method has already met the limitation by the present preparing technique. It needs to find out other techniques to measure the current density distribution in higher resolution.
- Results show that ECA has been improved under land areas. But the fundamental mechanism of ECA variation is still not clear. So it will be a good complement to inspect the microstructure of catalyst layer under nano-scale resolution.
- The 3-D CFD model can be further developed into multiphase and time transient model to simulate the effects from liquid water blocking and fuel cell dynamics.
- A PEM fuel cell system combined with other renewable energy sources such as solar, wind may be a promising future study. With electrolyzers the power generated by other renewable energy systems can be used to produce hydrogen for PEM fuel cells.

REFERENCES

[1] United States. Congress. Senate. Committee on Energy and Natural Resources. Annual Energy Outlook 2012. Washington2012.

[2] O'Hayre R. Fuel cell fundamentals. Hoboken, NJ: John Wiley & Sons; 2006.

[3] Segura F, Duran E, Andujar JM. Design, building and testing of a stand alone fuel cell hybrid system. J Power Sources. 2009;193:276-84.

[4] Appleby AJ, Yeager EB. Solid Polymer Electrolyte Fuel Cells (SPEFCs). Energy, The International Journal, vol 11, Chap 4, pp 137-152. 1986.

[5] Larmine J, Andrew D. Fuel Cell Systems Explained. New York, John Wiley & Sons, LTD. 2000.

[6] Wee JH. Applications of proton exchange membrane fuel cell systems. Renew Sust Energ Rev. 2007;11:1720-38.

[7] Zainoodin AM, Kamarudin SK, Daud WRW. Electrode in direct methanol fuel cells. Int J Hydrogen Energ. 2010;35:4606-21.

[8] Middelman E. Improved PEM fuel cell electrodes by controlled self-assembly. Fuel Cells Science and Technology 2002 Conference on Scientific Advances in Fuel Cell Systems. Amsterdam2002.

[9] Spernjak D, Prasad AK, Advani SG. Experimental investigation of liquid water formation and transport in a transparent single-serpentine PEM fuel cell. J Power Sources. 2007;170:334-44.

[10] Wu JF, Yuan XZ, Wang HJ, Blanco M, Martin JJ, Zhang JJ. Diagnostic tools in PEM fuel cell research: Part I - Electrochemical techniques. Int J Hydrogen Energ. 2008;33:1735-46.

[11] Yuan XZ, Wang HJ, Sun JC, Zhang JJ. AC impedance technique in PEM fuel cell diagnosis - A review. Int J Hydrogen Energ. 2007;32:4365-80.

[12] Stumper J, Campbell SA, Wilkinson DP, Johnson MC, Davis M. In-situ methods for the determination of current distributions in PEM fuel cells. Electrochim Acta. 1998;43:3773-83.

[13] Cleghorn SJC, Derouin CR, Wilson MS, Gottesfeld S. A printed circuit board approach to measuring current distribution in a fuel cell. J Appl Electrochem. 1998;28:663-72.

[14] Wieser C, Helmbold A, Gulzow E. A new technique for two-dimensional current distribution measurements in electrochemical cells. J Appl Electrochem. 2000;30:803-7.

[15] Brett DJL, Atkins S, Brandon NP, Vasileiadis N, Vesovic V, Kucernak AR. Membrane resistance and current distribution measurements under various operating conditions in a polymer electrolyte fuel cell. J Power Sources. 2007;172:2-13.

[16] Brett DJL, Atkins S, Brandon NP, Vesovic V, Vasileiadis N, Kucernak AR. Measurement of the current distribution along a single flow channel of a solid polymer fuel cell. Electrochem Commun. 2001;3:628-32.

[17] Noponen M, Mennola T, Mikkola M, Hottinen T, Lund P. Measurement of current distribution in a free-breathing PEMFC. J Power Sources. 2002;106:304-12.

[18] Mench MM, Wang CYH. An in situ method for determination of current distribution in PEM fuel cells applied to a direct methanol fuel cell. J Electrochem Soc. 2003;150:A79-A85.

[19] Natarajan D, Van Nguyen T. Effect of electrode configuration and electronic conductivity on current density distribution measurements in PEM fuel cells. J Power Sources. 2004;135:95-109.

[20] Hakenjos A, Muenter H, Wittstadt U, Hebling C. A PEM fuel cell for combined measurement of current and temperature distribution, and flow field flooding. J Power Sources. 2004;131:213-6.

[21] Basu S, Renfro MW, Cetegen BM. Spatially resolved optical measurements of water partial pressure and temperature in a PEM fuel cell under dynamic operating conditions. J Power Sources. 2006;162:286-93.

[22] Freunberger SA, Reum M, Evertz J, Wokaun A, Buchi FN. Measuring the current distribution in PEFCs with sub-millimeter resolution. J Electrochem Soc. 2006;153:A2158-A65.

[23] Reum M, Freunberger SA, Wokaun A, Buchi FN. Measuring the current distribution with sub-millimeter resolution in PEFCs. J Electrochem Soc. 2009;156:B301-B10.

[24] Reum M, Wokaun A, Buchi FN. Measuring the current distribution with submillimeter resolution in PEFCs III. Influence of the flow field geometry. J Electrochem Soc. 2009;156:B1225-B31.

[25] Schneider IA, von Dahlen S. Start-stop phenomena in channel and land areas of a polymer electrolyte fuel cell. Electrochem Solid St. 2011;14:B30-B3.

[26] Sun H, Zhang GS, Guo LJ, Dehua S, Liu HT. Effects of humidification temperatures on local current characteristics in a PEM fuel cell. J Power Sources. 2007;168:400-7.

[27] Sun H, Zhang GS, Guo LJ, Liu HT. A novel technique for measuring current distributions in PEM fuel cells. J Power Sources. 2006;158:326-32.

[28] Sun H, Zhang GS, Guo LJ, Liu HT. A Study of dynamic characteristics of PEM fuel cells by measuring local currents. Int J Hydrogen Energ. 2009;34:5529-36.

[29] Zhang GS, Guo LJ, Ma B, Liu HT. Comparison of current distributions in proton exchange membrane fuel cells with interdigitated and serpentine flow fields. J Power Sources. 2009;188:213-9.

[30] Zhang GS, Guo LJ, Ma LZ, Liu HT. Simultaneous measurement of current and temperature distributions in a proton exchange membrane fuel cell. J Power Sources. 2010;195:3597-604.

[31] Zhang GS, Shen SL, Guo LJ, Liu HT. Dynamic characteristics of local current densities and temperatures in proton exchange membrane fuel cells during reactant starvations. Int J Hydrogen Energ. 2012;37:1884-92.

[32] Wang L, Liu HT. Separate measurement of current density under the channel and the shoulder in PEM fuel cells. J Power Sources. 2008;180:365-72.

[33] Higier A, Liu HT. Direct measurement of current density under the land and channel in a PEM fuel cell with serpentine flow fields. J Power Sources. 2009;193:639-48.

[34] Akhtar N, Qureshi A, Scholta J, Hartnig C, Messerschmidt M, Lehnert W. Investigation of water droplet kinetics and optimization of channel geometry for PEM fuel cell cathodes. Int J Hydrogen Energ. 2009;34:3104-11.

[35] Alaefour I, Karimi G, Jiao K, Li X. Measurement of current distribution in a proton exchange membrane fuel cell with various flow arrangements - A parametric study. Appl Energ. 2012;93:80-9.

[36] Gerteisen D, Zamel N, Sadeler C, Geiger F, Ludwig V, Hebling C. Effect of operating conditions on current density distribution and high frequency resistance in a segmented PEM fuel cell. Int J Hydrogen Energ. 2012;37:7736-44.

[37] Fouquet N, Doulet C, Nouillant C, Dauphin-Tanguy G, Ould-Bouamama B. Model based PEM fuel cell state-of-health monitoring via ac impedance measurements. J Power Sources. 2006;159:905-13.

[38] Danzer MA, Hofer EP. Electrochemical parameter identification - An efficient method for fuel cell impedance characterisation. J Power Sources. 2008;183:55-61.

[39] Ciureanu M, Roberge R. Electrochemical impedance study of PEM fuel cells. Experimental diagnostics and modeling of air cathodes. J Phys Chem B. 2001;105:3531-9.

[40] Brunetto C, Moschetto A, Tina G. PEM fuel cell testing by electrochemical impedance spectroscopy. Electr Pow Syst Res. 2009;79:17-26.

[41] Hsieh SS, Yang SH, Feng CL. Characterization of the operational parameters of a H-2/air micro PEMFC with different flow fields by impedance spectroscopy. J Power Sources. 2006;162:262-70.

[42] Boillot M, Bonnet C, Jatroudakis N, Carre P, Didierjean S, Lapicque F. Effect of gas dilution on PEM fuel cell performance and impedance response. Fuel Cells. 2006;6:31-7.

[43] Malevich D, Halliop E, Peppley BA, Pharoah JG, Karan K. Investigation of charge-transfer and mass-transport resistances in PEMFCs with microporous layer using electrochemical impedance spectroscopy. J Electrochem Soc. 2009;156:B216-B24.

[44] Meng H, Wang CY. Electron transport in PEFCs. J Electrochem Soc. 2004;151:A358-A67.

[45] Zhou TH, Liu HT. Effects of the electrical resistances of the GDL in a PEM fuel cell. J Power Sources. 2006;161:444-53.

[46] Springer TE, Zawodzinski TA, Gottesfeld S. Polymer electrolyte fuel-cell model. J Electrochem Soc. 1991;138:2334-42.

[47] Bernardi DM, Verbrugge MW. A mathematical-model of the solid-polymer-electrolyte fuel-cell. J Electrochem Soc. 1992;139:2477-91.

[48] Gurau V, Barbir F, Liu HT. An analytical solution of a half-cell model for PEM fuel cells. J Electrochem Soc. 2000;147:2468-77.

[49] Mazumder S, Cole JV. Rigorous 3-d mathematical modeling of PEM fuel cells - II. Model predictions with liquid water transport. J Electrochem Soc. 2003;150:A1510-A7.

[50] Mazumder S, Cole JV. Rigorous 3-d mathematical modeling of PEM fuel cells - I. Model predictions without liquid water transport. J Electrochem Soc. 2003;150:A1503-A9.

[51] Du CY, Shi PF, Cheng XQ, Yin GP. Effective protonic and electronic conductivity of the catalyst layers in proton exchange membrane fuel cells. Electrochem Commun. 2004;6:435-40.

[52] Nguyen PT, Berning T, Djilali N. Computational model of a PEM fuel cell with serpentine gas flow channels. J Power Sources. 2004;130:149-57.

[53] Wang L, Liu HT. Performance studies of PEM fuel cells with interdigitated flow fields. J Power Sources. 2004;134:185-96.

[54] You LX, Liu HT. A two-phase flow and transport model for PEM fuel cells. J Power Sources. 2006;155:219-30.

[55] Roshandel R, Farhanieh B. The effects of non-uniform distribution of catalyst loading on polymer electrolyte membrane fuel cell performance. Int J Hydrogen Energ. 2007;32:4424-37.

[56] Nitta I, Karvonen S, Himanen O, Mikkola M. Modelling the effect of inhomogeneous compression of GDL on local transport phenomena in a PEM fuel cell. Fuel Cells. 2008;8:410-21.

[57] Bapat CJ, Thynell ST. Effect of anisotropic electrical resistivity of gas diffusion layers (GDLs) on current density and temperature distribution in a Polymer Electrolyte Membrane (PEM) fuel cell. J Power Sources. 2008;185:428-32.

[58] Bapat CJ, Thynell ST. Effect of anisotropic thermal conductivity of the GDL and current collector rib width on two-phase transport in a PEM fuel cell. J Power Sources. 2008;179:240-51.

[59] Su ZY, Liu CT, Chang HP, Li CH, Huang KJ, Sui PC. A numerical investigation of the effects of compression force on PEM fuel cell performance. J Power Sources. 2008;183:182-92.

[60] Kleemann J, Finsterwalder F, Tillmetz W. Characterisation of mechanical behaviour and coupled electrical properties of polymer electrolyte membrane fuel cell gas diffusion layers. J Power Sources. 2009;190:92-102.

[61] Shi ZY, Wang X, Guessous L. Effect of compression on the water management of a proton exchange membrane fuel cell with different gas diffusion layers. J Fuel Cell Sci Tech. 2010;7:-.

[62] Chippar P, Kyeongmin O, Kang K, Ju H. A numerical investigation of the effects of GDL compression and intrusion in polymer electrolyte fuel cells (PEFCs). Int J Hydrogen Energ. 2012;37:6326-38.

[63] Garcia-Salaberri PA, Vera M, Zaera R. Nonlinear orthotropic model of the inhomogeneous assembly compression of PEM fuel cell gas diffusion layers. Int J Hydrogen Energ. 2011;36:11856-70.

[64] Zhou TH, Liu HT. A general three-dimensional model for proton exchange membrane fuel cells. Int J of Transport Phenomena. 2001;3:pp.177-98.

[65] Natarajan D, Van Nguyen T. A two-dimensional, two-phase, multicomponent, transient model for the cathode of a proton exchange membrane fuel cell using conventional gas distributors. J Electrochem Soc. 2001;148:A1324-A35.

[66] Berning T, Lu DM, Djilali N. Three-dimensional computational analysis of transport phenomena in a PEM fuel cell. J Power Sources. 2002;106:284-94.

[67] Cheng CH, Lin HH, Lai GJ. Design for geometric parameters of PEM fuel cell by integrating computational fluid dynamics code with optimization method. J Power Sources. 2007;165:803-13.

[68] Rao RM, Rengaswamy R. Optimization study of an agglomerate model for platinum reduction and performance in PEM fuel cell cathode. Chem Eng Res Des. 2006;84:952-64.

[69] Wishart J, Dong Z, Secanell A. Optimization of a PEM fuel cell system based on empirical data and a generalized electrochemical semi-empirical model. J Power Sources. 2006;161:1041-55.

[70] Song DT, Wang QP, Liu ZS, Navessin T, Eikerling M, Holdcroft S. Numerical optimization study of the catalyst layer of PEM fuel cell cathode. J Power Sources. 2004;126:104-11.

[71] Wilson MS, Gottesfeld S. Thin-film catalyst layers for polymer electrolyte fuel-cell electrodes. J Appl Electrochem. 1992;22:1-7.

[72] Wilson MS, Gottesfeld S. High-performance catalyzed membranes of ultra-low Pt loadings for polymer electrolyte fuel-cells. J Electrochem Soc. 1992;139:L28-L30.

[73] Uchida M, Aoyama Y, Eda N, Ohta A. Investigation of the microstructure in the catalyst layer and effects of both perfluorosulfonate ionomer and PTFE-Loaded carbon on the catalyst layer of polymer electrolyte fuel cells. J Electrochem Soc. 1995;142:4143-9.

[74] Uchida M, Aoyama Y, Eda N, Ohta A. New preparation method for polymer-electrolyte fuel-cells. J Electrochem Soc. 1995;142:463-8.

[75] Uchida M, Aoyama Y, Tanabe M, Yanagihara N, Eda N, Ohta A. Influences of both carbon supports and heat-treatment of supported catalyst on electrochemical oxidation of methanol. J Electrochem Soc. 1995;142:2572-6.

[76] Mehta V, Cooper JS. Review and analysis of PEM fuel cell design and manufacturing. J Power Sources. 2003;114:32-53.

[77] Higier A, Liu HT. Optimization of PEM fuel cell flow field via local current density measurement. Int J Hydrogen Energ. 2010;35:2144-50.

[78] Higier A, Liu HT. Separate in situ measurements of ECA under land and channel in PEM fuel cells. J Power Sources. 2012;215:11-7.

[79] Pozio A, De Francesco M, Cemmi A, Cardellini F, Giorgi L. Comparison of high surface Pt/C catalysts by cyclic voltammetry. J Power Sources. 2002;105:13-9.

[80] Schneider IA, Kramer D, Wokaun A, Scherer GG. Effect of inert gas flow on hydrogen underpotential deposition measurements in polymer electrolyte fuel cells. Electrochem Commun. 2007;9:1607-12.

[81] Ha PT, Moon H, Kim BH, Ng HY, Chang IS. Determination of charge transfer resistance and capacitance of microbial fuel cell through a transient response analysis of cell voltage. Biosens Bioelectron. 2010;25:1629-34.

[82] Jia S, Liu HT. Cold pre-compression of membrane electrode assembly for PEM fuel cells. Int J Hydrogen Energ. 2012;37:13674-80.

[83] Liu HT, Higier A. Effects of the difference in electrical resistance under the land and channel in a PEM fuel cell. Int J Hydrogen Energ. 2011;36:1664-70.

[84] Franco AA, Schott P, Jallut C, Maschke B. A multi-scale dynamic mechanistic model for the transient analysis of PEFCs. Fuel Cells. 2007;7:99-117.

[85] Franco AA, Schott P, Jallut C, Maschke B. A dynamic mechanistic model of an electrochemical interface. J Electrochem Soc. 2006;153:A1053-A61.

[86] Yuan XZ, Sun JC, Blanco M, Wang HJ, Zhang JJ, Wilkinson DP. AC impedance diagnosis of a 500 W PEM fuel cell stack - Part I: Stack impedance. J Power Sources. 2006;161:920-8.

[87] Romero-Castanon T, Arriaga LG, Cano-Castillo U. Impedance spectroscopy as a tool in the evaluation of MEA's. J Power Sources. 2003;118:179-82.

[88] Freire TJP, Gonzalez ER. Effect of membrane characteristics and humidification conditions on the impedance response of polymer electrolyte fuel cells. J Electroanal Chem. 2001;503:57-68.

[89] Neyerlin KC, Gu WB, Jorne J, Gasteiger HA. Determination of catalyst unique parameters for the oxygen reduction reaction in a PEMFC. J Electrochem Soc. 2006;153:A1955-A63.

[90] Dong Q, Santhanagopalan S, White RE. Simulation of the oxygen reduction reaction at an RDE in 0.5 m H2SO4 including an adsorption mechanism. J Electrochem Soc. 2007;154:A888-A99.

[91] Springer TE, Zawodzinski TA, Wilson MS, Gottesfeld S. Characterization of polymer electrolyte fuel cells using AC impedance spectroscopy. J Electrochem Soc. 1996;143:587-99.

[92] Wang L, Husar A, Zhou TH, Liu HT. A parametric study of PEM fuel cell performances. Int J Hydrogen Energ. 2003;28:1263-72.